UNIVERSITY OF CALIFORNIA SAN DIEGO

Integration and Validation of the Simons Observatory Small Aperture Telescope

A dissertation submitted in partial satisfaction of the
requirements for the degree Doctor of Philosophy

in

Physics

by

Joseph Sloane Seibert

Committee in charge:

Professor Kam Arnold, Chair
Professor Dan Green
Professor George Papen
Professor Dan Sievenpiper
Professor Shelley Wright

2023

The Dissertation of Joseph Sloane Seibert is approved, and it is acceptable in quality and form for publication on microfilm and electronically.

University of California San Diego

2023

DEDICATION

To my parents, Robin and Fred, for believing in me more than I have ever believed in myself.

To my brother, Jack, for his kindness and compassion through every memory I have.

To my life partner and forever teammate, Sarah, for her bottomless capacity for love, support, and encouragement.

TABLE OF CONTENTS

LIST OF FIGURES

LIST OF TABLES

ACKNOWLEDGEMENTS

It is difficult to imagine being able to thank everyone who deserves my gratitude in this section, particularly if I'm trying to curtail my tendency to ramble.

First, I have to thank my advisor, Kam Arnold. Thank you for so many hours of your time, in all different forms. From phone calls or Zoom meetings shoved into triple-booked time slots to time in lab breaking off screw heads during SAT disassembly, you have provided unceasing guidance and mentorship. As a role model, your thoughtfulness and empathy have given me a goal for which I'll always strive to reach, and I am forever grateful for that.

For the rest of the UCSD Cosmology group, thank you for your friendship and support. One of the best parts about working in such a big group is the constant community around you, during what can be an isolating time for many others in grad school. Much gratitude to Brian Keating, for creating a group with so much camaraderie and mutual support.

The many postdocs in our group over the years have been terrific mentors as well. To Nick Galitzki, who introduced me to the SAT and has spent an unfathomable amount of time teaching me so much about cryogenics, design principles, instrumentation, and how to maintain a clean lab space (an effort in which I spent many hours disappointing him, I'm sure). Thank you to Grant Teply, for always answering any questions I had about calibration and analysis. To Praween Siritanasak, grad student turned postdoc, who taught me so much about the lab, and has answered all my dumb questions about any number of pieces of hardware, especially the beam mapper chopper. I promise I'll get to paying my outstanding balance for each question, one day. To Kevin Crowley, without whom there is no chance we ever would have been able to finish P10R2, and definitely would never have gotten the whole highbay packed and sent to Chile.

There are so many graduate students who have overlapped with me for whom I am endlessly grateful. Even as a young graduate student, Marty Navaroli and David Leon were so helpful in trying to get up to speed. Tucker Elleflot was always there to help me understand more about detectors and readout, an invaluable resource for much of the work throughout this thesis. Jen Ito and I joined the group at the same time, and she was also my LTAC when I was

TAing 1-series labs in my first quarter. Thank you so much for always being willing to talk through any cosmology or instrumentation topics with me, as we helped each other fight through decades of jargon and esoteric topics. Tran Tsan, thank you for all of your hard work on the SAT. It is no understatement to say you were the backbone of so much work that we did, and without you there's no chance we would've been able to keep track of all the moving pieces inside the highbay. I would thank you for your (seemingly endless) work on documentation, but I think you'd probably like to forget that. Thank you to Megan Russell, who has been my officemate for all six years at UCSD. Many of my favorite memories of grad school are when we would put off whatever K2SO work we needed to get done, and instead just vent about whatever chaos was going on around us. To Lindsay Lowry, thank you so much for your friendship and guidance. Hours spent on FTS alignment and analysis or debugging motor control code would not have been possible without your positivity and compassion. To Logan Howe, who mentored me in my first projects in the lab. I'll never forget you helping me late on a Friday evening in my first time cooling down the DR by myself, not to mention countless other times you were always willing to drop whatever you were working on to answer whatever silly question I had, especially when I was just getting started with basically no practical lab experience. Jake Spisak has always been a driving force for my understanding of any problem in lab, or broader cosmology. Whenever I tried to handwave my way through an answer, you never hesitated to push further to try and understand more. Even more important, thank you for always being willing to talk about or watch sports with me, whenever work was the farthest thing from my mind. To Michael Randall, thank you for always bringing levity, enthusiasm, and support to the lab. Your Club Highbay holiday presents are a highlight of every year, and your constant help, even at ludicrous hours of the evening/morning, were an invaluable part of getting the SAT ready to deploy. I can always rely on Bryce Bixler for all things half-wave plate, even if you've been in Chile for four months. And finally, I would be remiss to not mention Max Silva-Feaver, who has been an amazing office-mate, roommate, lab-mate, teacher, and above all else, an amazing friend. There is no chance I would've been able to make it through the last six years without your

unceasing guidance and companionship. It would be amazing if you were simply an amazing technical mind, who knows the answers to everyone's questions and is always willing to take the time out of your (extraordinarily busy) day and go out of your way to help. But on top of that, you are a source of constant friendship and support not just to me, but to everyone that has ever passed through the lab. For that, I am truly grateful, and this is merely scraping the tip of the iceberg, so thank you.

I've also been really fortunate to work with a number of amazing undergraduate and postbacc students over the course of my time in graduate school. Many have passed through the lab, some of whom have gone on to have amazing careers of their own in academia and industry. In particular, thank you for picking up all the soldering tasks I was desperate to avoid on any given day. An extra special thanks to Ethan Wadhwa, Chris Ellis, and J.B. Lloyd, who, like all undergrad and postbacc members of the lab, know that what we do here would be truly impossible without their help and support.

To the many members of the Simons Observatory collaboration who I have been so lucky to work with over the course of my graduate school career. There are too many to name, so I apologize for any I have missed. But to Jack Lashner, Remy Gerras, Grace Chesmore, Tommy Alford, Katie Harrington, Marius Lungu, and Jenna Moore, especially, for all your help in the final cooldown of the SAT, an enormous thank you.

I can't even imagine my life without all my amazing friends and family, who have been constant in their support, love, and companionship over so much more than just the last six years. To all my San Diego friends, especially Ryan, Cameron, Darius, Sanchit, Jason, Amy, Nick, and Shannon, thank you for making this such a truly special place to live and spend my time here in graduate school. To my Bowdoin friends, Julian, Danny, Tucker, Kenny, Jono, Andrew, Sam, Ryan, Connor, Cam, Ben, Charlie, Greg, Harriet, Penelope, and so many more, you have made my life so rich, and full of joy. Thank you, from the bottom of my heart.

I am so grateful for my family, who have always believed in me and constantly pushed me to follow my dreams.

My dad, Fred, has been a role model unlike any other. You have taught me so much: how to be strong, a friend to everyone, and have a constant curiosity. As a little kid, helping you build tables and fix small things around the house is where I first got my love for making things, and I wouldn't have been able to get through the last six years of turning screws and patching holes with duct tape without that. There is no one I would have rather learned to be a fountain of useless information from. My mom, Robin, is the toughest person I know. You have never backed down from a fight or a challenge, and you passed that on. You have never been afraid to stand up for yourself or your family, and you are fiercely loyal. Thank you for teaching me to love games, to love cooking and food, and to always question the world around me. You have guided me through my entire life, and have been the most constant source of support, showing me how to have determination and perseverance. To both of my parents, thank you for always picking up the phone, no matter the time of day or how busy you were. To my brother, Jack, who has been my best friend since the second he came into my life. I am beyond lucky to have a brother as kind, caring, compassionate, smart, funny, and supportive as you. You've always pushed me to be a better version of myself, even when it's really easy to lean into my worst impulses. You may be my younger brother, but you've always helped me set goals to aspire to, and never failed to be my constant companion.

To all my extended family, Dean, Mary, Craig, Barbara, Adam, Rebecca, Noah, Leni, Alan, Kathy, Dave, Perry, Lily, Leah, Sasha, Georgia, and my grandparents, thank you so much for being the greatest family I could ask for. And to Dennis, who I have known longer than anyone besides my parents. Thank you also to the Brennan/Jensen family, Doug, Bridget, and Thomas, who have always treated me as part of their own, and given me so much kindness and support over the years.

Finally, thank you to Sarah Jensen, who has been so much more than my fiancée. My best friend, my teammate, my constant support, my number one fan and believer. I would not be the person I am without you, and being able to grow up with you and build a life with you is one of the true privileges of my life. You are a magnetic, beautiful, and empathetic soul who gives

more of themselves to the world around you than I would ever have thought possible. Thank you for encouraging me to have confidence in myself, remind me that it's important to take a moment to breathe, and always pushing me out of my comfort zone. It is a special quality to always know what the people in your life need and you never cease to amaze me. I am so proud of all you have accomplished and it has been an honor and a privilege to grow up with you. I cannot wait to spend the rest of my life with you.

Chapter 4, in part, is a reprint of the material as it appears in Joseph Seibert, Peter Ade, Aamir M. Ali, Kam Arnold, Nicholas F. Cothard, Nicholas Galitzki, Kathleen Harrington, Shuay-Pwu Patty Ho, Brian Keating, Lindsay Ng. Lowry, Megan Russell, Maximiliano Silva-Feaver, Praween Siritanasak, Grant P. Teply, Carole Tucker, Eve M. Vavagiakis, and Zhilei Xu. "Development of an optical detector testbed for the Simons Observatory". In: *Millimeter, Submillimeter, and Far-Infrared Detectors and Instrumentation for Astronomy X*. ed. by Jonas Zmuidzinas and Jian-Rong Gao. Vol. 11453. International Society for Optics and Photonics. SPIE, 2020, p. 114532C. DOI: 10.1117/12.2562045. URL: https://doi.org/10.1117/12.2562045.

VITA

2017	B.A. in Physics, Bowdoin College
2023	M.S. in Physics, University of California San Diego
2023	Ph. D. in Physics, University of California San Diego

PUBLICATIONS

Jack Lashner, Joseph Seibert, Max Silva-Feaver, Tanay Bhandarkar, Kevin T. Crowley, Shannon M. Duff, Daniel Dutcher, Kathleen Harrington, Shawn W. Henderson, Amber D. Miller, Michael Niemack, Suzanne Staggs, Yuhan Wang, and Kaiwen Zheng. "The Simons Observatory: complex impedance measurements for a full focal-plane module". In: *Millimeter, Submillimeter, and Far-Infrared Detectors and Instrumentation for Astronomy XI*. ed. by Jonas Zmuidzinas and Jian-Rong Gao. Vol. 12190. Society of Photo-Optical Instrumentation Engineers (SPIE) Conference Series. Aug. 2022, 121900Z, 121900Z. DOI: 10.1117/12.2629374. arXiv: 2207.11804 [astro-ph.IM]

Michael Randall, Akshay Yeddanapudi, Nicholas Galitzki, Aamir Ali, Brian Keating, Jacob Lashner, Joseph Seibert, Maximiliano Silva-Feaver, and Jacob Spisak. "Testing of the radio frequency and magnetic shielding implementation of the first Simons Observatory Small Aperture Telescope, SAT-MF1". In: *Millimeter, Submillimeter, and Far-Infrared Detectors and Instrumentation for Astronomy XI*. ed. by Jonas Zmuidzinas and Jian-Rong Gao. Vol. PC12190. International Society for Optics and Photonics. SPIE, 2022, PC1219013. DOI: 10.1117/12.2630676. URL: https://doi.org/10.1117/12.2630676

Heather McCarrick, Kam Arnold, Zachary Atkins, Jason Austermann, Tanay Bhandarkar, Steve K. Choi, Cody J. Duell, Shannon M. Duff, Daniel Dutcher, Nicholas Galitzk, Erin Healy, Zachary B. Huber, Johannes Hubmayr, Bradley R. Johnson, Michael D. Niemack, Joseph Seibert, Maximiliano Silva-Feaver, Rita F. Sonka, Suzanne T. Staggs, Eve M. Vavagiakis, Yuhan Wang, Zhilei Xu, Kaiwen Zheng, and Ningfeng Zhu. "The 90 and 150 GHz universal focal-plane modules for the Simons Observatory". In: *arXiv e-prints*, arXiv:2112.01458 (Dec. 2021), arXiv:2112.01458. DOI: 10.48550/arXiv.2112.01458. arXiv: 2112.01458 [astro-ph.IM]

Yuhan Wang, Kaiwen Zheng, Zachary Atkins, Jason Austermann, Tanay Bhandarkar, Steve K. Choi, Shannon M. Duff, Daniel Dutcher, Nicholas Galitzki, Erin Healy, Zachary B. Huber, Johannes Hubmayr, Bradley R. Johnson, Jack Lashner, Yaqiong Li, Heather McCarrick, Michael D. Niemack, Joseph Seibert, Maximiliano Silva-Feaver, Rita Sonka, Suzanne T. Staggs, Eve Vavagiakis, and Zhilei Xu. "Simons Observatory Focal-Plane Module: In-lab Testing and Characterization Program". In: *arXiv e-prints*, arXiv:2111.11301 (Nov. 2021), arXiv:2111.11301. DOI: 10.48550/arXiv.2111.11301. arXiv: 2111.11301 [astro-ph.IM]

Heather McCarrick, Erin Healy, Zeeshan Ahmed, Kam Arnold, Zachary Atkins, Jason E. Austermann, Tanay Bhandarkar, James A. Beall, Sarah Marie Bruno, Steve K. Choi, Jake Connors, Nicholas F. Cothard, Kevin D. Crowley, Simon Dicker, Bradley Dober, Cody J. Duell, Shannon M. Duff, Daniel Dutcher, Josef C. Frisch, Nicholas Galitzki, Megan B. Gralla, Jon E. Gudmundsson, Shawn W. Henderson, Gene C. Hilton, Shuay-Pwu Patty Ho, Zachary B. Huber, Johannes Hubmayr, Jeffrey Iuliano, Bradley R. Johnson, Anna M. Kofman, Akito Kusaka, Jack Lashner, Adrian T. Lee, Yaqiong Li, Michael J. Link, Tammy J. Lucas, Marius Lungu, J. A. B. Mates, Jeffrey J. McMahon, Michael D. Niemack, John Orlowski-Scherer, Joseph Seibert, Maximiliano Silva-Feaver, Sara M. Simon, Suzanne Staggs, Aritoki Suzuki, Tomoki Terasaki, Robert Thornton, Joel N. Ullom, Eve M. Vavagiakis, Leila R. Vale, Jeff Van Lanen, Michael R. Vissers, Yuhan Wang, Edward J. Wollack, Zhilei Xu, Edward Young, Cyndia Yu, Kaiwen Zheng, and Ningfeng Zhu. "The Simons Observatory Microwave SQUID Multiplexing Detector Module Design". In: *The Astrophysical Journal* 922.1, 38 (Nov. 2021), p. 38. DOI: 10.3847/1538-4357/ac2232. arXiv: 2106.14797 [astro-ph.IM]

Tran Tsan, Nicholas Galitzki, Aamir M. Ali, Kam Arnold, Gabriele Coppi, Tamar Ervin, Logan Foote, Brian Keating, Jack Lashner, John Orlowski-Scherer, Michael J. Randall, Joseph Seibert, Jacob Spisak, Grant P. Teply, Zhilei Xu, and Ningfeng Zhu. "The effects of inclination on a two stage pulse tube cryocooler for use with a ground based observatory". In: *Cryogenics* 117 (2021), p. 103323. ISSN: 0011-2275. DOI: https://doi.org/10.1016/j.cryogenics.2021.103323. URL: https://www.sciencedirect.com/science/article/pii/S0011227521000813

Ningfeng Zhu, Tanay Bhandarkar, Gabriele Coppi, Anna M. Kofman, John L. Orlowski-Scherer, Zhilei Xu, Shunsuke Adachi, Peter Ade, Simone Aiola, Jason Austermann, Andrew O. Bazarko, James A. Beall, Sanah Bhimani, J. Richard Bond, Grace E. Chesmore, Steve K. Choi, Jake Connors, Nicholas F. Cothard, Mark Devlin, Simon Dicker, Bradley Dober, Cody J. Duell, Shannon M. Duff, Rolando Dünner, Giulio Fabbian, Nicholas Galitzki, Patricio A. Gallardo, Joseph E. Golec, Saianeesh K. Haridas, Kathleen Harrington, Erin Healy, Shuay-Pwu Patty Ho, Zachary B. Huber, Johannes Hubmayr, Jeffrey Iuliano, Bradley R. Johnson, Brian Keating, Kenji Kiuchi, Brian J. Koopman, Jack Lashner, Adrian T. Lee, Yaqiong Li, Michele Limon, Michael Link, Tammy J. Lucas, Heather McCarrick, Jenna Moore, Federico Nati, Laura B. Newburgh, Michael D. Niemack, Elena Pierpaoli, Michael J. Randall, Karen Perez Sarmiento, Lauren J. Saunders, Joseph Seibert, Carlos Sierra, Rita Sonka, Jacob Spisak, Shreya Sutariya, Osamu Tajima, Grant P. Teply, Robert J. Thornton, Tran Tsan, Carole Tucker, Joel Ullom, Eve M. Vavagiakis, Michael R. Vissers, Samantha Walker, Benjamin Westbrook, Edward J. Wollack, and Mario Zannoni. "The Simons Observatory Large Aperture Telescope Receiver". In: *The Astrophysical Journal Supplement Series* 256.1, 23 (Sept. 2021), p. 23. DOI: 10.3847/1538-4365/ac0db7. arXiv: 2103.02747 [astro-ph.IM]

Kathleen Harrington, Carlos Sierra, Grace Chesmore, Shreya Sutariya, Aamir M. Ali, Steve K. Choi, Nicholas F. Cothard, Simon Dicker, Nicholas Galitzki, Shuay-Pwu Patty Ho, Anna M. Kofman, Brian J. Koopman, Jack Lashner, Jeff McMahon, Michael D. Niemack, John Orlowski-Scherer, Joseph Seibert, Max Silva-Feaver, Eve M. Vavagiakis, Zhilei Xu, and Ningfeng Zhu. "The Integration and Testing Program for the Simons Observatory Large Aperture Telescope

Optics Tubes". In: *arXiv e-prints*, arXiv:2102.02129 (Feb. 2021), arXiv:2102.02129. DOI: 10.48550/arXiv.2102.02129. arXiv: 2102.02129 [astro-ph.IM]

L. Montier, B. Mot, P. de Bernardis, B. Maffei, G. Pisano, F. Columbro, J. E. Gudmundsson, S. Henrot-Versillé, L. Lamagna, J. Montgomery, T. Prouvé, M. Russell, G. Savini, S. Stever, K. L. Thompson, M. Tsujimoto, C. Tucker, B. Westbrook, P. A. R. Ade, A. Adler, E. Allys, K. Arnold, D. Auguste, J. Aumont, R. Aurlien, J. Austermann, C. Baccigalupi, A. J. Banday, R. Banerji, R. B. Barreiro, S. Basak, J. Beall, D. Beck, S. Beckman, J. Bermejo, M. Bersanelli, J. Bonis, J. Borrill, F. Boulanger, S. Bounissou, M. Brilenkov, M. Brown, M. Bucher, E. Calabrese, P. Campeti, A. Carones, F. J. Casas, A. Challinor, V. Chan, K. Cheung, Y. Chinone, J. F. Cliche, L. Colombo, J. Cubas, A. Cukierman, D. Curtis, G. D'Alessandro, N. Dachlythra, M. De Petris, C. Dickinson, P. Diego-Palazuelos, M. Dobbs, T. Dotani, L. Duband, S. Duff, J. M. Duval, K. Ebisawa, T. Elleflot, H. K. Eriksen, J. Errard, T. Essinger-Hileman, F. Finelli, R. Flauger, C. Franceschet, U. Fuskeland, M. Galloway, K. Ganga, J. R. Gao, R. Genova-Santos, M. Gerbino, M. Gervasi, T. Ghigna, E. Gjerløw, M. L. Gradziel, J. Grain, F. Grupp, A. Gruppuso, T. de Haan, N. W. Halverson, P. Hargrave, T. Hasebe, M. Hasegawa, M. Hattori, M. Hazumi, D. Herman, D. Herranz, C. A. Hill, G. Hilton, Y. Hirota, E. Hivon, R. A. Hlozek, Y. Hoshino, E. de la Hoz, J. Hubmayr, K. Ichiki, T. Iida, H. Imada, K. Ishimura, H. Ishino, G. Jaehnig, T. Kaga, S. Kashima, N. Katayama, A. Kato, T. Kawasaki, R. Keskitalo, T. Kisner, Y. Kobayashi, N. Kogiso, A. Kogut, K. Kohri, E. Komatsu, K. Komatsu, K. Konishi, N. Krachmalnicoff, I. Kreykenbohm, C. L. Kuo, A. Kushino, J. V. Lanen, M. Lattanzi, A. T. Lee, C. Leloup, F. Levrier, E. Linder, T. Louis, G. Luzzi, T. Maciaszek, D. Maino, M. Maki, S. Mandelli, E. Martinez-Gonzalez, S. Masi, T. Matsumura, A. Mennella, M. Migliaccio, Y. Minami, K. Mitsuda, G. Morgante, Y. Murata, J. A. Murphy, M. Nagai, Y. Nagano, T. Nagasaki, R. Nagata, S. Nakamura, T. Namikawa, P. Natoli, S. Nerval, T. Nishibori, H. Nishino, C. O'Sullivan, H. Ogawa, H. Ogawa, S. Oguri, H. Ohsaki, I. S. Ohta, N. Okada, N. Okada, L. Pagano, A. Paiella, D. Paoletti, G. Patanchon, J. Peloton, F. Piacentini, G. Polenta, D. Poletti, G. Puglisi, D. Rambaud, C. Raum, S. Realini, M. Reinecke, M. Remazeilles, A. Ritacco, G. Roudil, J. A. Rubino-Martin, H. Sakurai, Y. Sakurai, M. Sandri, M. Sasaki, D. Scott, J. Seibert, Y. Sekimoto, B. Sherwin, K. Shinozaki, M. Shiraishi, P. Shirron, G. Signorelli, G. Smecher, R. Stompor, H. Sugai, S. Sugiyama, A. Suzuki, J. Suzuki, T. L. Svalheim, E. Switzer, R. Takaku, H. Takakura, S. Takakura, Y. Takase, Y. Takeda, A. Tartari, E. Taylor, Y. Terao, H. Thommesen, B. Thorne, T. Toda, M. Tomasi, M. Tominaga, N. Trappe, M. Tristram, M. Tsuji, J. Ullom, G. Vermeulen, P. Vielva, F. Villa, M. Vissers, N. Vittorio, I. Wehus, J. Weller, J. Wilms, B. Winter, E. J. Wollack, N. Y. Yamasaki, T. Yoshida, J. Yumoto, M. Zannoni, and A. Zonca. "Overview of the medium and high frequency telescopes of the LiteBIRD space mission". In: *Space Telescopes and Instrumentation 2020: Optical, Infrared, and Millimeter Wave*. Ed. by Makenzie Lystrup and Marshall D. Perrin. Vol. 11443. Society of Photo-Optical Instrumentation Engineers (SPIE) Conference Series. Dec. 2020, 114432G, 114432G. DOI: 10.1117/12.2562243. arXiv: 2102.00809 [astro-ph.IM]

M. Hazumi, P. A. R. Ade, A. Adler, E. Allys, K. Arnold, D. Auguste, J. Aumont, R. Aurlien, J. Austermann, C. Baccigalupi, A. J. Banday, R. Banjeri, R. B. Barreiro, S. Basak, J. Beall, D. Beck, S. Beckman, J. Bermejo, P. de Bernardis, M. Bersanelli, J. Bonis, J. Borrill, F. Boulanger, S. Bounissou, M. Brilenkov, M. Brown, M. Bucher, E. Calabrese, P. Campeti, A. Carones, F. J.

Casas, A. Challinor, V. Chan, K. Cheung, Y. Chinone, J. F. Cliche, L. Colombo, F. Columbro, J. Cubas, A. Cukierman, D. Curtis, G. D'Alessandro, N. Dachlythra, M. De Petris, C. Dickinson, P. Diego-Palazuelos, M. Dobbs, T. Dotani, L. Duband, S. Duff, J. M. Duval, K. Ebisawa, T. Elleflot, H. K. Eriksen, J. Errard, T. Essinger-Hileman, F. Finelli, R. Flauger, C. Franceschet, U. Fuskeland, M. Galloway, K. Ganga, J. R. Gao, R. Genova-Santos, M. Gerbino, M. Gervasi, T. Ghigna, E. Gjerløw, M. L. Gradziel, J. Grain, F. Grupp, A. Gruppuso, J. E. Gudmundsson, T. de Haan, N. W. Halverson, P. Hargrave, T. Hasebe, M. Hasegawa, M. Hattori, S. Henrot-Versillé, D. Herman, D. Herranz, C. A. Hill, G. Hilton, Y. Hirota, E. Hivon, R. A. Hlozek, Y. Hoshino, E. de la Hoz, J. Hubmayr, K. Ichiki, T. Iida, H. Imada, K. Ishimura, H. Ishino, G. Jaehnig, T. Kaga, S. Kashima, N. Katayama, A. Kato, T. Kawasaki, R. Keskitalo, T. Kisner, Y. Kobayashi, N. Kogiso, A. Kogut, K. Kohri, E. Komatsu, K. Komatsu, K. Konishi, N. Krachmalnicoff, I. Kreykenbohm, C. L. Kuo, A. Kushino, L. Lamagna, J. V. Lanen, M. Lattanzi, A. T. Lee, C. Leloup, F. Levrier, E. Linder, T. Louis, G. Luzzi, T. Maciaszek, B. Maffei, D. Maino, M. Maki, S. Mandelli, E. Martinez-Gonzalez, S. Masi, T. Matsumura, A. Mennella, M. Migliaccio, Y. Minami, K. Mitsuda, J. Montgomery, L. Montier, G. Morgante, B. Mot, Y. Murata, J. A. Murphy, M. Nagai, Y. Nagano, T. Nagasaki, R. Nagata, S. Nakamura, T. Namikawa, P. Natoli, S. Nerval, T. Nishibori, H. Nishino, F. Noviello, C. O'Sullivan, H. Ogawa, H. Ogawa, S. Oguri, H. Ohsaki, I. S. Ohta, N. Okada, N. Okada, L. Pagano, A. Paiella, D. Paoletti, G. Patanchon, J. Peloton, F. Piacentini, G. Pisano, G. Polenta, D. Poletti, T. Prouvé, G. Puglisi, D. Rambaud, C. Raum, S. Realini, M. Reinecke, M. Remazeilles, A. Ritacco, G. Roudil, J. A. Rubino-Martin, M. Russell, H. Sakurai, Y. Sakurai, M. Sandri, M. Sasaki, G. Savini, D. Scott, J. Seibert, Y. Sekimoto, B. Sherwin, K. Shinozaki, M. Shiraishi, P. Shirron, G. Signorelli, G. Smecher, S. Stever, R. Stompor, H. Sugai, S. Sugiyama, A. Suzuki, J. Suzuki, T. L. Svalheim, E. Switzer, R. Takaku, H. Takakura, S. Takakura, Y. Takase, Y. Takeda, A. Tartari, E. Taylor, Y. Terao, H. Thommesen, K. L. Thompson, B. Thorne, T. Toda, M. Tomasi, M. Tominaga, N. Trappe, M. Tristram, M. Tsuji, M. Tsujimoto, C. Tucker, J. Ullom, G. Vermeulen, P. Vielva, F. Villa, M. Vissers, N. Vittorio, I. Wehus, J. Weller, B. Westbrook, J. Wilms, B. Winter, E. J. Wollack, N. Y. Yamasaki, T. Yoshida, J. Yumoto, M. Zannoni, and A. Zonca. "LiteBIRD satellite: JAXA's new strategic L-class mission for all-sky surveys of cosmic microwave background polarization". In: *Space Telescopes and Instrumentation 2020: Optical, Infrared, and Millimeter Wave*. Ed. by Makenzie Lystrup and Marshall D. Perrin. Vol. 11443. Society of Photo-Optical Instrumentation Engineers (SPIE) Conference Series. Dec. 2020, 114432F, 114432F. DOI: 10.1117/12.2563050. arXiv: 2101.12449 [astro-ph.IM]

Kenji Kiuchi, Shunsuke Adachi, Aamir M. Ali, Kam Arnold, Peter Ashton, Jason E. Austermann, Andrew Bazako, James A. Beall, Yuji Chinone, Gabriele Coppi, Kevin D. Crowley, Kevin T. Crowley, Simon Dicker, Bradley Dober, Shannon M. Duff, Giulio Fabbian, Nicholas Galitzki, Joseph E. Golec, Jon E. Gudmundsson, Kathleen Harrington, Masaya Hasegawa, Makoto Hattori, Charles A. Hill, Shuay-Pwu Patty Ho, Johannes Hubmayr, Bradley R. Johnson, Daisuke Kaneko, Nobuhiko Katayama, Brian Keating, Akito Kusaka, Jack Lashner, Adrian T. Lee, Frederick Matsuda, Heather McCarrick, Masaaki Murata, Federico Nati, Yume Nishinomiya, Lyman Page, Mayuri Sathyanarayana Rao, Christian L. Reichardt, Kana Sakaguri, Yuki Sakurai, Joseph Sibert, Jacob Spisak, Osamu Tajima, Grant P. Teply, Tomoki Terasaki, Tran Tsan, Samantha Walker, Edward J. Wollack, Zhilei Xu, Kyohei Yamada, Mario Zannoni, and Ningfeng Zhu. "Simons

Observatory Small Aperture Telescope overview". In: *Ground-based and Airborne Telescopes VIII*. ed. by Heather K. Marshall, Jason Spyromilio, and Tomonori Usuda. Vol. 11445. Society of Photo-Optical Instrumentation Engineers (SPIE) Conference Series. Dec. 2020, 114457L, p. 114457L. DOI: 10.1117/12.2562016. arXiv: 2101.11917 [astro-ph.IM]

Y. Sekimoto, P. A. R. Ade, A. Adler, E. Allys, K. Arnold, D. Auguste, J. Aumont, R. Aurlien, J. Austermann, C. Baccigalupi, A. J. Banday, R. Banerji, R. B. Barreiro, S. Basak, J. Beall, D. Beck, S. Beckman, J. Bermejo, P. de Bernardis, M. Bersanelli, J. Bonis, J. Borrill, F. Boulanger, S. Bounissou, M. Brilenkov, M. Brown, M. Bucher, E. Calabrese, P. Campeti, A. Carones, F. J. Casas, A. Challinor, V. Chan, K. Cheung, Y. Chinone, J. F. Cliche, L. Colombo, F. Columbro, J. Cubas, A. Cukierman, D. Curtis, G. D'Alessandro, N. Dachlythra, M. De Petris, C. Dickinson, P. Diego-Palazuelos, M. Dobbs, T. Dotani, L. Duband, S. Duff, J. M. Duval, K. Ebisawa, T. Elleflot, H. K. Eriksen, J. Errard, T. Essinger-Hileman, F. Finelli, R. Flauger, C. Franceschet, U. Fuskeland, M. Galloway, K. Ganga, J. R. Gao, R. Genova-Santos, M. Gerbino, M. Gervasi, T. Ghigna, E. Gjerløw, M. L. Gradziel, J. Grain, F. Grupp, A. Gruppuso, J. E. Gudmundsson, T. de Haan, N. W. Halverson, P. Hargrave, T. Hasebe, M. Hasegawa, M. Hattori, M. Hazumi, S. Henrot-Versillé, D. Herman, D. Herranz, C. A. Hill, G. Hilton, Y. Hirota, E. Hivon, R. A. Hlozek, Y. Hoshino, E. de la Hoz, J. Hubmayr, K. Ichiki, T. iida, H. Imada, K. Ishimura, H. Ishino, G. Jaehnig, T. Kaga, S. Kashima, N. Katayama, A. Kato, T. Kawasaki, R. Keskitalo, T. Kisner, Y. Kobayashi, N. Kogiso, A. Kogut, K. Kohri, E. Komatsu, K. Komatsu, K. Konishi, N. Krachmalnicoff, I. Kreykenbohm, C. L. Kuo, A. Kushino, L. Lamagna, J. V. Lanen, M. Lattanzi, A. T. Lee, C. Leloup, F. Levrier, E. Linder, T. Louis, G. Luzzi, T. Maciaszek, B. Maffei, D. Maino, M. Maki, S. Mandelli, E. Martinez-Gonzalez, S. Masi, T. Matsumura, A. Mennella, M. Migliaccio, Y. Minanmi, K. Mitsuda, J. Montgomery, L. Montier, G. Morgante, B. Mot, Y. Murata, J. A. Murphy, M. Nagai, Y. Nagano, T. Nagasaki, R. Nagata, S. Nakamura, T. Namikawa, P. Natoli, S. Nerval, T. Nishibori, H. Nishino, C. O'Sullivan, H. Ogawa, H. Ogawa, S. Oguri, H. Ohsaki, I. S. Ohta, N. Okada, N. Okada, L. Pagano, A. Paiella, D. Paoletti, G. Patanchon, J. Peloton, F. Piacentini, G. Pisano, G. Polenta, D. Poletti, T. Prouvé, G. Puglisi, D. Rambaud, C. Raum, S. Realini, M. Reinecke, M. Remazeilles, A. Ritacco, G. Roudil, J. A. Rubino-Martin, M. Russell, H. Sakurai, Y. Sakurai, M. Sandri, M. Sasaki, G. Savini, D. Scott, J. Seibert, B. Sherwin, K. Shinozaki, M. Shiraishi, P. Shirron, G. Signorelli, G. Smecher, S. Stever, R. Stompor, H. Sugai, S. Sugiyama, A. Suzuki, J. Suzuki, T. L. Svalheim, E. Switzer, R. Takaku, H. Takakura, S. Takakura, Y. Takase, Y. Takeda, A. Tartari, E. Taylor, Y. Terao, H. Thommesen, K. L. Thompson, B. Thorne, T. Toda, M. Tomasi, M. Tominaga, N. Trappe, M. Tristram, M. Tsuji, M. Tsujimoto, C. Tucker, J. Ullom, G. Vermeulen, P. Vielva, F. Villa, M. Vissers, N. Vittorio, I. Wehus, J. Weller, B. Westbrook, J. Wilms, B. Winter, E. J. Wollack, N. Y. Yamasaki, T. Yoshida, J. Yumoto, M. Zannoni, and A. Zonca. "Concept Design of Low Frequency Telescope for CMB B-mode Polarization satellite LiteBIRD". in: *arXiv e-prints*, arXiv:2101.06342 (Jan. 2021), arXiv:2101.06342. DOI: 10.48550/arXiv.2101.06342. arXiv: 2101.06342 [astro-ph.IM]

Brian J. Koopman, Jack Lashner, Lauren J. Saunders, Matthew Hasselfield, Tanay Bhandarkar, Sanah Bhimani, Steve K. Choi, Cody J. Duell, Nicholas Galitzki, Kathleen Harrington, Adam D. Hincks, Shuay-Pwu Patty Ho, Laura Newburgh, Christian L. Reichardt, Joseph Seibert,

Jacob Spisak, Benjamin Westbrook, Zhilei Xu, and Ningfeng Zhu. "The Simons Observatory: overview of data acquisition, control, monitoring, and computer infrastructure". In: *Software and Cyberinfrastructure for Astronomy VI*. ed. by Juan C. Guzman and Jorge Ibsen. Vol. 11452. Society of Photo-Optical Instrumentation Engineers (SPIE) Conference Series. Dec. 2020, 1145208, p. 1145208. DOI: 10.1117/12.2561771. arXiv: 2012.10345 [astro-ph.IM]

Zhilei Xu, Tanay Bhandarkar, Gabriele Coppi, Anna Kofman, John L. Orlowski-Scherer, Ningfeng Zhu, Aamir M. Ali, Kam Arnold, Jason E. Austermann, Steve K. Choi, Jake Connors, Nicholas F. Cothard, Mark Devlin, Simon Dicker, Bradley Dober, Shannon M. Duff, Giulio Fabbian, Nicholas Galitzki, Saianeesh Haridas, Katheleen Harrington, Erin Healy, Shuay-Pwu Patty Ho, Johannes Hubmayr, Jeffrey Iuliano, Jack Lashner, Yaqiong Li, Michele Limon, Brian J. Koopman, Heather McCarrick, Jenna Moore, Federico Nati, Michael D. Niemack, Christian L. Reichardt, Karen Sarmiento, Joseph Seibert, Maximiliano Silva-Feaver, Rita F. Sonka, Suzanne Staggs, Robert J. Thornton, Eve M. Vavagiakis, Michael R. Vissers, Samantha Walker, Yuhan Wang, Edward J. Wollack, and Kaiwen Zheng. "The Simons Observatory: the Large Aperture Telescope Receiver (LATR) integration and validation results". In: *Millimeter, Submillimeter, and Far-Infrared Detectors and Instrumentation for Astronomy X*. ed. by Jonas Zmuidzinas and Jian-Rong Gao. Vol. 11453. Society of Photo-Optical Instrumentation Engineers (SPIE) Conference Series. Dec. 2020, 1145315, p. 1145315. DOI: 10.1117/12.2576151. arXiv: 2012.07862 [astro-ph.IM]

Joseph Seibert, Peter Ade, Aamir M. Ali, Kam Arnold, Nicholas F. Cothard, Nicholas Galitzki, Kathleen Harrington, Shuay-Pwu Patty Ho, Brian Keating, Lindsay Ng. Lowry, Megan Russell, Maximiliano Silva-Feaver, Praween Siritanasak, Grant P. Teply, Carole Tucker, Eve M. Vavagiakis, and Zhilei Xu. "Development of an optical detector testbed for the Simons Observatory". In: *Millimeter, Submillimeter, and Far-Infrared Detectors and Instrumentation for Astronomy X*. ed. by Jonas Zmuidzinas and Jian-Rong Gao. Vol. 11453. International Society for Optics and Photonics. SPIE, 2020, p. 114532C. DOI: 10.1117/12.2562045. URL: https://doi.org/10.1117/12.2562045

Mayuri Sathyanarayana Rao, Maximiliano Silva-Feaver, Aamir Ali, Kam Arnold, Peter Ashton, Bradley J. Dober, Cody J. Duell, Shannon M. Duff, Nicholas Galitzki, Erin Healy, Shawn Henderson, Shuay-Pwu Patty Ho, Jonathan Hoh, Anna M. Kofman, Akito Kusaka, Adrian T. Lee, Aashrita Mangu, Justin Mathewson, Philip Mauskopf, Heather McCarrick, Jenna Moore, Michael D. Niemack, Christopher Raum, Maria Salatino, Trevor Sasse, Joseph Seibert, Sara M. Simon, Suzanne Staggs, Jason R. Stevens, Grant Teply, Robert Thornton, Joel Ullom, Eve M. Vavagiakis, Benjamin Westbrook, Zhilei Xu, and Ningfeng Zhu. "Simons Observatory Microwave SQUID Multiplexing Readout: Cryogenic RF Amplifier and Coaxial Chain Design". In: *Journal of Low Temperature Physics* 199.3-4 (Mar. 2020), pp. 807–816. DOI: 10.1007/s10909-020-02429-y. arXiv: 2003.08949 [astro-ph.IM]

Aamir M. Ali, Shunsuke Adachi, Kam Arnold, Peter Ashton, Andrew Bazarko, Yuji Chinone, Gabriele Coppi, Lance Corbett, Kevin D. Crowley, Kevin T. Crowley, Mark Devlin, Simon Dicker, Shannon Duff, Chris Ellis, Nicholas Galitzki, Neil Goeckner-Wald, Kathleen Harrington,

Erin Healy, Charles A. Hill, Shuay-Pwu Patty Ho, Johannes Hubmayr, Brian Keating, Kenji Kiuchi, Akito Kusaka, Adrian T. Lee, Michael Ludlam, Aashrita Mangu, Frederick Matsuda, Heather McCarrick, Federico Nati, Michael D. Niemack, Haruki Nishino, John Orlowski-Scherer, Mayuri Sathyanarayana Rao, Christopher Raum, Yuki Sakurai, Maria Salatino, Trevor Sasse, Joseph Seibert, Carlos Sierra, Maximiliano Silva-Feaver, Jacob Spisak, Sara M. Simon, Suzanne Staggs, Osamu Tajima, Grant Teply, Tran Tsan, Edward Wollack, Bejamin Westbrook, Zhilei Xu, Mario Zannoni, and Ningfeng Zhu. "Small Aperture Telescopes for the Simons Observatory". In: *Journal of Low Temperature Physics* 200.5-6 (Apr. 2020), pp. 461–471. DOI: 10.1007/s10909-020-02430-5. arXiv: 2001.07848 [astro-ph.IM]

Adrian Lee, Maximilian H. Abitbol, Shunsuke Adachi, Peter Ade, James Aguirre, Zeeshan Ahmed, Simone Aiola, Aamir Ali, David Alonso, Marcelo A. Alvarez, Kam Arnold, Peter Ashton, Zachary Atkins, Jason Austermann, Humna Awan, Carlo Baccigalupi, Taylor Baildon, Anton Baleato Lizancos, Darcy Barron, Nick Battaglia, Richard Battye, Eric Baxter, Andrew Bazarko, James A. Beall, Rachel Bean, Dominic Beck, Shawn Beckman, Benjamin Beringue, Tanay Bhandarkar, Sanah Bhimani, Federico Bianchini, Steven Boada, David Boettger, Boris Bolliet, J. Richard Bond, Julian Borrill, Michael L. Brown, Sarah Marie Bruno, Sean Bryan, Erminia Calabrese, Victoria Calafut, Paolo Calisse, Julien Carron, Fred. M. Carl, Juan Cayuso, Anthony Challinor, Grace Chesmore, Yuji Chinone, Jens Chluba, Hsiao-Mei Sherry Cho, Steve Choi, Susan Clark, Philip Clarke, Carlo Contaldi, Gabriele Coppi, Nicholas F. Cothard, Kevin Coughlin, Will Coulton, Devin Crichton, Kevin D. Crowley, Kevin T. Crowley, Ari Cukierman, John M. DÉwart, Rolando Dünner, Tijmen de Haan, Mark Devlin, Simon Dicker, Bradley Dober, Cody J. Duell, Shannon Duff, Adri Duivenvoorden, Jo Dunkley, Hamza El Bouhargani, Josquin Errard, Giulio Fabbian, Stephen Feeney, James Fergusson, Simone Ferraro, Pedro Fluxa, Katherine Freese, Josef C. Frisch, Andrei Frolov, George Fuller, Nicholas Galitzki, Patricio A. Gallardo, Jose Tomas Galvez Ghersi, Jiansong Gao, Eric Gawiser, Martina Gerbino, Vera Gluscevic, Neil Goeckner-Wald, Joseph Golec, Sam Gordon, Megan Gralla, Daniel Green, Arpi Grigorian, John Groh, Chris Groppi, Yilun Guan, Jon E. Gudmundsson, Mark Halpern, Dongwon Han, Peter Hargrave, Kathleen Harrington, Masaya Hasegawa, Matthew Hasselfield, Makoto Hattori, Victor Haynes, Masashi Hazumi, Erin Healy, Shawn W. Henderson, Brandon Hensley, Carlos Hervias-Caimapo, Charles A. Hill, J. Colin Hill, Gene Hilton, Matt Hilton, Adam D. Hincks, Gary Hinshaw, Renee Hložek, Shirley Ho, Shuay-Pwu Patty Ho, Thuong D. Hoang, Jonathan Hoh, Selim C. Hotinli, Zhiqi Huang, Johannes Hubmayr, Kevin Huffenberger, John P. Hughes, Anna Ijjas, Margaret Ikape, Kent Irwin, Andrew H. Jaffe, Bhuvnesh Jain, Oliver Jeong, Matthew Johnson, Daisuke Kaneko, Ethan D. Karpel, Nobuhiko Katayama, Brian Keating, Reijo Keskitalo, Theodore Kisner, Kenji Kiuchi, Jeff Klein, Kenda Knowles, Anna Kofman, Brian Koopman, Arthur Kosowsky, Nicoletta Krachmalnicoff, Akito Kusaka, Paul La Plante, Jacob Lashner, Adrian Lee, Eunseong Lee, Antony Lewis, Yaqiong Li, Zack Li, Michele Limon, Eric Linder, Jia Liu, Carlos Lopez-Caraballo, Thibaut Louis, Marius Lungu, Mathew Madhavacheril, Daisy Mak, Felipe Maldonado, Hamdi Mani, Ben Mates, Frederick Matsuda, Loic Maurin, Phil Mauskopf, Andrew May, Nialh McCallum, Heather McCarrick, Chris McKenney, Jeff McMahon, P. Daniel Meerburg, James Mertens, Joel Meyers, Amber Miller, Mark Mirmelstein, Kavilan Moodley, Jenna Moore, Moritz Munchmeyer, Charles Munson, Masaaki Murata, Sigurd Naess, Toshiya Namikawa, Federico Nati, Martin Navaroli, Laura Newburgh, Ho Nam Nguyen,

Andrina Nicola, Mike Niemack, Haruki Nishino, Yume Nishinomiya, John Orlowski-Scherer, Luca Pagano, Bruce Partridge, Francesca Perrotta, Phumlani Phakathi, Lucio Piccirillo, Elena Pierpaoli, Giampaolo Pisano, Davide Poletti, Roberto Puddu, Giuseppe Puglisi, Chris Raum, Christian L. Reichardt, Mathieu Remazeilles, Yoel Rephaeli, Dominik Riechers, Felipe Rojas, Aditya Rotti, Anirban Roy, Sharon Sadeh, Yuki Sakurai, Maria Salatino, Mayuri Sathyanarayana Rao, Lauren Saunders, Emmanuel Schaan, Marcel Schmittfull, Neelima Sehgal, Joseph Seibert, Uros Seljak, Paul Shellard, Blake Sherwin, Meir Shimon, Carlos Sierra, Jonathan Sievers, Cristobal Sifon, Precious Sikhosana, Maximiliano Silva-Feaver, Sara M. Simon, Adrian Sinclair, Kendrick Smith, Wuhyun Sohn, Rita Sonka, David Spergel, Jacob Spisak, Suzanne T. Staggs, George Stein, Jason R. Stevens, Radek Stompor, Aritoki Suzuki, Osamu Tajima, Satoru Takakura, Grant Teply, Daniel B. Thomas, Ben Thorne, Robert Thornton, Hy Trac, Jesse Treu, Calvin Tsai, Carole Tucker, Joel Ullom, Sunny Vagnozzi, Alexander van Engelen, Jeff Van Lanen, Daniel D. Van Winkle, Eve M. Vavagiakis, Clara Vergès, Michael Vissers, Kasey Wagoner, Samantha Walker, Yuhan Wang, Jon Ward, Ben Westbrook, Nathan Whitehorn, Jason Williams, Joel Williams, Edward Wollack, Zhilei Xu, Siavash Yasini, Edward Young, Byeonghee Yu, Cyndia Yu, Fernando Zago, Mario Zannoni, Hezi Zhang, Kaiwen Zheng, Ningfeng Zhu, and Andrea Zonca. "The Simons Observatory". In: *Bulletin of the American Astronomical Society*. Vol. 51. Sept. 2019, 147, p. 147. DOI: 10.48550/arXiv.1907.08284. arXiv: 1907.08284 [astro-ph.IM]

F. Matsuda, L. Lowry, A. Suzuki, M. Aguilar Fáundez, K. Arnold, D. Barron, F. Bianchini, K. Cheung, Y. Chinone, T. Elleflot, G. Fabbian, N. Goeckner-Wald, M. Hasegawa, D. Kaneko, N. Katayama, B. Keating, A. T. Lee, M. Navaroli, H. Nishino, H. Paar, G. Puglisi, P. L. Richards, J. Seibert, P. Siritanasak, O. Tajima, S. Takatori, C. Tsai, and B. Westbrook. "The POLARBEAR Fourier transform spectrometer calibrator and spectroscopic characterization of the POLARBEAR instrument". In: *Review of Scientific Instruments* 90.11, 115115 (Nov. 2019), p. 115115. DOI: 10.1063/1.5095160. arXiv: 1904.02901 [astro-ph.IM]

Peter Ade, James Aguirre, Zeeshan Ahmed, Simone Aiola, Aamir Ali, David Alonso, Marcelo A. Alvarez, Kam Arnold, Peter Ashton, Jason Austermann, Humna Awan, Carlo Baccigalupi, Taylor Baildon, Darcy Barron, Nick Battaglia, Richard Battye, Eric Baxter, Andrew Bazarko, James A. Beall, Rachel Bean, Dominic Beck, Shawn Beckman, Benjamin Beringue, Federico Bianchini, Steven Boada, David Boettger, J. Richard Bond, Julian Borrill, Michael L. Brown, Sarah Marie Bruno, Sean Bryan, Erminia Calabrese, Victoria Calafut, Paolo Calisse, Julien Carron, Anthony Challinor, Grace Chesmore, Yuji Chinone, Jens Chluba, Hsiao-Mei Sherry Cho, Steve Choi, Gabriele Coppi, Nicholas F. Cothard, Kevin Coughlin, Devin Crichton, Kevin D. Crowley, Kevin T. Crowley, Ari Cukierman, John M. DÉwart, Rolando Dünner, Tijmen de Haan, Mark Devlin, Simon Dicker, Joy Didier, Matt Dobbs, Bradley Dober, Cody J. Duell, Shannon Duff, Adri Duivenvoorden, Jo Dunkley, John Dusatko, Josquin Errard, Giulio Fabbian, Stephen Feeney, Simone Ferraro, Pedro Fluxà, Katherine Freese, Josef C. Frisch, Andrei Frolov, George Fuller, Brittany Fuzia, Nicholas Galitzki, Patricio A. Gallardo, Jose Tomas Galvez Ghersi, Jiansong Gao, Eric Gawiser, Martina Gerbino, Vera Gluscevic, Neil Goeckner-Wald, Joseph Golec, Sam Gordon, Megan Gralla, Daniel Green, Arpi Grigorian, John Groh, Chris Groppi, Yilun Guan, Jon E. Gudmundsson, Dongwon Han, Peter Hargrave, Masaya Hasegawa,

Matthew Hasselfield, Makoto Hattori, Victor Haynes, Masashi Hazumi, Yizhou He, Erin Healy, Shawn W. Henderson, Carlos Hervias-Caimapo, Charles A. Hill, J. Colin Hill, Gene Hilton, Matt Hilton, Adam D. Hincks, Gary Hinshaw, Renée Hložek, Shirley Ho, Shuay-Pwu Patty Ho, Logan Howe, Zhiqi Huang, Johannes Hubmayr, Kevin Huffenberger, John P. Hughes, Anna Ijjas, Margaret Ikape, Kent Irwin, Andrew H. Jaffe, Bhuvnesh Jain, Oliver Jeong, Daisuke Kaneko, Ethan D. Karpel, Nobuhiko Katayama, Brian Keating, Sarah S. Kernasovskiy, Reijo Keskitalo, Theodore Kisner, Kenji Kiuchi, Jeff Klein, Kenda Knowles, Brian Koopman, Arthur Kosowsky, Nicoletta Krachmalnicoff, Stephen E. Kuenstner, Chao-Lin Kuo, Akito Kusaka, Jacob Lashner, Adrian Lee, Eunseong Lee, David Leon, Jason S. -Y. Leung, Antony Lewis, Yaqiong Li, Zack Li, Michele Limon, Eric Linder, Carlos Lopez-Caraballo, Thibaut Louis, Lindsay Lowry, Marius Lungu, Mathew Madhavacheril, Daisy Mak, Felipe Maldonado, Hamdi Mani, Ben Mates, Frederick Matsuda, Loic Maurin, Phil Mauskopf, Andrew May, Nialh McCallum, Chris McKenney, Jeff McMahon, P. Daniel Meerburg, Joel Meyers, Amber Miller, Mark Mirmelstein, Kavilan Moodley, Moritz Munchmeyer, Charles Munson, Sigurd Naess, Federico Nati, Martin Navaroli, Laura Newburgh, Ho Nam Nguyen, Michael Niemack, Haruki Nishino, John Orlowski-Scherer, Lyman Page, Bruce Partridge, Julien Peloton, Francesca Perrotta, Lucio Piccirillo, Giampaolo Pisano, Davide Poletti, Roberto Puddu, Giuseppe Puglisi, Chris Raum, Christian L. Reichardt, Mathieu Remazeilles, Yoel Rephaeli, Dominik Riechers, Felipe Rojas, Anirban Roy, Sharon Sadeh, Yuki Sakurai, Maria Salatino, Mayuri Sathyanarayana Rao, Emmanuel Schaan, Marcel Schmittfull, Neelima Sehgal, Joseph Seibert, Uros Seljak, Blake Sherwin, Meir Shimon, Carlos Sierra, Jonathan Sievers, Precious Sikhosana, Maximiliano Silva-Feaver, Sara M. Simon, Adrian Sinclair, Praween Siritanasak, Kendrick Smith, Stephen R. Smith, David Spergel, Suzanne T. Staggs, George Stein, Jason R. Stevens, Radek Stompor, Aritoki Suzuki, Osamu Tajima, Satoru Takakura, Grant Teply, Daniel B. Thomas, Ben Thorne, Robert Thornton, Hy Trac, Calvin Tsai, Carole Tucker, Joel Ullom, Sunny Vagnozzi, Alexander van Engelen, Jeff Van Lanen, Daniel D. Van Winkle, Eve M. Vavagiakis, Clara Vergès, Michael Vissers, Kasey Wagoner, Samantha Walker, Jon Ward, Ben Westbrook, Nathan Whitehorn, Jason Williams, Joel Williams, Edward J. Wollack, Zhilei Xu, Byeonghee Yu, Cyndia Yu, Fernando Zago, Hezi Zhang, Ningfeng Zhu, and Simons Observatory Collaboration. "The Simons Observatory: science goals and forecasts". In: *Journal of Cosmology and Astrophysics* 2019.2, 056 (Feb. 2019), p. 056. DOI: 10.1088/1475-7516/2019/02/056. arXiv: 1808.07445 [astro-ph.CO]

Nicholas Galitzki, Aamir Ali, Kam S. Arnold, Peter C. Ashton, Jason E. Austermann, Carlo Baccigalupi, Taylor Baildon, Darcy Barron, James A. Beall, Shawn Beckman, Sarah Marie M. Bruno, Sean Bryan, Paolo G. Calisse, Grace E. Chesmore, Yuji Chinone, Steve K. Choi, Gabriele Coppi, Kevin D. Crowley, Kevin T. Crowley, Ari Cukierman, Mark J. Devlin, Simon Dicker, Bradley Dober, Shannon M. Duff, Jo Dunkley, Giulio Fabbian, Patricio A. Gallardo, Martina Gerbino, Neil Goeckner-Wald, Joseph E. Golec, Jon E. Gudmundsson, Erin E. Healy, Shawn Henderson, Charles A. Hill, Gene C. Hilton, Shuay-Pwu Patty Ho, Logan A. Howe, Johannes Hubmayr, Oliver Jeong, Brian Keating, Brian J. Koopman, Kenji Kiuchi, Akito Kusaka, Jacob Lashner, Adrian T. Lee, Yaqiong Li, Michele Limon, Marius Lungu, Frederick Matsuda, Philip D. Mauskopf, Andrew J. May, Nialh McCallum, Jeff McMahon, Federico Nati, Michael D. Niemack, John L. Orlowski-Scherer, Stephen C. Parshley, Lucio Piccirillo, Mayuri Sathyanarayana Rao, Christopher Raum, Maria Salatino, Joseph S. Seibert, Carlos

Sierra, Max Silva-Feaver, Sara M. Simon, Suzanne T. Staggs, Jason R. Stevens, Aritoki Suzuki, Grant Teply, Robert Thornton, Calvin Tsai, Joel N. Ullom, Eve M. Vavagiakis, Michael R. Vissers, Benjamin Westbrook, Edward J. Wollack, Zhilei Xu, and Ningfeng Zhu. "The Simons Observatory: instrument overview". In: *Millimeter, Submillimeter, and Far-Infrared Detectors and Instrumentation for Astronomy IX*. ed. by Jonas Zmuidzinas and Jian-Rong Gao. Vol. 10708. Society of Photo-Optical Instrumentation Engineers (SPIE) Conference Series. July 2018, 1070804, p. 1070804. DOI: 10.1117/12.2312985. arXiv: 1808.04493 [astro-ph.IM]

ABSTRACT OF THE DISSERTATION

Integration and Validation of the Simons Observatory Small Aperture Telescope

by

Joseph Sloane Seibert

Doctor of Philosophy in Physics

University of California San Diego, 2023

Professor Kam Arnold, Chair

Measurements of the polarization of the cosmic microwave background (CMB) provide powerful probes of early-universe physics and cosmology, including for evidence of cosmic inflation. The Simons Observatory (SO) is a ground-based survey experiment designed to measure the CMB polarization signal using three small aperture telescopes (SATs) and one large aperture telescope (LAT) from the Atacama Desert in Chile. In order to achieve the required sensitivity, SO will field over 60,000 transition edge sensor (TES) bolometers in six spectral bands ranging from 27 to 280 GHz. Before being installed into the receivers, the detectors' dark and optical properties must be characterized in in-lab testbeds. A testbed specifically focused on optical characterization of the detector modules was developed at UC San Diego, along with

required test equipment to enable these measurements. Following this, detector modules were integrated into the full receiver, where we perform final validation. The first-light instrument for SO, the first SAT, was integrated at UC San Diego, where we characterized the instrument beam, spectral properties, and polarization performance, among other tests. The testing, as well as field operation, requires new software implementation for detector control and analysis, as well as metadata packaging for science-grade analysis. These software packages were developed and tested during the lab testing program described here, both in the optical testbed and the fully integrated SAT cryogenic receiver.

Chapter 1

Introduction

This chapter begins with a basic description of the standard model of cosmology and the physics of general relativity that underpins it. What follows is a discussion of the cosmic microwave background (CMB), a topic rich with theoretical and experimental implications. The current focus is on measurements of CMB polarization, with the intent to learn even more about the evolution of the universe in its earliest days. In general, we will follow [1] for much of the discussion of cosmological theory.

This theory-based introduction sets the stage for the remaining chapters, which focus on the construction of a state-of-the-art observatory focused on measuring the CMB polarization. Chapter 2 describes the Simons Observatory and gives an overview of the instruments designed and built for this purpose. Chapter 3 is a deeper dive into the detector technology employed, focused towards characterizing the detector parameters and noise properties in the context of their observational use. Chapter 4 describes the development of a detector testbed at UCSD, designed to provide a location to do full-scale detector characterization, including measurements of their optical response. Chapter 5 outlines the optical characterization of the first light instrument for Simons Observatory, built and validated at UCSD. Finally, Chapter 6 details some of the software development efforts for control, characterization, data processing, and pipeline elements specifically related to the detector and readout technology employed by Simons Observatory.

Simons Observatory is a large, international collaboration with many contributors. After

the introductory material in chapters 1-3, chapters 4-6 in this dissertation describe the individual contributions that I made to the project, with a particular focus on detector and optical characterization of the first light instrument for the project, and general pipeline and data acquisition software elements for detector and readout control across the entire project.

1.1 Standard Model of Cosmology

In general relativity, spacetime can be described by the Einstein Field Equations:

$$R_{\mu\nu} - \frac{1}{2} g_{\mu\nu} R - \Lambda g_{\mu\nu} = 8\pi G T_{\mu\nu} \tag{1.1}$$

where $R_{\mu\nu}$ and R are the Ricci curvature tensor and scalar, respectively, $g_{\mu\nu}$ is the metric tensor, and $T_{\mu\nu}$ is the stress-energy tensor. Λ is the so-called cosmological constant, which will become useful to consider from a cosmological perspective. The Ricci tensor and scalar only depend on the metric tensor and its first and second derivatives, which in itself is a description of the coordinate space. The stress-energy tensor describes the energy and momentum in a particular region of spacetime. Thus, in the simplest summary, equation 1.1 describes how spacetime changes in response to the presence of matter. (Note that above, we have chosen the unit basis where the speed of light is set to 1.)

The implication of the cosmological principle is that the universe, on large scales, is isotropic and homogenous. That leads us to be able to write down the Friedmann-Lemaître-Robertson-Walker (FLRW) metric:

$$ds^2 = -dt^2 + a^2(t)\delta_{ij} dx^i dx^j \tag{1.2}$$

which is expressed in matrix form as

$$g_{\mu\nu} = \begin{pmatrix} -1 & 0 & 0 & 0 \\ 0 & a^2(t) & 0 & 0 \\ 0 & 0 & a^2(t) & 0 \\ 0 & 0 & 0 & a^2(t) \end{pmatrix} \tag{1.3}$$

where $a(t)$ is defined as the scale-factor of the universe, a parameter that describes the size of an expanding universe as a function of time.

In the similar isotropic and homogeneous universe, we can write the stress-energy tensor in the form of a perfect isotropic fluid:

$$T^{\mu}{}_{\nu} = \begin{pmatrix} -\rho & 0 & 0 & 0 \\ 0 & P & 0 & 0 \\ 0 & 0 & P & 0 \\ 0 & 0 & 0 & P \end{pmatrix} \tag{1.4}$$

where ρ is the energy density and P is the pressure.

Plugging in the FLRW metric and the stress-energy tensor to equation 1.1 yields the following equations from the temporal and spatial portions, respectively:

$$\left(\frac{\dot{a}}{a}\right)^2 = \frac{8\pi G}{3}\rho - \frac{k}{a^2} + \frac{\Lambda}{3} \tag{1.5}$$

$$\frac{\ddot{a}}{a} = -\frac{4\pi G}{3}(\rho + 3P) + \frac{\Lambda}{3}, \tag{1.6}$$

where k is a parameter describing the curvature of the universe. It is common to simplify these equations by considering the cosmological constant term as a contribution to the energy density by the substitutions

$$\rho \to \rho - \frac{\Lambda}{8\pi G} \tag{1.7}$$

$$P \to P + \frac{\Lambda}{8\pi G}, \tag{1.8}$$

which turn equations 1.5 and 1.6 into

$$H^2 \equiv \left(\frac{\dot{a}}{a}\right)^2 = \frac{8\pi G}{3}\rho - \frac{k}{a^2} \tag{1.9}$$

$$\frac{\ddot{a}}{a} = -\frac{4\pi G}{3}(\rho + 3P). \tag{1.10}$$

These two equations are often referred to as the Friedmann equations, and they describe the evolution of an isotropic and homogenous universe. Here, also, the Hubble parameter H is defined.

Enforcing energy conservation via the continuity equation $\nabla_\mu T^\mu{}_\nu = 0$ gives us the following relationship:

$$\dot{\rho} + 3\frac{\dot{a}}{a}(\rho + P) = 0. \tag{1.11}$$

We can now parameterize the fluid as having an equation of state of the form $P = w\rho$, where the value of w varies depending on the type of energy we are discussing. This allows us to write down the energy density as a function of the scale factor:

$$\frac{\rho}{\rho_0} = a^{-3(1+w)}. \tag{1.12}$$

The subscript 0 indicates the value of the energy density today. For the cold, non-relativistic matter (both baryonic and dark matter), relativistic matter, and dark energy, $w = 0, 1/3,$ and -1, respectively.

Now, we can define a critical density ρ_c where the spatial geometry is flat by solving equation 1.9 with $k = 0$. That yields $\rho_c = \frac{3H^2}{8\pi G}$. We can use the critical density to define a

dimensionless energy density $\Omega = \rho/\rho_c$, which allows us to simply equation 1.9 even further, using 1.12, and yields

$$\frac{H^2}{H_0^2} = \Omega_{0,R}a^{-4} + \Omega_{0,M}a^{-3} + \Omega_{0,k}a^{-2} + \Omega_{0,\Lambda}. \tag{1.13}$$

The subscript 0 again indicates the value of the parameter at modern day (i.e. $a = 1$). This way of expressing the first Friedmann equation makes it more immediately obvious how the evolution of the universe depends on the constituent parts of the total energy content. In addition, it demonstrates that each individual portion's contribution to the total energy density varies as a function of scale factor and indicates that at different eras of the universe (often parametrized by redshift $z \equiv (1-a)/a$), the total energy density was dominated by a different constituent. Early in the universe, the relativistic species (largely photons and neutrinos) were the dominant portion. At $z \sim 3400$, non-relativistic matter (baryons and dark matter) began to dominate. Finally, at $z \sim 0.3$, dark energy became dominant, since it has a constant energy density.

Best estimates of the modern day energy densities from measurements of the CMB, which we will discuss in more detail in section 1.2, have $\Omega_{0,R} \sim 2.4 \times 10^{-5}$, $\Omega_{0,M} \sim 0.3$, $\Omega_{0,k} \sim 0$, $\Omega_{0,\Lambda} \sim 0.7$ [2]. The value of $\Omega_{0,k}$ indicates that the universe is very spatially flat, and the values of the other Ω_0 demonstrate the dominance of the dark energy portion of the energy density. From these measurements, we can also estimate the age of the universe to be roughly 13.7 billion years old.

1.2 Cosmic Microwave Background

1.2.1 Surface of Last Scattering

Early in its evolution, the universe is extremely hot and dense. As soon as expansion begins, the average energy of particles in the universe decreases, which leads to a shift in interactions over time, and a variety of physical phenomena emerge.

For a population in thermal equilibrium (a reasonable assumption for photons and baryons

at this stage of cosmic evolution), the distribution function according to statistical mechanics can be described by

$$f(t,\mathbf{x},\mathbf{p}) = f(t,p) = \frac{1}{e^{(E(p)-\mu)/T} \pm 1} \tag{1.14}$$

where the $\pm$ denotes fermions and bosons, respectively, with energy E and momentum p in equilibrium with a chemical potential *mu* at temperature T. We can use the distribution function to write down expressions for number and energy density:

$$n = \frac{g}{(2\pi)^3} \int d^3p f(p) \tag{1.15}$$

$$\rho = \frac{g}{(2\pi)^3} \int d^3p f(p) E(p) \tag{1.16}$$

where g denotes the degeneracy of the particle species in question. For massive particles, $E = m$, and their contribution to the total energy and number density is suppressed while $T >> m$, which is true in the early stages of expansion. However, for relativistic particles, in particular photons, $g = 2$ and $E = p = \omega = 2\pi\nu$, where ν is the frequency of the photon. Once we plug those values in, we can see that the photons in the early universe constitute a blackbody, described by

$$B_\nu(T) = \frac{1}{4\pi}\frac{d\rho}{d\nu} = \frac{4\pi\nu^3}{e^{(2\pi\nu)/T} - 1}. \tag{1.17}$$

The majority of matter present during these early periods was comprised of protons and electrons. From an energetic perspective, the two favored interactions are protons and electrons forming neutral hydrogen, and photons scattering off electrons via Thomson scattering.

Inititially, due to the abundance of high-energy photons, the total amount of neutral hydrogen is relatively low. However, as expansion continues and the temperature of the plasma drops below 1 eV, it becomes possible for neutral hydrogen to form in greater quantities, since

the photon energies are lower. The increase in the amount of neutral hydrogen is inversely proportional to the abundance of free electrons, which means the number of particles for the photons to interact with dramatically decreases. Eventually, the number density of electrons decreases enough such that the rate of Thomson scattering is less than the Hubble parameter, and the photon blackbody decouples from the baryonic matter completely and begins to freestream. This happens at $z \sim 1100$, when the temperature is roughly 0.3 eV, and the free-streaming photons form what we call the CMB [1]. The redshift at which the photons decoupled from the baryonic matter is the so-called surface of last scattering. Thus, any measurement of the properties of the CMB can provide a probe for the state of the universe at the surface of last scattering, and is the most powerful of any tool to discover properties of the early universe.

1.2.2 Temperature Anisotropies

As the universe continues to expand, the photons comprising the CMB redshift according to equation 1.13, i.e. as a^{-4}. Measurements of the CMB by the FIRAS instrument on the COBE satellite [3] show that the CMB is very well-described by a blackbody, as expected from equation 1.17, radiating at 2.725 K with a frequency of maximum radiation intensity of 160 GHz (roughly 2 mm wavelength), which is firmly in the microwave section of the electromagnetic spectrum, hence the name. The agreement between the CMB and a blackbody is good to 1 part in 10^5. This anisotropy of the CMB describes how the CMB photons were affected by over- and under-densities of matter at and before the surface of last scattering. Quantifying the amount of anisotropy present at different angular scales is the method by which we can estimate the values of the cosmological parameters, as alluded to in section 1.1.

If we consider the surface of last scattering as a sphere projected around the Earth (our arbitrary location as an observer) upon which we observe the CMB signal, we can decompose the projected signal in terms of the spherical harmonics $Y_{\ell m}(\hat{n})$, where ℓ is the multipole number inversely proportional to angular scale on the sky, m is the azimuthal number, and $\hat{n}$ represents a particular point on the sphere [4]. The temperature at a particular point can be given by

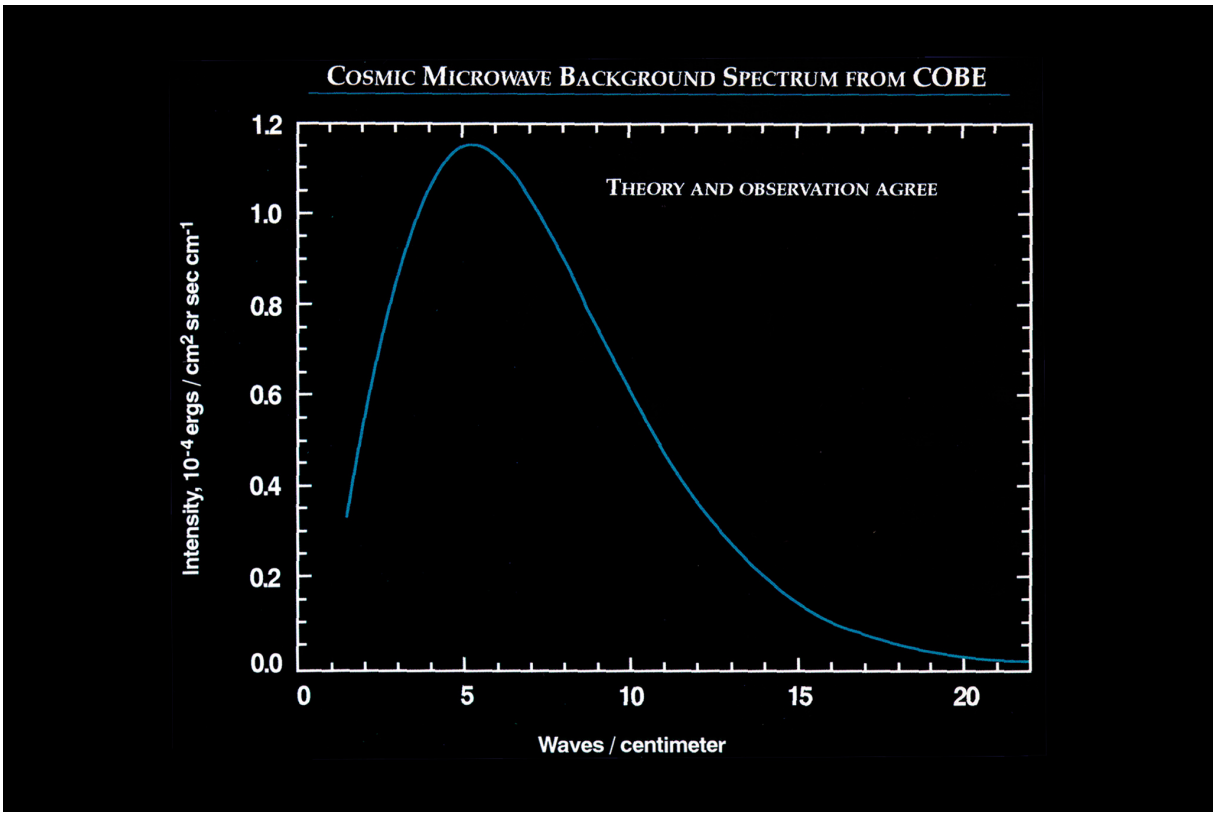

Figure 1.1. Measurements by the FIRAS instrument on the COBE satellite measured the spectral emission of the CMB and showed the near-perfect agreement with a theoretical blackbody at 2.725 K. Figure courtesy of the NASA Lambda archive.

$$T(\hat{n}) = \sum_{\ell m} a_{\ell m} Y_{\ell m}(\hat{n}) \tag{1.18}$$

where $a_{\ell m}$ is the amplitude of the particular spherical harmonic.

It is now helpful to construct an angular power spectrum as a function of multipole on the sky. The values of the power spectrum are given by

$$C_\ell = \frac{1}{2\ell+1} \sum_m a^*_{\ell m} a_{\ell m}. \tag{1.19}$$

The sum over the azimuthal number m is necessary because of the cosmological principle. The properties of the universe should not depend on the perspective of a particular observer. By summing over m, we remove the observer-dependent $Y_{\ell m}$ in lieu of the observer-independent C_ℓ.

The monopole moment ($\ell = 0$) is simply the mean temperature of the CMB. The observed dipole moment ($\ell = 1$) is an effect of the motion of the Earth through the CMB during measurement, which dominates any primordial signal.

All the primordial information from the surface of last scattering is found at the higher multipole moments ($\ell \geq 2$). Figure 1.2 shows the measured angular power spectrum from the Planck experiment [2]. The amplitude of the various peaks, as well as their location in angular space, communicates various information about the cosmological parameters than can be extracted. For example, the location of the first peak demonstrates that the universe is very close to flat (i.e. $\Omega_{0,k} \approx 0$, as stated in section 1.1). The ratio of the peak amplitudes tells us the portion of the total non-relativistic matter made up of baryons, and the third peak tells us how much of the non-relativistic matter is made up of dark matter. The fall off at higher angular scales is an effect of damping from radiation and can be used as a constraint on the energy density of relativistic neutrinos in the early universe. The angular power spectrum of the temperature anisotropies is an incredibly powerful probe of early universe physics.

1.3 Inflation

There are two main problems with the CMB in the model presented above. The first is known as the Horizon Problem, and is a statement that the isotropy shown in measurements of the CMB imply that two distant points were causally connected in the early stages of cosmic expansion [1]. However, based on measurements of the age of the universe described above, this isn't possible, given the contraints of the speed of light. The next issue is the Flatness Problem, which stems from the measurement above that the universe is extremely flat [1]. Based on expansion rates that can be solved for from the Friedmann equations, the flat universe would require fine-tuning of cosmological parameters which is not expected from a physical model.

Both problems can be solved by the theory of cosmic inflation. Instead of the power-law expansion rate given by solutions to equation 1.13, inflation postulates that extremely early in

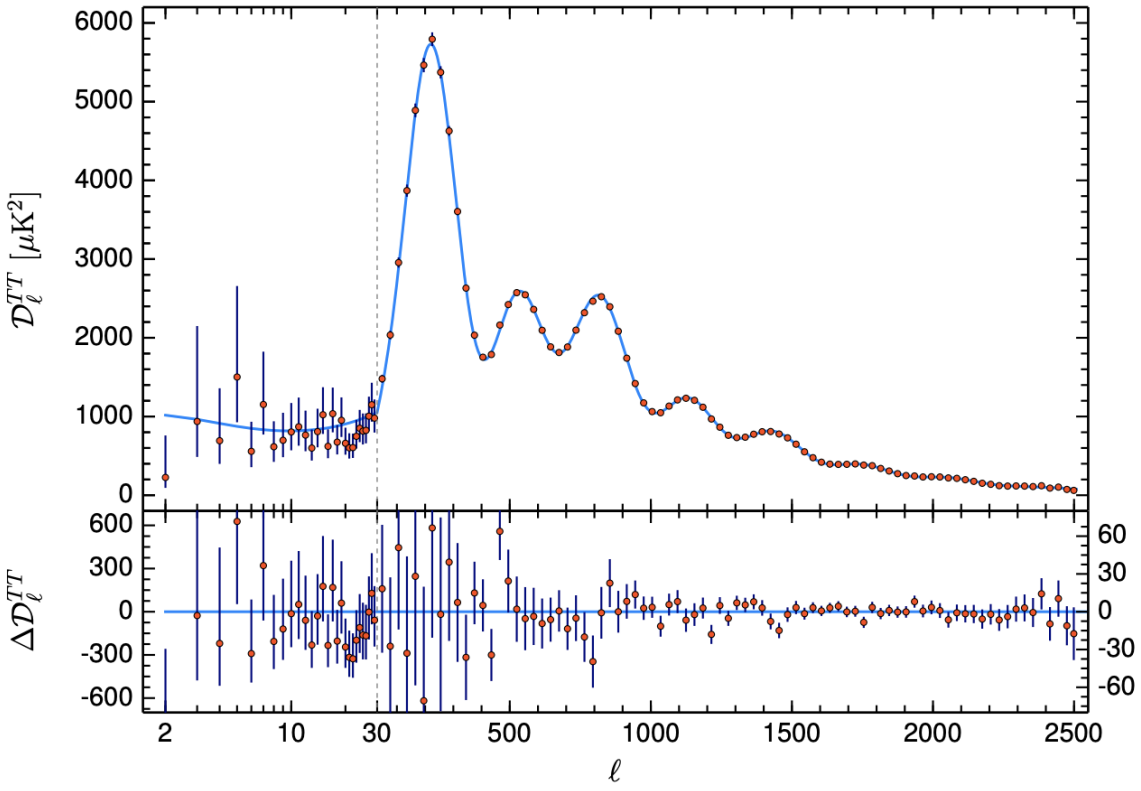

Figure 1.2. Angular power spectrum of the temperature anisotropies in the CMB, as measured by the Planck satellite. The red points are the data measured by Planck, and the blue is the fitted theory curve. Residuals between the two are plotted in the bottom panel. In the plots, $D_\ell^{TT} \equiv \frac{\ell(\ell+1)}{2\pi} C_\ell^{TT}$. Figure is courtesy of [2].

the history of the universe, there existed some scalar field that led to exponential expansion of the universe, where $a \propto e^{Ht}$ [5], [6], [7]. The exponential expansion solves both the horizon and flatness problems. Since the universe expanded so rapidly during the inflationary era, it means the entire sky was in causal contact early, providing a solution for the horizon problem. In addition, the exponential expansion flattens the universe and sends the curvature to zero, which in turn solves the flatness problem.

Inflation is a term that refers to a broad class of theories that all postulate a similar exponential expansion in the early universe, but differ in key ways, namely by describing different properties of the scalar field that would cause inflation. Given the neat way that the theory of inflation solves key questions in the cosmological model, it is important to think

of predicted observables that would allow us to not only confirm the existence of the early inflationary period, but also to narrow in on which model most accurately describes known universe. We will explore these observables in more depth in section 1.4.

1.4 CMB Polarization

It is a natural extension to wonder whether the CMB is polarized at all when it is released at the surface of last scattering. As discussed in section 1.2, the CMB photons predominantly interacted with electrons via Thomson scattering. If the scattering electron is located in a uniform, isotropic region of space, i.e. all incident photons are the same from different directions, the resultant scattered photon will be unpolarized. However, if the region is anisotropic, and the incident photons are different temperatures, the resultant scattered photon will be polarized along the cold axis. More specifically, the incident must be 90° separated from one another, so the anisotropy required to source polarization of the scattered photon must be quadrupolar in nature [8]. Figure 1.3 illustrates this difference clearly.

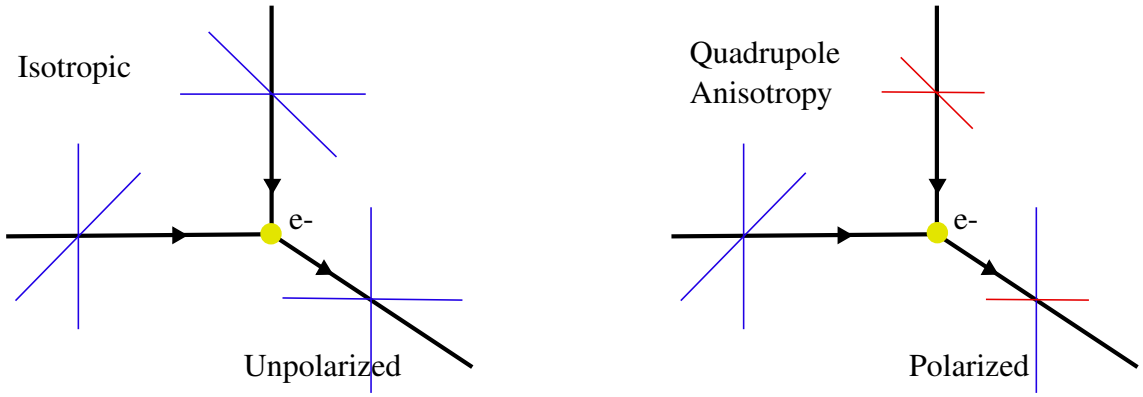

(a) Isotropy **(b)** Quadrupole anisotropy

Figure 1.3. In both figures, CMB photons interact with an electron via Thomson scattering. In 1.3a, the local area around the electron is isotropic, so the resultant scattered radiation is unpolarized. In 1.3b, there is a quadrupole anisotropy in the region around the electron which results in a net polarization in the scattered radiation.

There are two expected ways to generate local quadrupole anisotropies in the early universe: scalar and tensor perturbations. The scalar perturbations generate local density fluctuations near the electron where Thomson scattering occurs. Locally overdense and underdense regions can lead to temperature variations that will generate the necessary anisotropy to source polarization. These density fluctuations are the seeds for structure formation throughout the evolving universe. The tensor perturbations are primordial gravitational waves. The amplitude of these gravitational waves is too small to be detected by modern gravitational wave observatories, but they will generate a unique polarization signal that can be detected in the cosmic microwave background.

Both of these perturbations are generated during the inflationary era described in section 1.3. Quantum fluctuations of spacetime in the primordial universe are grown by the exponential expansion in this period, and we can write down a modification to equation 1.2 including these perturbations [9]:

$$ds^2 = -dt^2 + a^2(t)(e^{2\zeta}\delta_{ij} + \gamma_{ij})dx^i dx^j. \tag{1.20}$$

ζ are the scalar perturbations, while γ are the tensor perturbations. It is common to write down a parameter

$$r \equiv \frac{\langle \gamma\gamma \rangle}{\langle \zeta\zeta \rangle} \tag{1.21}$$

where r is the defined ratio of tensor to scalar perturbations. Different values of r are predicted in different models of inflation, so measurements of r would directly provide constraining power on which models of inflation are physically permitted based on observables.

It is informative to project the polarization anisotropies of the CMB onto the surface of last scattering, just as we did for temperature anisotropies in section 1.2.2. However, since polarization is a spin-2 vector field, we have to use spin-2 spherical harmonics for the decomposition. In terms of the Stokes parameters Q and U, the equivalent to equation 1.18 is given by [4]

$$Q(\hat{n}) - iU(\hat{n}) = \sum_{\ell=2}^{\infty} \sum_{m=-\ell}^{\ell} a^*_{P,\ell m}\, {}_2Y^*_{\ell m}(\hat{n}). \tag{1.22}$$

From here, we could follow the same procedure and generate an angular power spectrum of the the polarization anisotropies. However, the Stokes parameters require a definition of a local coordinate system, which means that depending on our choice of coordinates, the $a_{P,\ell m}$ are not rotationally invariant on the sphere, which means we cannot sum over m cleanly. So, we choose to make linear combinations of the coefficients such that they are rotationally invariant:

$$a_{E,\ell m} \equiv \frac{-(a_{P,\ell m} + a^*_{P,\ell -m})}{2} \tag{1.23}$$

$$a_{B,\ell m} \equiv \frac{i(a_{P,\ell m} - a^*_{P,\ell -m})}{2}. \tag{1.24}$$

These are the so-called E- and B-modes. As you can see, the E-modes are a curl-free pattern that is parity-even (symmetric under reflection) and the B-modes are a divergence-free pattern that is parity-odd (anti-symmetric under reflection). From these, we can generate the same angular power spectra as is done for temperature anisotropies, following the same process as equation 1.19. Current measurements of the angular power spectra can be seen in Figure 1.4.

The choice of name is meant to reflect a similar parity to the analogous electric and magnetic fields from electro- and magnetostatics, where the electric field is curl-free, and the magnetic field is divergence-free. The naming convention has no physical significance.

The other useful part about decomposing the measured polarization into E- and B-modes is that the different perturbations directly source different polarization modes. Both scalar perturbations and tensor perturbations that generate gravitational waves can generate E-modes, but B-modes are only generated by tensor perturbations [10], [11]. Since the gravitational waves generated via tensor perturbations are an unintended prediction of the inflationary paradigm, measurements of gravitational waves would be consistent with a prediction of inflation, and

could provide more information about the mechanism of inflation. The search for primordial B-modes is often phrased in terms of a measurement of a non-zero value of r, from equation 1.21 [11].

To date, experiments have only been able to place upper bounds on the value of r, and we have not yet detected primordial B-modes [12]. The only detected B-modes have been the so-called lensed B-modes, see [13], [12], which are E-modes that are shifted into B-modes via weak gravitational lensing as the photons free-stream through the gravitational structure of the evolving universe. Given the nature of these lensed B-modes, they are more prevalent at smaller angular scales, since the larger angular scales correspond to scales set earlier in cosmic history, when the CMB was released at recombination. Thus, in order to make a good measurement of the B-modes, it is important to measure the polarization of the CMB at both large and small angular scales, in order to remove the effect of the lensed B-modes, which can contribute a number of other interesting scientific measurements related to the evolution and contents of the evolving universe.

As you can see in Figure 1.4, the polarization signal is small relative to the temperature signal, and the B-mode signal itself is orders of magnitude dimmer than the E-mode signal. This highlights the need for highly sensitive experiments, specifically designed and planned to go after the extremely small signal.

1.5 Foregrounds

In addition to the strict sensitivity requirements imposed on instrument design and calibration in order to isolate the weak polarization signal in the CMB, there are spurious astrophysical signals that can leak into the polarization as well. These so-called foregrounds are highly polarized galactic signals that look like the B-mode pattern we are attempting to detect.

There are two main types of polarized foregrounds that we are concerned with: synchrotron radiation and thermal dust emission. Synchrotron radiation is generated by relativistic

electrons spiraling in the galactic magnetic field and is dominant at lower frequencies [14]. Thermal dust emission is generated by spinning, anisotropic dust grains which in turn emit polarized radiation and is dominant at higher frequencies [15]. Figure 1.5 shows the relative contribution from the foreground signals as a function of frequency.

We can take advantage of the spectral shape of the different polarized signals as a method to mitigate their effect on observations of the CMB. By observing the sky at multiple different frequencies, we can better isolate the contribution to the measured signal from the three main components: both foreground signals and the CMB itself. We observe over three main frequency ranges: at low frequencies where the synchrotron is dominant, and high frequencies where the dust is dominant, and at middle frequencies where both foreground signals are minimized and the CMB signal has the largest fractional contribution.

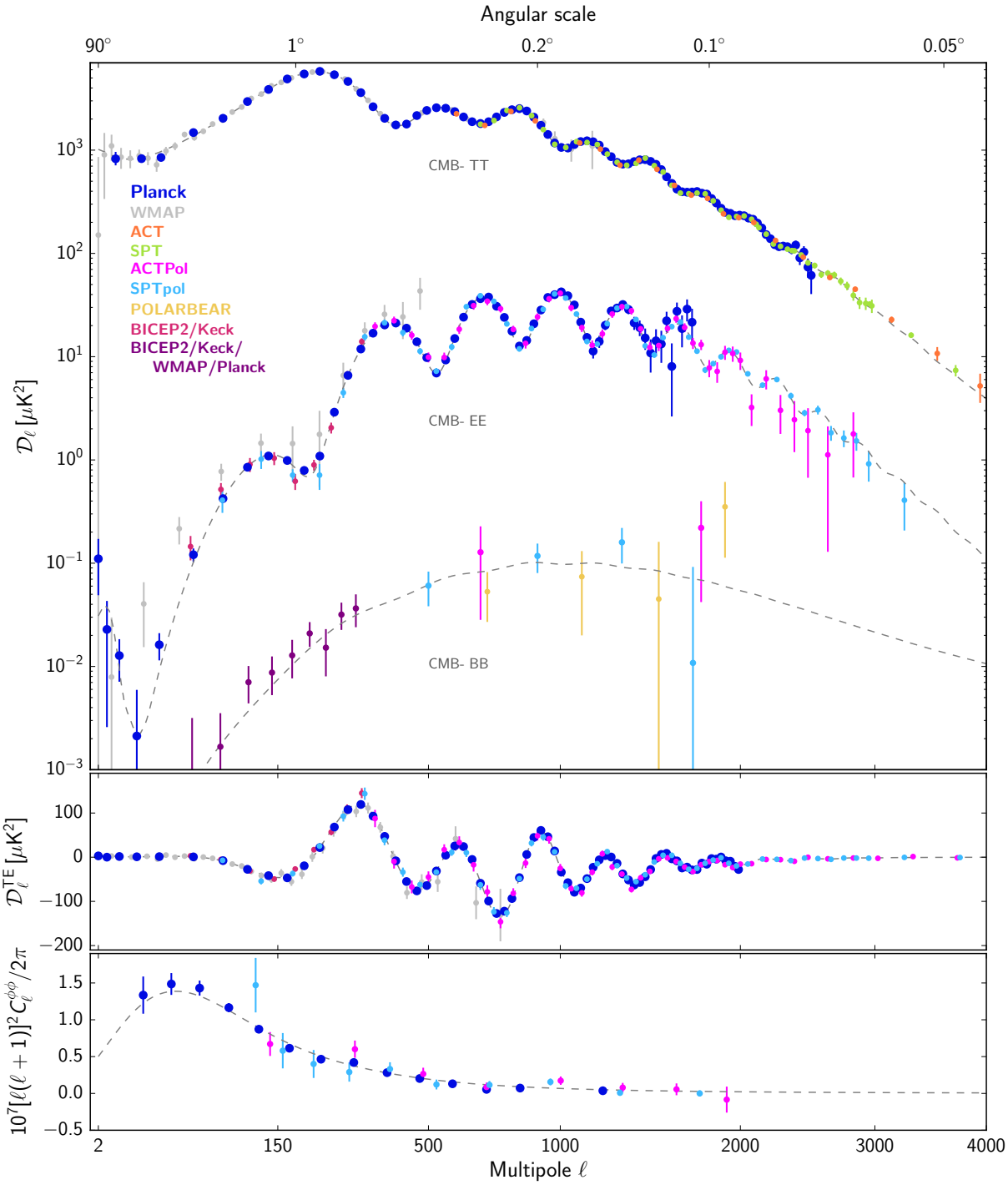

Figure 1.4. Current measurements of the various CMB anisotropies. As shown in the top panel, the E- and B-mode power spectra are many orders of magnitude smaller than the temperature anisotropies, which requires very sensitive instruments in order to measure the polarization anisotropies. Figure is courtesy of the Planck 2018 data release.

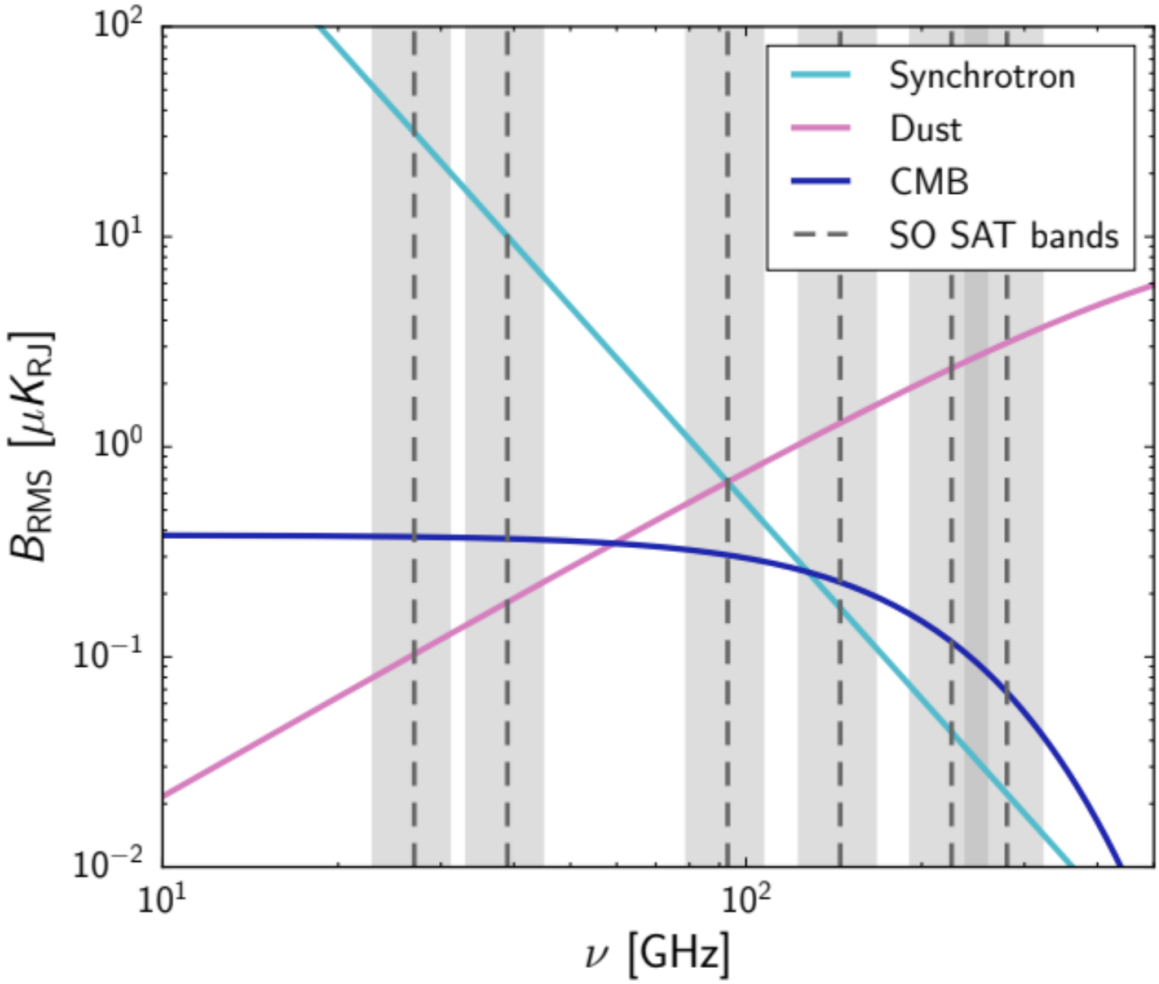

Figure 1.5. Frequency dependence of the polarized foreground signals, as compared to the CMB anisotropies. The Simons Observatory observing bands are overplotted to demonstrate the advantage of observing at many different frequencies to separate out the foreground signals from the CMB. Figure is courtesy of [16].

Chapter 2

Simons Observatory

Simons Observatory (SO) is a ground-based experiment designed to observe the polarization anisotropies in the CMB, described in section 1.2. The project was incepted in 2016 and has been in design, construction, and validation up to now. The project will see first light in the second half of 2023 and begin science-grade observations following commissioning measurements. This chapter describes the instrument design for SO, with a special focus on the Small Aperture Telescope design. We will also summarize projected sensitivities for SO's myriad science goals, as based on the instrument design.

2.1 Overview

SO will observe the CMB from the flank of Cerro Toco in the Atacama Desert of Chile. Multiple other CMB observatories are situated at the same site, including the Atacama Cosmology Telescope (ACT) [17], [18], the Simons Array (SA) [19], and the Cosmology Large Angular Scale Surveyor (CLASS) [20]. The proximity of other CMB experiments, as well as non-CMB observatories like the Dark Energy Survey (DES) [21], the Vera Rubin Observatory (formerly known as the Large Synoptic Survey Telescope, LSST) [22], and the Atacama Large Millimeter Array (ALMA) [23] allows for easier cross-correlation between surveys. In addition, the location near the equator increases the observable fraction of the sky.

The site is located 5190 meters above sea level, which demonstrates why it is an attractive

choice for SO's location. At such extreme elevation, there is not much oxygen, and combined with the desert climate, this means the surrounding atmosphere is extremely dry, with average precipitable water vapor (PWV) of $\sim$1 mm [24]. Atmospheric turbulence and contamination are one of the largest sources of low-frequency noise for SO, and being at a site with such low PWV reduces the amount of power observed by SO's instruments.

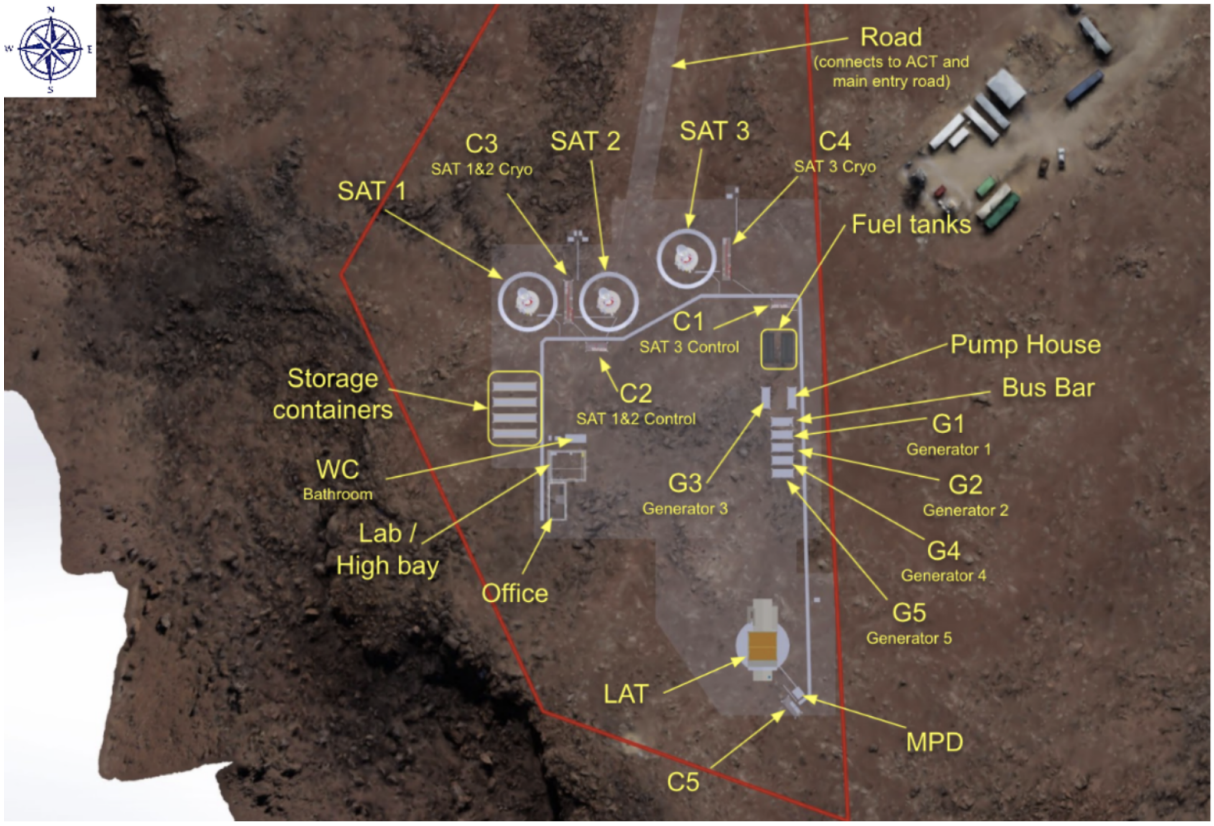

Figure 2.1. Planned layout of the SO observing site in the Atacama Desert.

Molecular absorption lines present in the atmospheric spectra provide a constraint on which frequency bands are selected for observation. As described in 1.5, it is important to observe across a variety of frequencies to mitigate the effect of galactic foregrounds. To satisfy this requirement and avoid the atmospheric lines, SO will observe in six bands. The two low-frequency (LF) bands are centered on 30 and 40 GHz, respectively; the two mid-frequency (MF) bands are centered on 95 and 150 GHz; and the two ultra-high-frequency (UHF) bands are

centered on 220 and 280 GHz[1]. See Figure 2.2 for a full depiction of the SO observing bands and the atmospheric transmission.

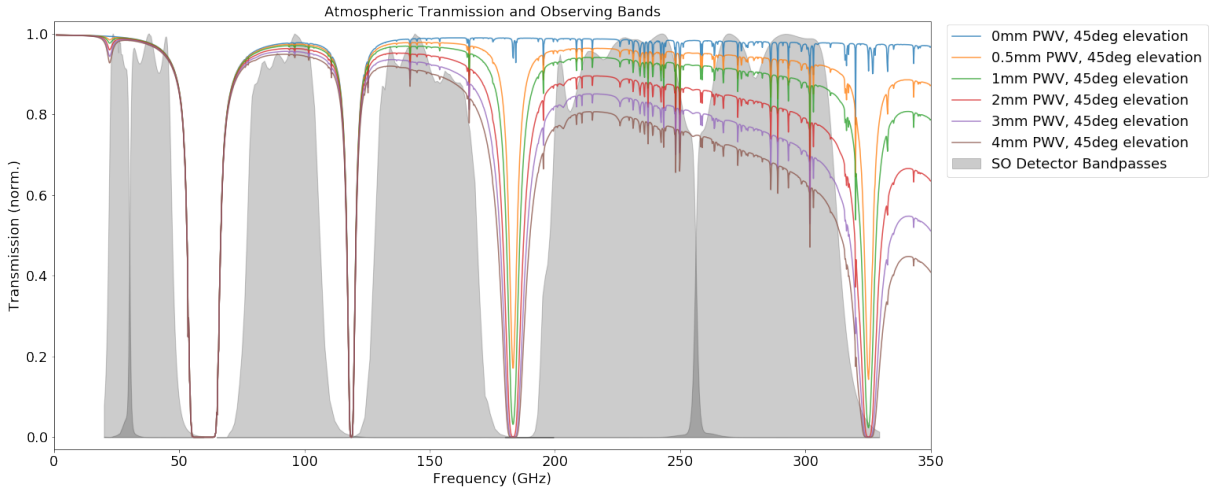

Figure 2.2. Plotted in black are the six planned observing bands for Simons Observatory. The range from 20-320 GHz provides coverage across the polarized foregrounds discussed in section 1.5. The colored lines are the atmospheric transmission profiles at different values of the precipitable water vapor (PWV). To prevent saturating the detectors with the bright atmosphere, the observing bands are chosen to take advantage of the available windows in the atmospheric transmission. The atmospheric transmission is generated from the `BoloCalc` library [25].

2.2 Observing Instruments

SO has a broad array of science goals, described in 2.3, which require sensitive measurements of the CMB temperature and polarization across a large range of angular scales. Designing one instrument that can cover all scales at the required depth is difficult, so SO is fielding two different types of instruments: small-aperture and large-aperture telescopes. Both instruments share many common pieces of hardware, leveraging experience and personnel from across the wide SO collaboration.

[1]The bands are interchangeably referred to by their center frequency or XF-1 where the X is replaced by the frequency reference. For example, the second MF band is referred to by either MF-2 or 150 GHz band.

2.2.1 Large Aperture Telescope

The SO Large Aperture Telescope (LAT) is a 6-m crossed-Dragone telescope with a 7.2° field-of-view. The LAT is coupled to the Large Aperture Telescope Receiver (LATR), a 2.5-m by 2.5-m cryogenic receiver [26], [27]. The LAT is designed to measure small angular scales, which means it focuses on the lensed B-mode spectrum and the associated science goals, while also providing the ability to de-lense the primordial B-modes targeted at large angular scales.

The LATR is designed to house 13 optics tubes (OTs), though only seven are populated in the nominal SO deployment. Each OT houses three silicon re-imaging lenses with metamaterial anti-reflection coatings. The lenses focus the incoming photons onto a focal plane that contains three hexagonal detector modules, which are described in more detail in section 2.2.2. In total, this is ∼38,000 detectors, across all six of SO's observation bands. The LAT and LATR are described in more detail in [26],[27].

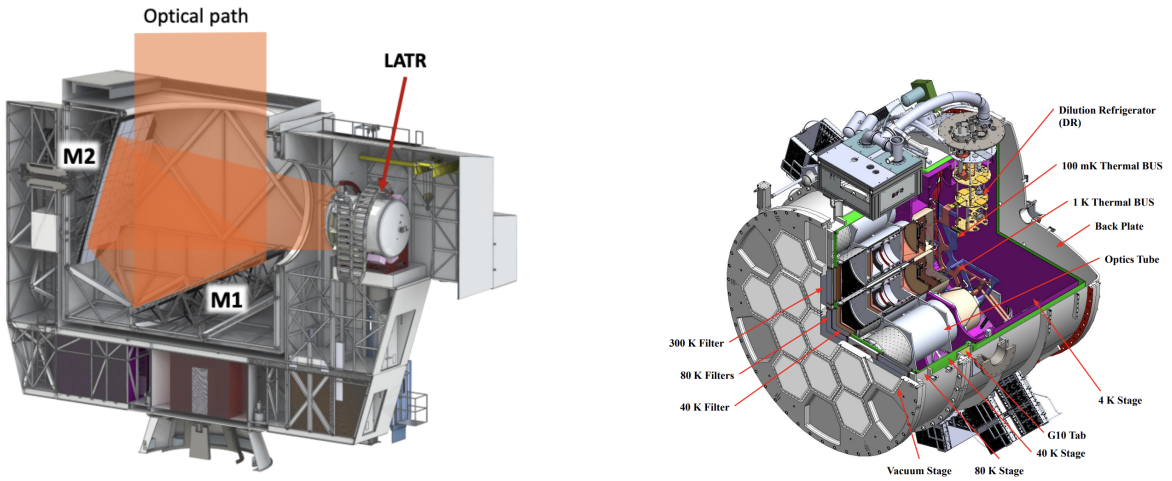

(a) Large Aperture Telescope

(b) Large Aperture Telescope Receiver

Figure 2.3. CAD renderings of the Large Aperture Telescope (left) and the Large Aperture Telescope Receiver (right). Renderings courtesy of [27], [28].

2.2.2 Small Aperture Telescopes

In addition to the LAT, SO will field three Small Aperture Telescopes (SATs) [28], [29], [30]. The SATs are designed to observe the largest angular scales on the sky, targeting a measurement of r from the primordial B-mode power spectrum. As such, angular resolution is less important than it is in the LAT.

The first SAT, henceforth referred to as SAT MF-1, or the SAT, is the first-light instrument for SO, and is being integrated and validated at UCSD before being sent to the site in Chile for science observations. More detailed descriptions of some of the validation steps are described in Chapter 5. To provide more context for those measurements, we will go into more detail about the SAT's subsystems.

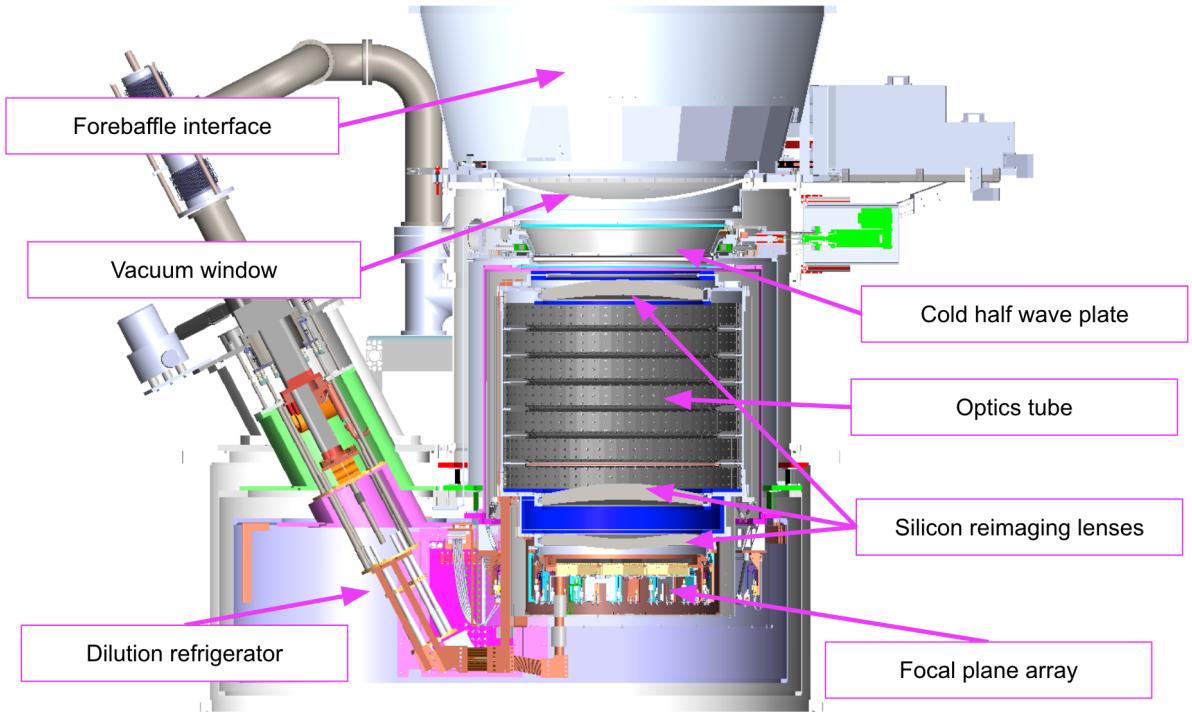

Figure 2.4. Cross-sectional view of the Small Aperture Telescope. Some key sub-assemblies are highlighted, including the dilution refrigerator that cools the milliKelvin stages, the focal plane array where the detector modules are housed, and the optics tube that contains the silicon reimaging lenses.

Optical Design

Each SAT is a 0.5-m aperture refracting telescope. The SATs have a very large FOV, $\sim$35° at 90 GHz. The beam size, and the angular resolution, is $\sim 27'$ and $\sim 18'$ at 90 and 150 GHz, respectively.

Inside each SAT is an optics tube (OT), cooled to 1 K, which consists of a 42-cm aperture stop and three re-imaging lenses. The lenses are made of silicon, with meta-material anti-reflection coatings on both interfaces [31]. The lenses focus incoming photons onto the 36-cm focal plane. The OT also contains black meta-material tiles on the walls and a series of ring baffles to minimize spurious optical features in the far sidelobes of the beams [30].

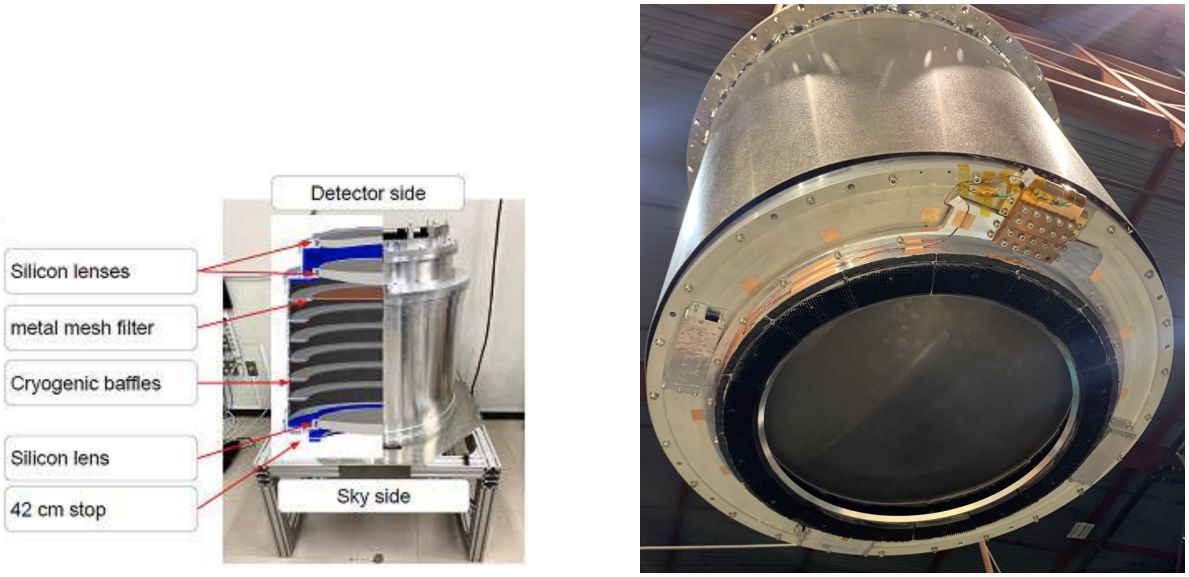

(a) Optics tube cross-section. **(b)** Photo of optics tube and sky-side lens.

Figure 2.5. Cross-sectional view of the optics tube (OT) for the SAT (left) and a photo of the OT from below during installation in the SAT. The skyward silicon lens is pictured, as well as some of the black meta-material tiles in a ring around the lens, which are used to absorb stray light.

Cryogenic Design

The detectors used for SO must be operated at 100 mK, so the SAT must be able to provide a focal plane that can achieve this temperature requirement. In service of this goal, the SAT is designed with nested mechanical shells, each at a subsequently lower temperature. The

outer shell, the nominal 300 K shell, is also responsible for maintaining a vacuum environment, necessary to maintain low operating temperatures. There are also 40 K and 4 K shells, which are named by their nominal operating temperatures. Each of these stages is supported by a truss constructed of plastic G-10 elements that provide strong mechanical support, but with poor thermal conductivity, in order to thermally isolate each subsequent stage from the previous, reducing cryogenic loading [27], [32]. These stages are cooled by a Cryomech PT420[2], a two-stage pulse tube cooler (PTC). As such, the 40 and 4 K shells are also referred to as the PTC1 and PTC2 stages, reflecting their coupling to the PTC instead of their nominal operating temperatures. These shells act primarily as radiation shields, protecting the colder temperature stages from high-temperature radiation. The 40 K shield also provides a home for the cold half-wave plate (CHWP) described in section 2.2.2. The main shells at 300, 40, and 4 K were manufactured by Criotec[3].

The 1 K and 100 mK stages house the core optical elements and the focal plane. These stages are cooled by a Bluefors[4] SD400, a dilution refrigerator which also contains a PT420 whose cooling power is used to pre-cool the helium mix in the system, but also provides some cooling power to the 40 and 4 K stages of the SAT. The 1 K stage is largely comprised of the OT, described in 2.2.2. The 100 mK stage houses the focal plane and detector modules. Both the 1 K and 100 mK stages are suspended from the preceding thermal stage by a carbon fiber truss [33], similar in purpose to the G-10 truss described earlier.

In order to reduce the optical loading from infrared radiation, a variety of IR-blocking filters are installed at different cryogenic stages. It is critical to remove as much infrared power as possible with a minimal effect on the in-band optical power. There are two main types of filters installed in the SAT: metal-mesh reflective filters fabricated at Cardiff University [34] and absorptive alumina filters with a mullite-Duroid anti-reflection coating [35]. The filter technologies are described in more detail in chapter 4.

[2]https://www.cryomech.com/products/pt420/
[3]https://www.criotec.com/en
[4]https://bluefors.com/

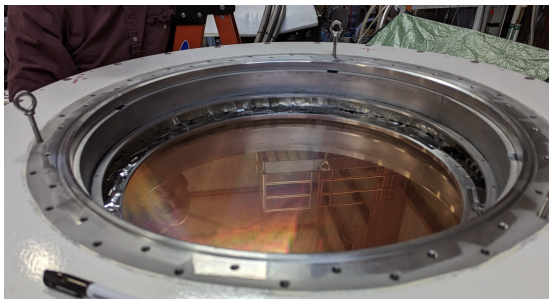

(a) Metal mesh filter from Cardiff University

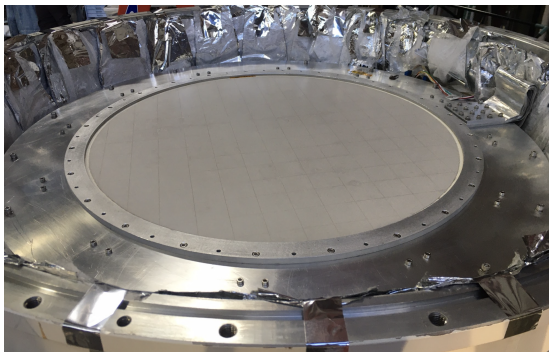

(b) Anti-reflection coated alumina filter

Figure 2.6. Two of the cryogenic filters used for removing infrared radiation. On the left is a metal-mesh reflective filter manufactured at Cardiff University, and on the right is an anti-reflection coated absorptive alumina filter, both installed at the 40 Kelvin stage.

The total estimated cryogenic loading at each stage, broken down by source, is shown in Table 2.1 [28].

Table 2.1. Estimates for the thermal load at each cryogenic stage of the SAT, broken down by source.

Stage	Available	Support	Cabling	Radiative	Optical	Total
40 K (PTC)	55 W	5.2 W	4.5 W	6.5 W	6.8 W	23 W
4 K (PTC)	2000 mW	180 mW	200 mW	4 mW	36 mW	420 mW
1 K (DR)	20 mW	1 mW	1 mW	1 mW	5 mW	8 mW
0.1 K (DR)	400 μW	3 μW	10 μW	1 μW	1 μW	15 μW

Cold Half-Wave Plate

The low-frequency variation from atmospheric turbulence is especially disruptive when trying to measure low-ℓ B-modes. In order to mitigate this effect, the SATs employ a continuously rotating cold half-wave plate (CHWP).

The CHWP is made from sapphire, which is a birefrigent material, meaning it has a refractive index that is dependent on the polarization of incident light. Anti-reflection coating is provided by a thin alumina plate with the same mullite-Duroid coating as the IR blocking alumina, though only one side is coated. Since sapphire is single-crystal alumina, the two materials have the same coefficient of thermal expansion.

A typical HWP shifts the incoming polarization from θ to $-\theta$ by tuning the thickness of the plate to be one half-wavelength. Our HWP is continuously rotating at frequency f, which has the effect of modulating the polarization of any incoming photon at $4f$. Since the SATs operate across a wide frequency range, we use a three-layer HWP to increase the modulation efficiency across the entire two-band spectral range [36], [37].

Neodymium magnets are attached to the sapphire stack, which are levitated above a yttrium barium copper oxide (YBCO) superconducting ring via the Meissner effect once the YBCO goes below its 92 K transition temperature. The levitating sapphire is then rotated by driving current in an alternating sequence through a series of solenoids placed on the stator. The rotor is typically spun at 2 Hz, which means the polarized signal is modulated at 8 Hz, above the frequency where atmospheric noise is a dominant noise source.

Detectors, Readout, and Universal Focal Plane Modules

The SAT focal plane is populated by seven universal focal plane modules (UFMs). The UFMs combine the detectors, transition-edge sensor (TES) bolometers, and the cold readout together into a hexagonal package, along with an optical coupling [38].

For LF, SO uses elliptical lenslets coupled to sinuous antennas that redirect incoming photons to the detectors. The lenslets, antennas, and detectors are all fabricated at UC Berkeley. For MF and UHF, we employ horn arrays coupled to orthomode transducers (OMTs). The horn arrays are fabricated by University of Chicago, University of Virginia, and Fermilab. The OMTs and coupled detectors are fabricated at NIST. Each optical pixel (i.e. one horn/lenslet and OMT/sinuous antenna pair) is coupled to four TES bolometers: 2 of each polarization at each of the two observing frequencies.

The cold readout multiplexer chips that contain the LC resonators and radio-frequency (RF) superconducting quantum interference devices (SQUIDs) are also manufactured and screened at NIST. The designs for the UFMs are slightly different in LF compared to MF/UHF. The UFM mechanical assemblies are made at Princeton University, and also integrated and

screened there. More details about the UFM design, construction, and screening process can be found in [38].

In the MF UFMs, which are the modules discussed in more detail in later sections, there are two pairs of coaxial transmission lines, coupled to ∼1800 detectors. The DC lines carry in two flux ramp lines, one for each coax pair. In addition, there are 12 detector bias lines, each of which bias ∼150 detectors simultaneously. The SAT MF-1 focal plane contains ∼12,600 detectors, across all seven UFMs.

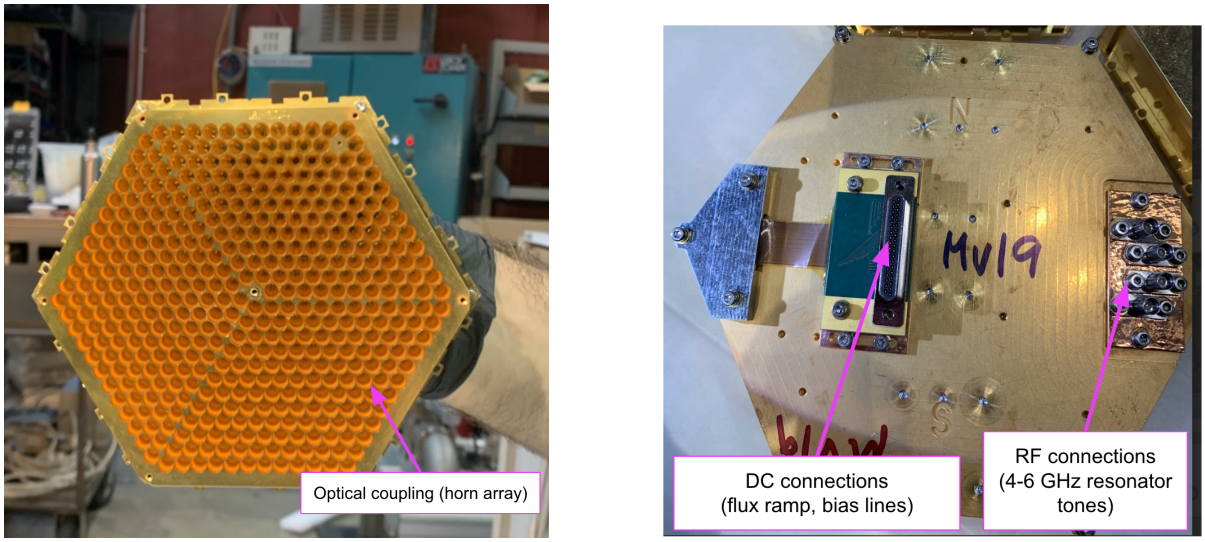

(a) UFM sky-side **(b)** UFM back-side

Figure 2.7. MF UFM package as viewed from the sky side (left) and back side (right). From the sky side, the horn array that captures incident electromagnetic radiation and couples it to the TES bolometers via OMT antennas is visible. On the back, the RF connections to connect to the transmission line and the DC connections for the detector biases and flux ramp lines are visible.

The cryogenic RF chains to carry the detector signals outside the receiver are described in [39].

Platform and Ground Shielding

Each SAT cryogenic receiver is installed on a scannable platform. The Small Aperture Telescope Platforms (SATPs) are manufactured by Vertex Antennentechnik GmbH[5]. The SATP

[5]https://www.vertexant.com/

allows for precise pointing and scanning across azimuth and elevation, as well as boresight rotation for systematics control.

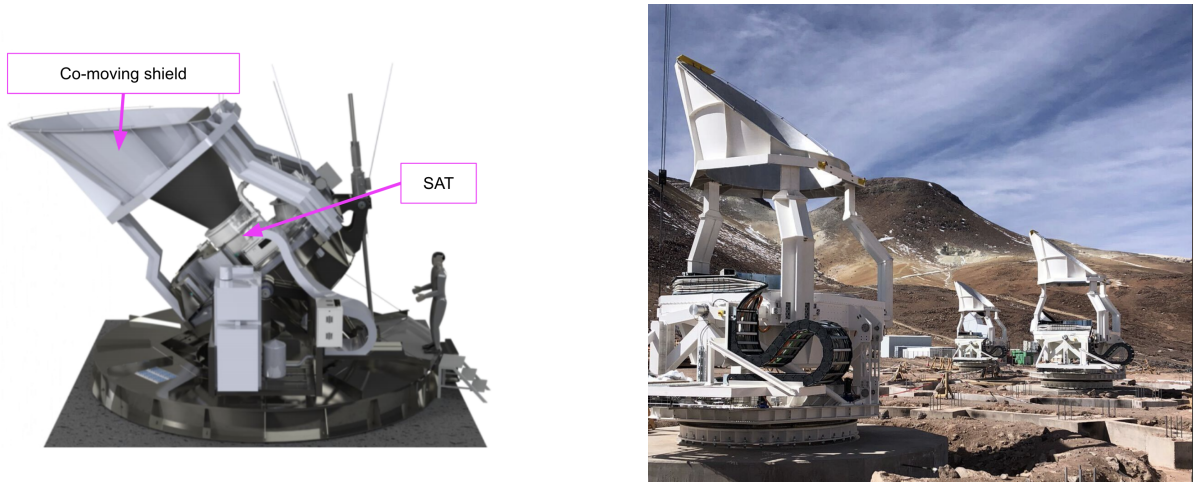

(a) Rendering of the SATP

(b) SATP installed in Chile

Figure 2.8. A CAD rendering of the Small Aperture Telescope Platform (left) and a photo of the SATPs installed at the Chilean observing site, both courtesy of Grant Teply. The first SAT will be installed into its SATP in late 2023.

Polarized pickup of ground emission is a very important systematic to mitigate and control, since it can provide unwanted polarization signal that reduces the instrument sensitivity. Three warm baffles are implemented to reduce the pickup: an absorbing forebaffle attached near the cryostat window, a reflective scoop that is co-moving with the platform, and a cylindrical ground shield coated in aluminum panels that surrounds each platform. The design philosophy of this multiple-baffle system is that any stray light from the ground is required to diffract twice off any baffle before entering the SAT aperture.

2.3 Science Goals and Projected Sensitivity

Based on the instrument design described above, the projected sensitivity for SO to the temperature and polarization anisotropies on the CMB can can be seen in Figure 2.9, as compared to other major CMB experiments, both past and future.

Detailed characterization of the CMB polarization can yield a number of compelling

science results that SO is designed to target. These include measurements of r, defined in equation 1.21, light relics in the early universe, bounds on the sum of the neutrino masses, deviations from ΛCDM, galaxy evolution and formation, measurements of the duration of reionization. Table 2.2 has summaries of SO's sensitivity to key parameters for each of these goals, from [16].

Table 2.2. Summary of SO key science goals. Numbers are reproduced from [16].

Science Goal	Parameter	Current	SO Baseline
Primordial perturbations	r	0.03	0.003
Relativistic Species	N_{eff}	0.2	0.07
Neutrino mass	Σm_ν	0.1 eV	0.04 eV
Deviations from Λ	$\sigma_8(z=1-2)$	7%	2%
	H_0 (ΛCDM)	0.5	0.4
Galaxy evolution	$\eta_{feedback}$	50-100%	3%
	p_{nt}	50-100%	8%
Reionization	Δz	1.4	0.6

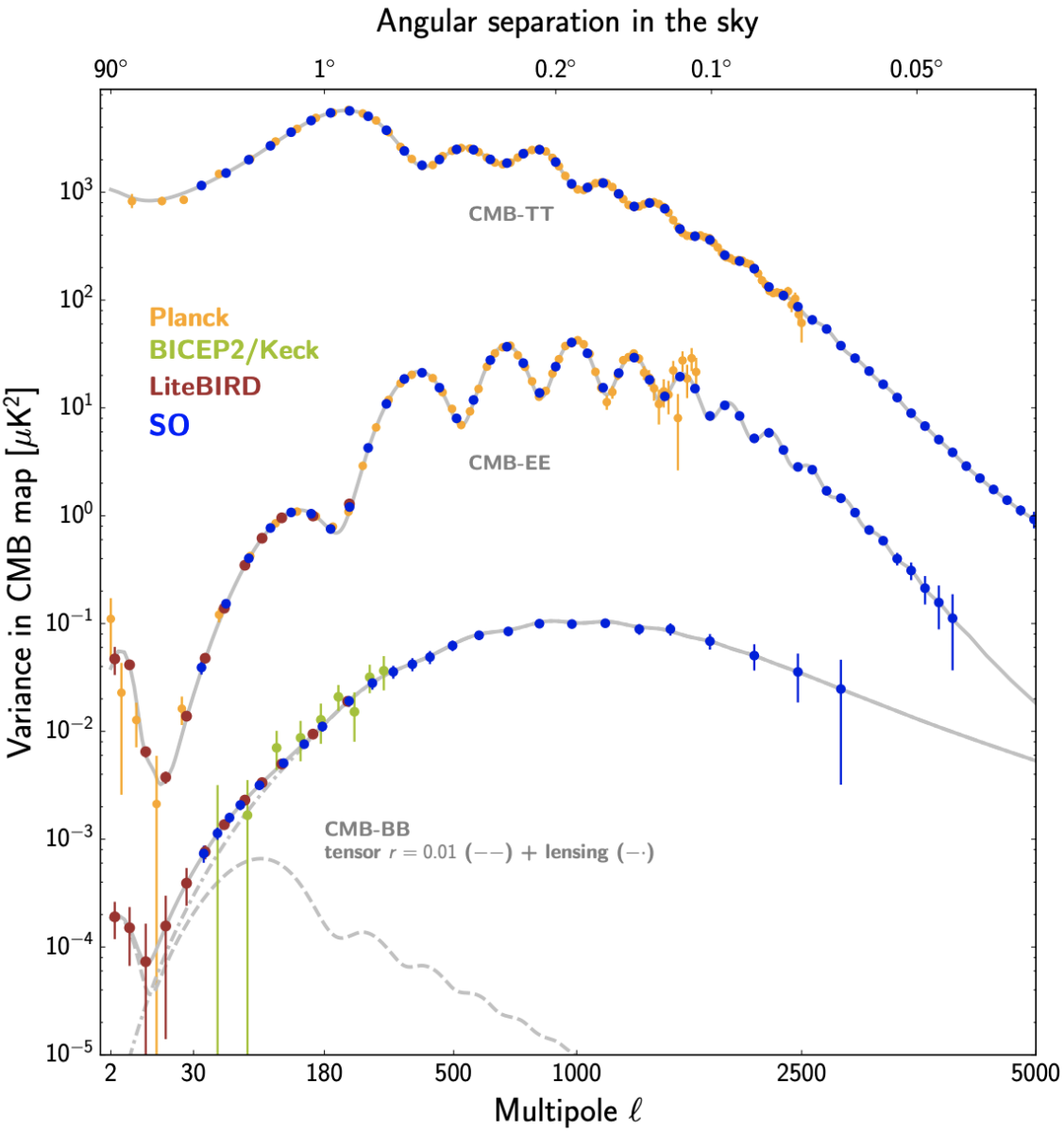

Figure 2.9. Projected angular power spectra for Simons Observatory, compared to BICEP2/KECK, Planck, and future satellite mission LiteBIRD [40].

Chapter 3

Detector and Readout Technology

This chapter describes the detector and readout technology employed by SO. The description of the bolometer detectors focuses on a derivation of key parameters for understanding the detector sensitivity, as well as a description of common measurement techniques used in detector characterization, to prepare for a description of their implementation in chapter 6.

3.1 Transition Edge Sensor Bolometers

3.1.1 Fundamental Bolometer Operation

For mm-wave astronomy, the wavelength range SO operates in, the most sensitive choice for detector technology is the transition-edge sensor (TES) bolometer. Generally speaking, a bolometer is a device used to measure the thermal energy of incoming electromagnetic radiation.

In the simplest implementation, a bolometer consists of an absorptive island at temperature T with heat capacity C coupled to a thermal reservoir at temperature T_{bath} via a weak link with thermal conductance G. A basic schematic of the thermal setup for a bolometer can be seen in Figure 3.1. Following [41], the differential equation governing the temperature of the bolometer is

$$C\frac{dT}{dt} = -P_{bath} + P_J + P_{opt} \tag{3.1}$$

where P_{bath} is the power flowing from the island to the reservoir and P_{opt} is the incident

power on the island. The inclusion of the Joule power term P_J is foreshadowing for the case where the bolometer island is a thermistor with a current running through it, which we will return to shortly.

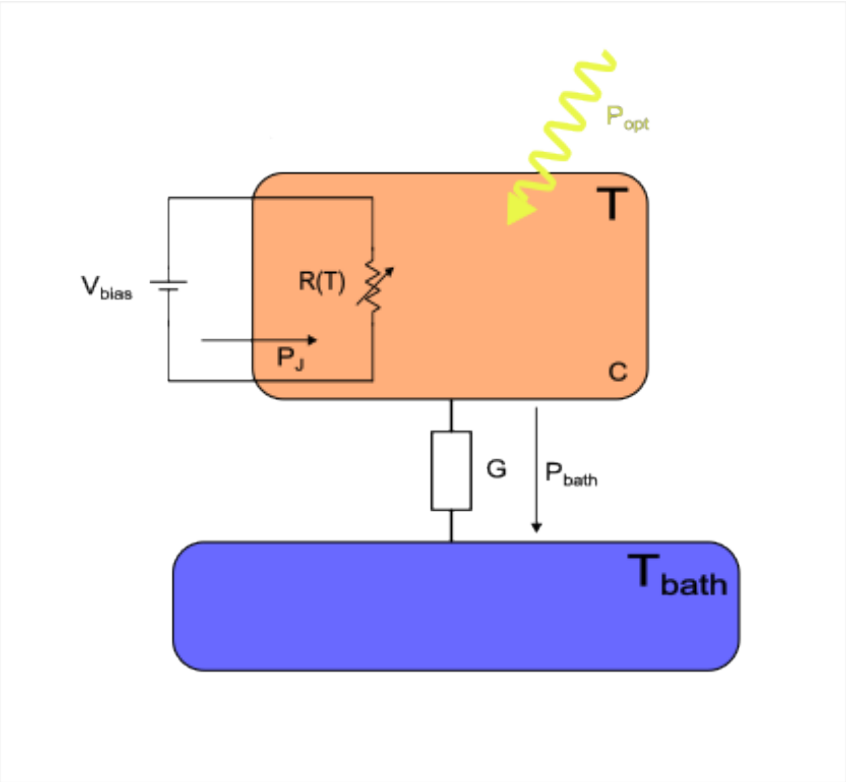

Figure 3.1. Schematic of a TES bolometer. The orange island increases in temperature due to power from incident photons P_{opt} and Joule heating P_J from applied bias voltage on the TES, which is represented by the variable resistor. The island is connected via a weak thermal link with conductance G to a reservoir at temperature T_{bath}.

Where the thermal conductivity between the bolometer and the bath is created by a material with a $T^{(n-1)}$ dependence in its thermal conductance, the power conducted to the bath can be expressed by a power law [41]:

$$P_{bath} = \kappa(T^n - T_{bath}^n) \tag{3.2}$$

where $\kappa = G/n(T^{n-1})$, and $G \equiv dP_{bath}/dT$. The exponent n is a number typically between 1 and 4, depending on the type of thermal carriers that flow along the link between the island and

the bath.

In the case of TES bolometers, the absorbing element is a thin superconducting film. The material of the film is chosen such that there is a steep transition from the normal regime to the superconducting regime, i.e. from the film having a normal resistance R_n to zero resistance, which occurs at the critical temperature T_c. For SO, these films are made from aluminum manganese (AlMn) and typically have transition temperatures $T_c \sim 160mK$ and normal resistances $R_n \sim 8m\Omega$. A superconductor is a natural choice, since sensitivity requirements necessitate operation at cryogenic temperatures. This is explored further in 3.2.

We tune the value of G for the bolometer such that in the equilibrium state,

$$P_{bath} = P_{bias} + P_{opt} = \kappa(T^n - T_{bath}^n), \tag{3.3}$$

which states that the power flowing from the TES to the bath is equal to the power deposited on the TES from a combination of the Joule heating due to the applied voltage bias and any incident optical radiation. If too much optical power or bias power is applied, the temperature of the island will increase above the critical temperature T_c and the TES will be saturated, since the resistance will no longer change as a function of temperature.

The effect of choosing a superconducting film with a sharp transition for the absorbing element of the bolometer is that a small change in temperature, caused by incident photons, is observable as a large change in electrical resistance, which can be read out as a change in current through the TES film. A schematic of the electrical circuit is shown in Figure 3.2. The differential equation governing the current flow in the TES is given by Kirchhoff's law:

$$L\frac{dI}{dt} = V - IR_L - IR(T,I) \tag{3.4}$$

where L is the inductance, V is the bias voltage applied to the TES, $R_L = R_{sh} + R_{parasitic}$ is the load resistor used to apply the bias, and $R(T,I)$ is the variable resistance of the TES itself.

The decision to voltage bias the TES—$R_{sh} \ll R_{par} + R_{TES}$—is made to stabilize operation

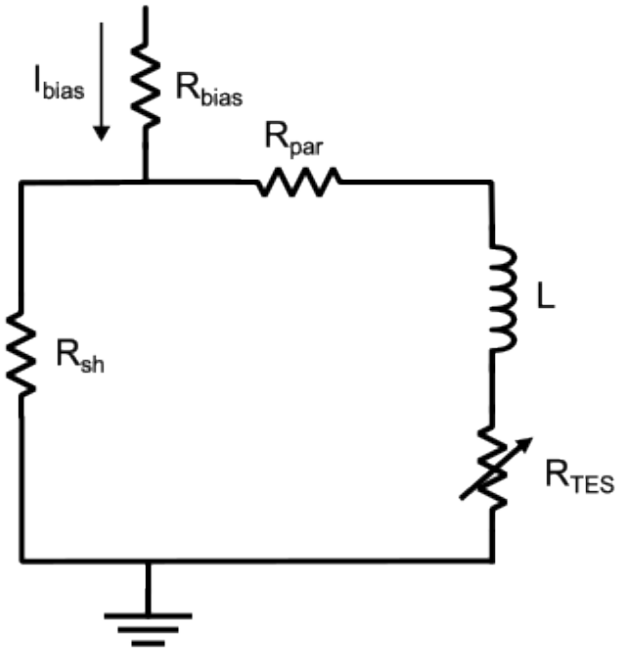

Figure 3.2. Electrical schematic of a TES bolometer operational circuit. The current flowing through the TES will vary as the temperature changes in response to incident optical power. R_{par} accounts for any parasitic resistance in the TES circuit, in which case $R_L = R_{sh} + R_{par}$.

of the TES as power is absorbed by the island due to incident photons [41]. Recall that the Joule power due to the bias is $P_{bias} = P_J = \frac{V_{bias}^2}{R_{bolo}}$. When a photon is absorbed by the bolometer, the temperature increases, which corresponds to an increase in the resistance of the TES. The increase in resistance leads to a decrease in Joule power, which leads to a decrease in temperature and the bolometer recovers to its original state before the incident optical power. In other words, due to the applied voltage bias, the system undergoes negative electrothermal feedback, where the dissipated Joule power naturally reduces to compensate for the increase in optical power, maintaining a stable state where the TES can remain biased in the linear range of the superconducting transition.

3.1.2 Detector Time Constants

It is convenient to define the logarithmic derivatives

$$\alpha = \left.\frac{\partial \log R}{\partial \log T}\right|_{I_0} = \left.\frac{T_0}{R_0}\frac{\partial R}{\partial T}\right|_{I_0}, \tag{3.5}$$

$$\beta = \left.\frac{\partial \log R}{\partial \log I}\right|_{T_0} = \left.\frac{I_0}{R_0}\frac{\partial R}{\partial I}\right|_{T_0} \tag{3.6}$$

to describe the change in the bolometer resistance relative to the change in TES temperature or current.

In the small signal limit—considering small changes in current, resistance, and temperature when the TES is biased in the linear regime of its transition—equations 3.1 and 3.4 simplify to

$$C\frac{d\delta T}{dt} = -(1-\mathscr{L})G\delta T + (2+\beta)I_0R_0\delta I + \delta P_{opt} \tag{3.7}$$

$$L\frac{d\delta I}{dt} = \delta V - (R_L + R_0(1+\beta))\delta I - \frac{\mathscr{L}G}{I_0}\delta T \tag{3.8}$$

where we have defined the electrothermal loop gain

$$\mathscr{L} = \frac{P_{bias}\alpha}{GT} \tag{3.9}$$

which we will return to later.

For the case of the voltage-biased TES, $\delta V = 0$, $\delta I \neq 0$, and $R_0 \gg R_L$. In addition, we typically choose a substantially small inductance L to reduce the electrical time constant $\tau_{el} = L/(R_0(1+\beta)+R_L)$. Evaluated in the Fourier domain, the differential equations 3.7 and 3.8 simplify to

$$\delta P = G_{eff}\left(1 + i\omega\tau_{eff}\right)\delta T, \tag{3.10}$$

where we have defined an effective thermal conductance and effective time constant:

$$G_{eff} = G(1 + \frac{\mathscr{L}}{1+\beta}) \tag{3.11}$$

$$\tau_{eff} = \frac{\tau_0}{1 + \frac{\mathscr{L}}{1+\beta}}, \tag{3.12}$$

where $\tau_0 \equiv C/G$ is the natural thermal time constant of the bolometer.

The time constant is a critical detector parameter that affects the sensitivity of the entire instrument. The time constant sets the bandwidth of the detector, effectively describing how quickly an individual detector can respond to incident signal—the smaller the time constant, the faster the response, or equivalently, the higher the bandwidth of the detector to signal. This underscores the importance of negative electrothermal feedback: the higher the loop gain—the more feedback—the faster the time constant.

In practice, SO sets requirements on its detector time constants, requiring particular detector bandwidths to prevent aliasing of the measured detector signal during telescope scanning (in the case of the LAT) and HWP modulation (in the case of the SAT). Techniques to measure the detector time constants—also required for deconvolving the effect of the finite time constant from the measured signal for reconstruction of the true sky signal—are described in section 3.3.

3.1.3 Detector Responsivity

From a measurement perspective, it is crucial to understand how much the TES current is changing as optical power is incident on the bolometer. That leads us to define the bolometer responsivity:

$$S_I \equiv \frac{\delta I}{\delta P_{opt}}. \tag{3.13}$$

From the coupled system of differential equations in equations 3.7 and 3.8, we can solve for the responsivity as a function of bolometer resistance, loop gain, and bias voltage, from [41]:

$$S_I(\omega) = -\frac{1}{V_{bias}}\left[\frac{L}{\tau_{el}\mathscr{L}R_0} + (1 - \frac{R_L}{R_0} + \frac{i\omega L}{\mathscr{L}R_0}\left(\frac{1-\mathscr{L}}{\tau_0} + \frac{1}{\tau_{el}}\right) - \frac{\omega^2 L\tau_0}{\mathscr{L}R_0}\right]^{-1} \tag{3.14}$$

For a stiff voltage bias, $R_L, i\omega L \ll R_0$, which simplifies the expression for responsivity:

$$S_I(\omega) = -\frac{1}{V_{bias}}\frac{\mathscr{L}}{\mathscr{L}+1+\beta}\frac{1}{1+i\omega\tau_{eff}}. \tag{3.15}$$

Under strong electrothermal feedback ($\mathscr{L} \gg 1+\beta$) and sufficiently low frequency such that the roll-off due to the time constant is inconsequential, the bolometer responsivity can be estimated by

$$S_I = -\frac{1}{V_{bias}}. \tag{3.16}$$

This is a simple but powerful statement that demonstrates another key benefit of electrothermal feedback. At sufficiently high loop gain, a TES bolometer's response to incoming optical power is only a function of the applied voltage bias, not any of its individual characteristics. This means that any TES bolometers with a shared bias voltage will act as a uniform array in response to incident optical power. We will discuss methods to estimate the bolometer responsivity in section 3.3.

The responsivity is also important in maximizing bolometer sensitivity. We will return to this idea in section 3.2.

3.2 Bolometer Noise Properties

TES bolometers are an attractive choice for measurements of the mm-wave CMB photons because they can be so low in noise that the detector noise itself becomes subdominant to other fundamental noise sources. To quantify the noise of the detector, it is best to use the so-called noise-equivalent power (NEP), which is the power that a signal with 1 Hz of bandwidth would

need to have to be equal to the noise in the power spectrum of a given timestream. This can be related to the total variance in power by

$$\sigma^2 = \int |NEP|^2 df. \tag{3.17}$$

The detector NEP can be described by a quadrature sum over all the contributing noise terms:

$$NEP_{det} = \sqrt{NEP_{\gamma}^2 + NEP_{Johnson}^2 + NEP_g^2 + NEP_{readout}^2} \tag{3.18}$$

where NEP_{γ} is the photon noise, $NEP_{Johnson}$ is the Johnson-Nyquist noise, NEP_g is the thermal carrier noise, and $NEP_{readout}$ is the contribution from the readout technology for the detectors, referred back to the detector as a power.

Readout noise is typically quoted as a noise equivalent current ($NEI_{readout}$), referred to a Superconducting Quantum Interference Device (SQUID) coupled to the TES. To convert this to the same NEP used for the other bolometric noise terms, we can use the responsivity S_I from equation 3.13:

$$NEP_{readout} = \frac{1}{|S_I|} NEI_{readout}. \tag{3.19}$$

If the bolometer responsivity is sufficiently large, this noise term is suppressed. If the responsivity is too low, the readout noise can begin to dominate the overall noise of the bolometer.

Johnson-Nyquist noise is generated by thermal fluctuation of the charge carriers flowing through the bolometer and is intrinsic to any electronic system. The NEI for a bolometer at temperature T_c and resistance R is reduced by the loop gain [41] and given by

$$NEI_{Johnson} = \frac{1}{\mathscr{L}} \sqrt{\frac{4k_B T_c}{R}}. \tag{3.20}$$

Using the responsivity from equation 3.13, we can convert this to a noise equivalent

power:

$$NEP_{Johnson} = \frac{\mathscr{L}+1}{\mathscr{L}^2}\sqrt{4k_bT_cP_{bias}}. \tag{3.21}$$

At sufficiently high loop gain, the Johnson-Nyquist noise becomes neglibible.

The thermal carrier noise is related to energy fluctuations of the particles that traverse the thermal link between the bolometer island and the bath it is weakly coupled to. These fluctuations are present in any macroscopic system, and in the bolometric case they result in power fluctuations. The noise equivalent power is given by

$$NEP_g = \sqrt{\gamma 4k_BT_b^2G} \tag{3.22}$$

where γ parametrizes the temperature dependence of the thermal conductivity of the link. Using the definitions of G and γ from [42], equation 3.22 simplifies to

$$NEP_g = \sqrt{4k_BP_{bath}T_{bath}F_{link}} \tag{3.23}$$

For SO, $F_{link} \sim 2.5$. The most important takeaway here is that the thermal carrier noise scales as the square root of the bath temperature and the operating power of the bolometer, which highlights the importance of operating any bolometer, TES or not, at low temperatures to reduce the noise penalty, as alluded to earlier in this section. It also provides motivation for having the minimum saturation power allowable on the bolometer while the bolometer still has sufficient dynamic range for our signal.

Finally, for any radiative source at temperature T, the occupation number is defined as

$$n \equiv \frac{1}{e^{h\nu/k_BT}-1}. \tag{3.24}$$

The observed power detected is thus

$$P_\gamma = \int \eta(\nu) h\nu n d\nu \tag{3.25}$$

where $\eta(\nu)$ is the efficiency of the collected optical elements and the detector. After observing for a time τ, the total variance in the measured optical power is [43]

$$\sigma^2 = \frac{1}{\tau}\int (h\nu)^2 \eta n(1+\eta n) d\nu. \tag{3.26}$$

In many systems, it is suitable to consider just one of these terms. When n is small, the so-called optical limit, just the first term contributes. In this limit, the arrival times of the photons vary according to Poisson statistics, and uncertainty in the power scales with the square root of the power of the signal. In the radio limit, when occupation number is large, the power uncertainty scales linearly with power. We can express the NEP by using equation 3.17:

$$NEP_\gamma = \sqrt{2\int (h\nu)^2 \eta n(1+\eta n) d\nu}. \tag{3.27}$$

It is convenient to use the approximation that the efficiency is sharply peaked at ν_0 with some integrated bandwidth $\Delta\nu$, which simplifies the NEP to

$$NEP_\gamma \approx \sqrt{2}\sqrt{h\nu_0 P_\gamma + \frac{P_\gamma^2}{\Delta\nu}}. \tag{3.28}$$

It is often convenient to refer the bolometer noise to the CMB itself, which leads to the so-called noise equivalent temperature (NET). This is the fluctuation of the CMB that would yield a signal-to-noise ratio of 1 after 1 second of integration time. This is related to NEP by

$$NET = \frac{NEP}{\sqrt{2}\frac{dP}{dT_{CMB}}} \tag{3.29}$$

where

$\frac{dP}{dT_{CMB}}$ is related to the optical efficiency $\eta(\nu)$, as it relates the change in power on the

bolometer relative to the differential change in the CMB temperature. The factor of $\sqrt{2}$ arises because the definition of NEP is related to the signal bandwidth in Hz, while the definition of NET is related to the signal integration time in seconds.

So far, we have discussed the noise properties of a single detector. When we consider an array of N detectors with yield Y, the NET scales as

$$NET_{arr} = \frac{NET_{det}}{\sqrt{YN}}\Gamma \tag{3.30}$$

where *Gamma* parameterizes how correlated the noise is between different detectors. For modern TES bolometers, like those used in SO, it is possible to reduce the contributions from readout, Johnson-Nyquist, and thermal carrier noise such that the dominant noise term is the photon noise. This is the oft-referred to "photon-noise-limited" detector. In this case, it is necessary to increase the number of detectors observing the sky. This is what drives CMB experiments to use increasingly large focal planes with as many detectors deployed as possible.

3.3 Detector Characterization Methods

Characterizing detector performance requires measurement techniques designed to extract specific parameters such as τ_{eff}, R_{TES}, P_{sat}, S_I, among others. Below, we will go over three such measurements—IV curves, bias steps, and bias group maps—all of which are necessary to fully characterize a detector array for SO. Software implementation of each of these measurement techniques for SO is discussed in section chapter 6. Development and testing of this software was an important function of the optical test bed and of all the SAT testing reported in this thesis.

3.3.1 IV Curves

Electronic devices are often characterized by IV curves, and TES bolometers are no exception. Functionally, at a fixed bath temperature, the TES bolometer operates as a variable resistor whose resistance changes as a function of the applied voltage bias. Understanding the

resistance as a function of bias is a crucial step in characterizing any TES. Not only does it give a sense of whether or not the detector is operating as expected, but it can be used to help estimate parameters like the appropriate bias voltage to choose for maximal sensitivity in an observation.

The general order of operations goes as follows: drive enough current through the TES such that you exceed the superconductor's critical current I_c and send the TES normal. Then, reduce the bias voltage ($V_{bias} = I_{bias}R_{bias}$) through the TES in steps, recording the current through the TES (I_{TES}) at each step.

A well-behaved TES has three distinct operational ranges: overbiased, in-transition, and superconducting. The ranges are typically classified by the value of R_{TES} relative to the normal resistance R_n, defined as R_{frac}:

$$R_{frac} \equiv \frac{R_{TES}}{R_n}. \tag{3.31}$$

When the TES is normal, $R_{frac} = 1$, with the island being held above the transition temperature T_c by Joule heating. This is the overbiased region. As the voltage bias is decreased, the total bias power decreases in turn, and the temperature of the island will decrease. As it drops near T_c, R_{TES}, and thus R_{frac}, will decrease. Since the resistance decreases, I_{TES} will begin to increase. This region, when $0 < R_{frac} < 1$, is the in-transition regime. It is in this area that the loop gain increases, and the TES starts to experience negative electrothermal feedback. Eventually, the resistance of the TES will decrease to 0, when it becomes superconducting. At this point, $R_{frac} = 0$. Now, the TES acts as a superconducting short, so $I_{TES} = I_{bias}$.

This immediately suggests one of the uses of an IV curve: if the TES is absorbing too much optical power such that the power balance in equation 3.3 leads to a TES temperature constantly above T_c, regardless of P_bias, the TES will never go through its transition. The resultant IV curve will look just like an Ohmic resistor with resistance R_n, over the full range of applied biases.

Beyond verifying general behavior of the TES, the IV curve is useful for extracting

parameters from each detector. Knowing R_{sh}, R_{bias}, and I_{bias}, and given the measured I_{TES}, we can extract R_{TES}, V_{TES}, and P_{TES}. Referencing the schematic in Figure 3.3, the TES parameters can be calculated as:

$$R_{TES} = R_{sh}\left(\frac{I_{bias}}{I_{TES}} - 1\right) \tag{3.32}$$

$$V_{TES} = I_{TES}R_{TES} = R_{sh}\left(I_{bias} - I_{TES}\right) \tag{3.33}$$

$$P_{TES} = \frac{V_{TES}^2}{R_{TES}}. \tag{3.34}$$

One of the most important relationships that is generated by the IV curves is R_{frac} vs. V_{bias}. Using IV curves, we can estimate the optimal bias point for a given detector.

The saturation power is defined from equation 3.2 as the total power on the TES when the TES is at temperature T_c:

$$P_{sat} \equiv P_{TES}(T_c) = \kappa(T_c^n - T_b^n). \tag{3.35}$$

Since we don't directly measure the temperature of the TES itself, merely the change in current due to its change in temperature, it can be difficult to define this point consistently. Many different conventions exist, but the one used by SO is to report the saturation power as the power on the TES at $R_{frac} = 0.9$ in the absence of optical power, as measured by the IV curve. Here, it becomes important to note that the TES power reported in equation 3.34 is just the electrical power on the TES: it does not account for the optical power. When $P_{opt} \neq 0$, some of the total power on the TES is the incident light absorbed by the bolometer, so the so-called P_{sat} measured at $R_{frac} = 0.9$ is reduced by P_{opt}. While this is a convenient way to get an estimate of the optical power on the TES for a particular moment in time, it is not an accurate measure of the saturation power. Refer to Chapter 6 for an example IV curve.

3.3.2 Bias Steps

Another operation that can be performed to extract detector parameters is bias steps. This is performed by playing a small square-wave (typically of amplitude 0.1 pW at $R_{frac} = 0.5$) on top of the DC bias value and measuring the TES response. When the TES is in-transition, the amplitude of the TES response can be used to estimate P_{bias}, R_{TES}, and S_I. The bolometer time constant τ_{eff} from equation 3.12 can also be fit from the relaxation time at each step.

Given a known baseline I_{bias}, a change in bias ΔI_{bias} i.e. the height of the commanded bias step, and the measured height of the TES response ΔI_{TES}, we can extract all the TES parameters. First, using the schematic in Figure 3.3:

$$I_{bias} - I_{TES} = I_{sh} = \frac{V_{sh}}{R_{sh}} = \frac{V_{TES}}{R_{sh}} = \frac{P_{bias}}{I_{TES} R_{sh}}. \tag{3.36}$$

Rearranging and separating out I_{TES} gives

$$I_{TES} = \frac{1}{2}\left(I_{bias} \pm \sqrt{I_{bias}^2 - 4\frac{P_{bias}}{R_{sh}}}\right). \tag{3.37}$$

Defining the derivative of the TES current with respect to the bias current, i.e. the ratio of the change in the TES current relative to the change in the bias current:

$$\Delta I_{rat} \equiv \frac{\Delta I_{TES}}{\Delta I_{bias}} \approx \frac{1}{2}\left(1 - \frac{I_{bias}}{\sqrt{I_{bias}^2 - 4\frac{P_{bias}}{R_{sh}}}}\right). \tag{3.38}$$

Rearranging and solving for I_{TES} using equation 3.36,

$$I_{TES} = \frac{I_{bias}\Delta I_{rat}}{2\Delta I_{rat} - 1} \tag{3.39}$$

which expresses I_{TES} purely in terms of known quantities. The rest of the TES parameters follow from the standard definitions:

$$P_{bias} = R_{sh}(I_{bias}I_{TES} - I_{TES}^2), \tag{3.40}$$

$$R_{TES} = \frac{I_{TES}^2}{P_{bias}}, \tag{3.41}$$

$$S_I = \frac{1}{R_{sh}(I_{bias} - 2I_{TES})}. \tag{3.42}$$

Recall that equation 3.39 is only valid when in the transition when $\mathscr{L} \gg 1$, where $\Delta P_{bias} \approx 0$ due to negative electrothermal feedback. If this was not the case, the approximation in equation 3.38 would no longer be valid.

Bias steps provide a less obtrusive way to probe the TES parameters in-transition. IV curves take longer to acquire and change the thermal state of the TES more substantially, which can add uncertainty about what the parameters are in the operating state. In addition, they are fairly time-consuming. Bias steps are fast and can provide an independent check that the detectors are correctly biased in the transition by estimating the value of R_{TES} in-transition. In addition, the extracted time constants can be used to give an estimate for how deep in the transition the detectors are biased. Finally, the estimated responsivity from the bias steps is crucial for the first steps in analysis pipelines, which require a way to convert between the current units directly measured and the desired units, which is the power of the incoming CMB photons. Refer to Chapter 6 for bias steps.

The other advantage of bias steps is the ability to quickly provide mappings of detector to bias group, which is discussed in more detail in section 3.3.3.

3.3.3 Bias Group Maps

In section 2.2.2, we described how each UFM has 12 bias lines, interchangeably referred to as bias groups, each of which is responsible for providing the voltage biases for ~ 150

detectors. In the ideal world, there would be only one detector on a given bias line, which allows us to precisely select the optimal value to bias the detector at the most sensitive point in the transition (typically $R_{frac} = 0.5$). However, because many detectors share a common bias group, we must choose a bias value that maximizes the number of channels at the optimal point in-transition.

However, a required input for such a calculation is identifying which detectors are coupled to which bias groups. Given the nature of the μmux readout, identifying which physical detectors are coupled to which resonator channels in the readout system is a non-trivial problem, which is addressed by the `DetMap`[1] software. For a particular test or observation, it is therefore critical to be able to identify which detector channels in resonator space are coupled to which bias groups in a fast and repeatable manner.

This is accomplished by performing bias steps on one bias line at a time and identifying which detector channels show a response to the square-wave bias-step input. These so-called bias group maps are best collected when the detectors are in the superconducting state, so that the amplitude of the measured step equal to that of the commanded step (i.e. $\Delta I_{rat} = 1$). These bias group maps can then be stored and accessed for a particular observation, to identify and isolate certain bias groups in various analyses, or apply specific calibrations, as well as allow us to provide estimated parameter values from IV curve calibrations on a per-detector basis, despite the fact that the bias group applies the same bias to many detectors simultaneously (each with different detector parameters). This is especially important in terms of providing accurate estimates of the detector responsivity, which is inversely proportional to applied voltage bias.

3.4 Microwave Multiplexing Readout

In order to measure the increasingly large number of cryogenic detectors, it becomes necessary to implement a multiplexed readout scheme. The two main reasons driving us towards multiplexed readout are both related to the density of wires required to measure each detector.

[1] https://github.com/simonsobs/detmap

In each MF SAT, for example, there are $\sim$ 13,000 detectors, each of which requires a pair of wires to bias and readout the TES signal. This not only creates mechanical concerns—designing a cryostat that can support that density of wires would become increasingly large—but also cryogenic concerns. The increased thermal load in the cryostat from so many wires would create problems maintaining the operating temperatures necessary to maintain low-noise operation of the detectors.

SO uses a type of frequency-division multiplexing known as microwave multiplexing, or μmux for short. In μmux, each detector is inductively coupled to a quarter-wave LC resonator via an RF SQUID [44]. As the current through the TES changes in response to a change in power, the changing flux in the RF SQUID changes the effective inductance of the coupled resonator, which shifts its resonance frequency. The resonators are connected to a common transmission line, which sends in probe tones at the resonance frequencies, and measures the change in resonance frequency. This change is directly proportional to the TES signal, so we are able to record the signals of all detectors connected to a single transmission line. For SO, we are able to couple roughly 1,000 resonators to the transmission line between 4-6 GHz, which gives us a multiplexing-factor (mux-factor) of 1000 [45]. A schematic of the full system can be seen in Figure 3.4.

In order to prevent low-frequency noise, a common flux ramp bias is applied to all the RF SQUIDs. The sawtooth pattern is intended to modulate the resonance frequency of each resonator even in the absence of TES signal. The ramp has a reset rate of 4 kHz and the amplitude of the ramp is chosen such that an integer number of flux quanta are driven through the SQUID in each ramp period. Typically, the number of flux quanta is chosen to be 5, which sets the final modulation rate for each resonator at 20 kHz [46]. The TES signal is then extracted as a phase shift in the flux-ramp-modulated resonator frequency shift. A representation of this effect can be seen in Figure 3.5.

In order to control the readout at room temperature, we use the so-called SLAC Microresonator RF (SMuRF) electronics, provided by collaborators at Stanford. The SMuRF system

provides both the RF tones used to interrogate the resonators along the coaxial transmission lines, as well as the DC signals such as the flux-ramp signal and detector biases. More details about μmux and SMuRF can be found in [46].

SO is the first deployment of μmux on cameras with $>$10,000 detectors. The ability to perform all the tests described in this chapter, along with other characterization measurements, requires new control and analysis capabilities that were developed and tested during the testing described in Chapters 5 and 6.

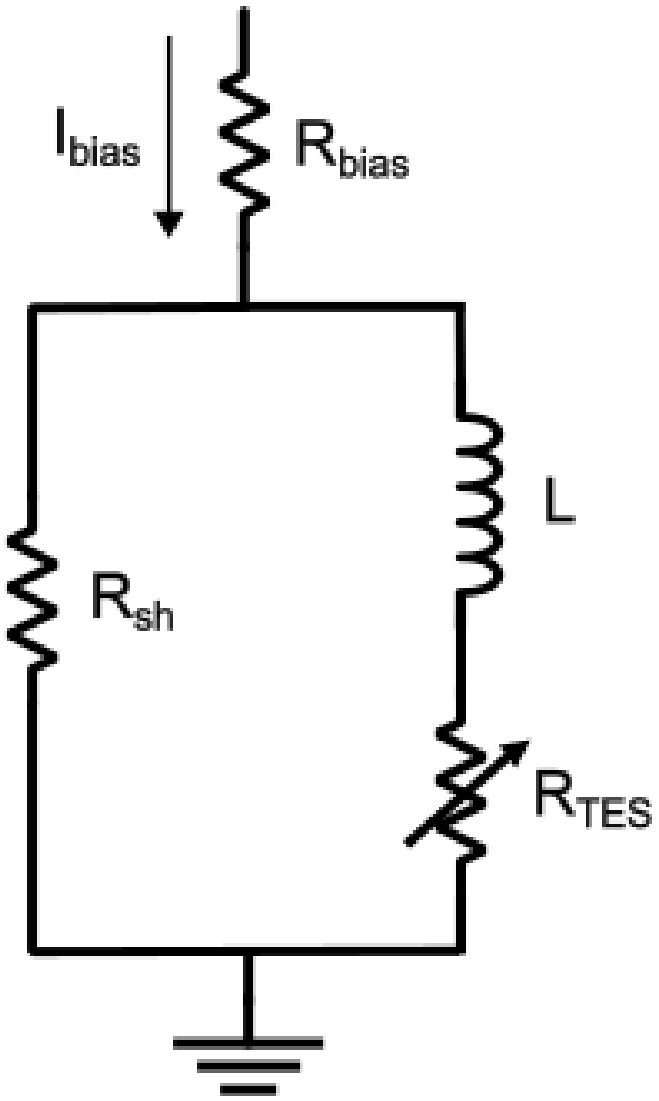

Figure 3.3. TES bolometer circuit.

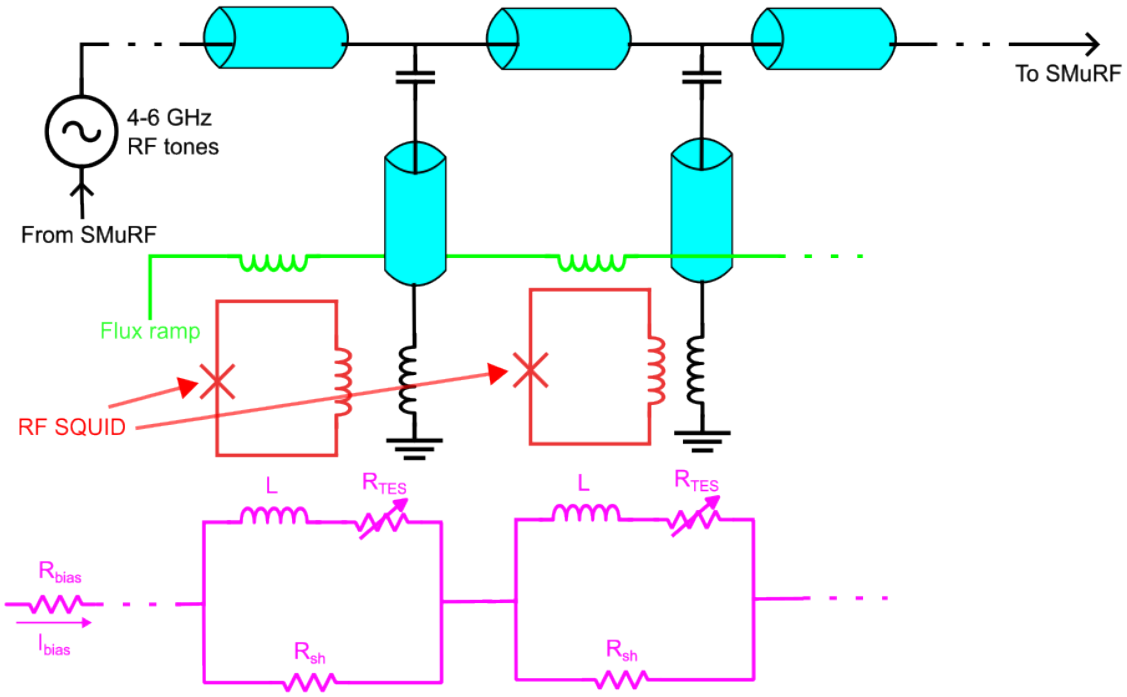

Figure 3.4. Block diagram of the μmux setup. TES bolometers are coupled to RF SQUIDs, which modulate the inductance of LC resonators, changing the resonance frequency. This change in resonance frequency is measured on a common transmission line, allowing many detectors to be read out on a single pair of coaxial cables.

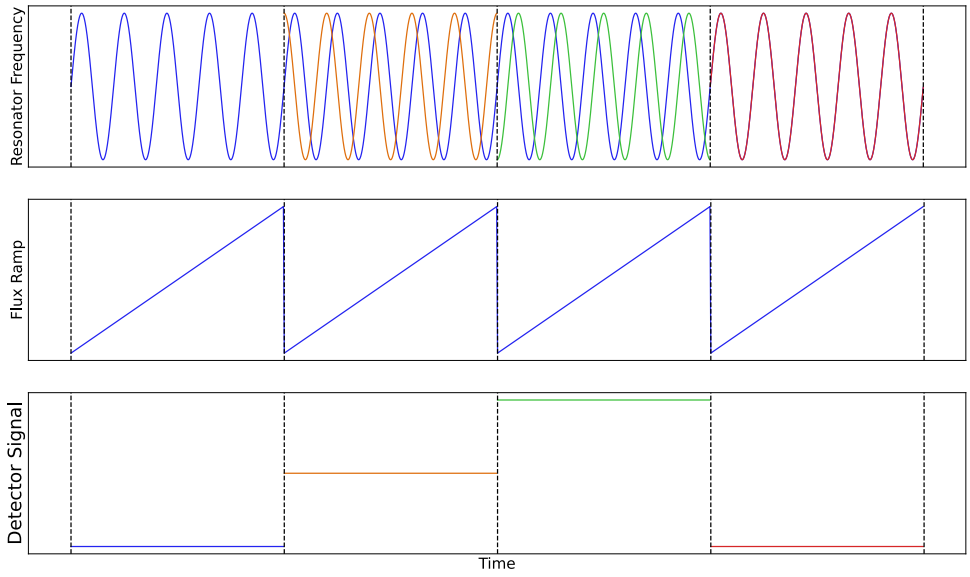

Figure 3.5. Example demonstration of the effect of the flux ramp modulation and changing TES signal on the resonator frequency. The resonator frequency in the top plot is set by the flux ramp amplitude and reset rate in the middle plot. The overall phase shift of the modulated resonator frequency signal is affected by the current through the TES, shown in the bottom plot.

Chapter 4

Development of an Optical Testbed

Before integration into the SATs and the LATR, the UFMs will be characterized fully to ensure suitable detector performance that meets the specifications necessary for SO to achieve its science goals. It is important to establish testbeds that can validate detector performance, since smaller lab testbeds enable faster turnaround times and focused testing, while other aspects of the deployment receivers are investigated and validated. Various SO testbeds are designed to validate aspects of the instrument, such as the optics tubes for the LATR [47] and the dark detector performance [48]·[49].

Optical characterization of the detector arrays is an important step in the validation of the UFMs before they can be integrated into the receivers. In order to perform the required optical testing, it is necessary to develop a testbed optimized to provide SO-specific optical measurements. In these chapter we present the design, construction, and validation of such a testbed. We also describe the test equipment built for use in this testbed, and show preliminary beam map results measured on a prototype UFM.

4.1 Mechanical and cryogenic design

For lab testing of components for the instrument, our testbed employs the same cooling technology as the SO receivers, in this case a Bluefors LD250 dilution refrigerator.[1] In order to

[1] https://bluefors.com/products/ld-dilution-refrigerator/

permit optical testing of detectors for SO, we need to be able to couple optical signals produced in the lab to our detectors housed in the cryostat at the millikelvin stage.

There are two basic requirements when opening the cryostat environment and detectors to external optical signals. First, we must minimally affect the cryogenic environment, i.e. limit the thermal power deposited on the coldest stages of the cryostat. We can accomplish this goal by utilizing infrared-blocking filtering, thereby limiting the cryogenic loading. Second, we must also take care to attenuate as little optical signal in the detector bandpass as possible, since we want to directly probe the properties of the detectors themselves, not the optical components in between the source and the detector. Therefore, whatever filtering we use to limit infrared loading must also minimally decrease in-band electromagnetic power or affect the shape of the spectral response.

These are also constraints and requirements in the design of the receivers for SO, which similarly require coupling a cryogenic environment to an external optical signal in order to observe the CMB signal. We chose to emulate various aspects of the filtering strategy for the SO receivers, both to ensure a level of similarity between the two systems and to take advantage of existing development.

Below, we provide a description of the infrared filter stack utilized in our testbed. We also present the mechanical design of the modifications to the Bluefors LD250 dilution refrigerator to mount the infrared filtering components, as well as the detector arrays under test.

4.1.1 Infrared Filtering

We describe the optical elements at each thermal stage, according to their nominal temperatures (Table 4.1).

300 Kelvin

The 300 K shell is the vacuum shell that houses the cryostat. There are two optical components attached at this stage: a vacuum window and the first of our IR-blocking filters.

The vacuum window is made of ultra-high-molecular-weight polyethylene (UHMWPE), with an expanded polypropylene anti-reflection coating (ARC). The window was fabricated by collaborators at Cardiff University. UHMWPE windows have low in-band loss and are mechanically sound under vacuum, making them well-suited for our applications. See Figure 4.1 for spectral measurements of the window.

Also at 300 K, we mount a metal-mesh reflective filter, a Double-Sided IR (DSIR) filter, designed and fabricated at Cardiff University [34]. The filter is a 4 micron thick sheet of polypropylene with a copper pattern on each side. The pattern on the filter allows transmission of only low-frequency radiation, meaning it can be used as a type of low-pass filter, blocking infrared radiation and transmitting the rest. Spectral measurements of the 300 K DSIR can be seen in Figure 4.2.

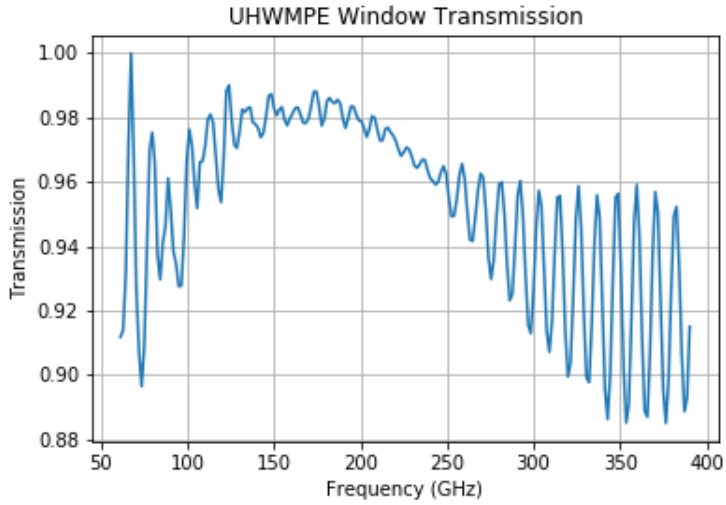

Figure 4.1. Transmission of the anti-reflection-coated ultra-high-molecular-weight polyethylene window, measured at Cardiff University.

40 Kelvin

At the 40 K stage, we have two more infrared blocking filters. The first is another DSIR filter from Cardiff University, similar in concept to the one at 300 K but with different patterning leading to a different effective cutoff frequency [34].

We also use an alumina filter to provide additional infrared filtering. Alumina has high absorption in the infrared but has high transmission in our band of interest, which makes it well matched for our application. The filter itself absorbs infrared radiation and is cooled conductively by the thermal stage it is coupled to due to the high thermal conductivity of alumina [50]. The alumina filter we used was procured from CoorsTek[2] and is 99.5 % pure alumina. The baseline design for the ARC of the alumina filter is to implement the same metamaterial technology as the SO receivers [31].

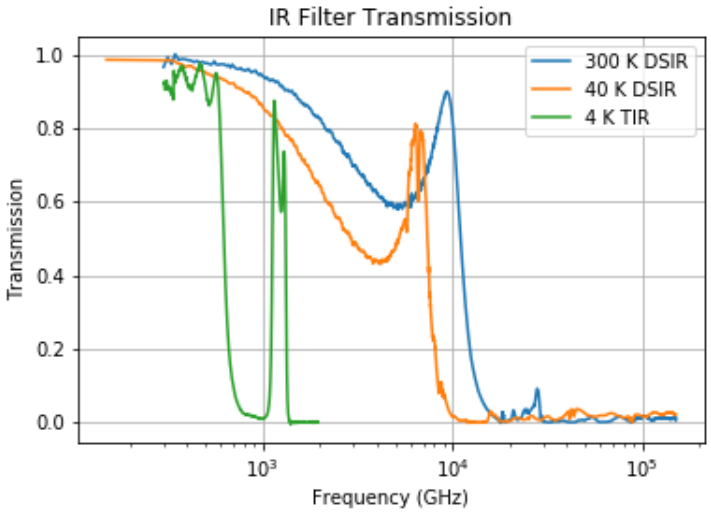

Figure 4.2. Transmission of the 300 K and 40 K double-sided IR filters, measured at Cardiff University, as well as the 4 K thick IR filter.

4 Kelvin

At 4 K, we use another filter manufactured by Cardiff University, a so-called thick IR (TIR) blocker. The filter consists of several layers of metal-mesh filters, similar to the ones at 300 and 40 K, hot-pressed together. Pressing together multiple different layers affects the shape of the transmission curve, providing a sharper cutoff than the filters on the warmer stages. The sharpness of the filtering cutoffs is farther increased at colder stages [34].

[2]https://www.coorstek.com/

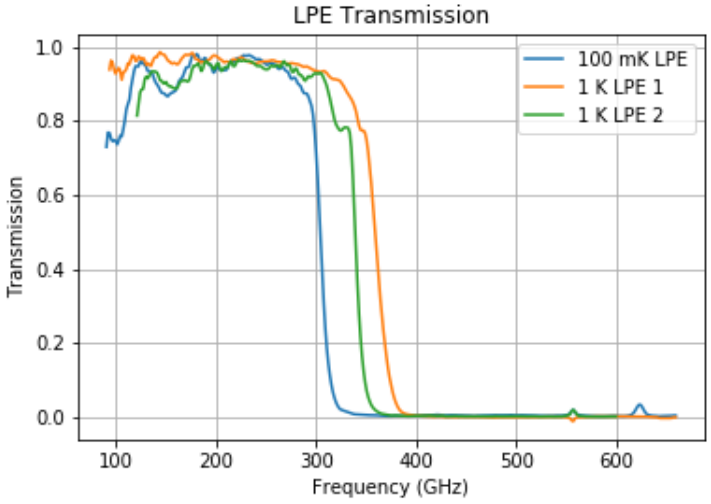

Figure 4.3. Transmission of the three LPE filters, measured at Cardiff University.

1 Kelvin and 0.1 Kelvin

At the 1 K and 0.1 K stages, there are a combined three low pass edge (LPE) filters, which are a variant of the metal-mesh filters described earlier. They consist of a stack of many layers of metal-mesh filters hot pressed together, similar to the TIR blocker at 4 K. With more layers than the TIR blocker, the LPE filters have a much sharper cut-off frequency [34]. There are two filters at 1 K, with cutoffs of 375 GHz and 345 GHz respectively. At 0.1 K, there is another LPE with a cutoff of 315 GHz. The filter cutoffs are chosen to match the SO filtering plan for the UHF bands, in order to allow for detector testing at all six SO bands, while minimizing excess thermal loading on the detectors.

Table 4.1. Breakdown of windows and IR filtering components by cryostat temperature stage.

300 K	40 K	4 K	1 K	0.1 K
UHMWPE Window Cardiff DSIR Filter	Cardiff DSIR Filter Alumina Filter	TIR Filter	12.5 icm LPE Filter 11.5 icm LPE Filter	10.5 icm LPE filter

Figure 4.4 shows the transmission onto the 100 mK stage. We have omitted the alumina filter, as we do not yet have transmission data from an ARC alumina filter in the system. In addition, for the TIR filter we extrapolate the transmission at the lower frequencies in the figure

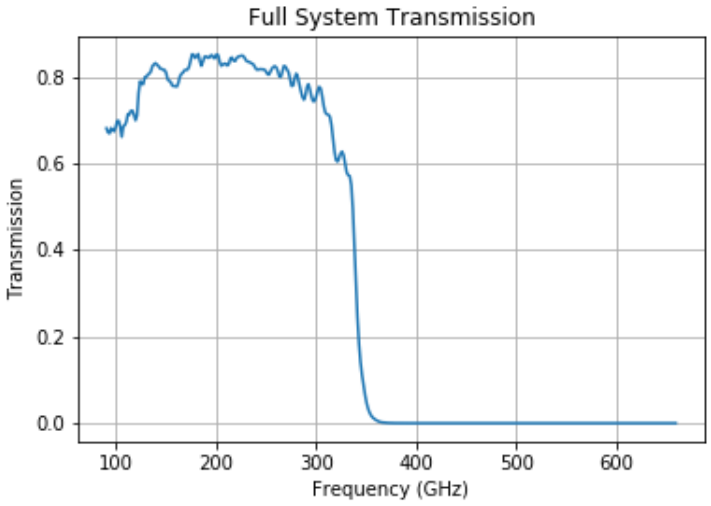

Figure 4.4. Transmission of the full filter stack, up to the 100 mK stage. For the TIR filter, we extrapolated the transmission at the lower frequencies to be the mean of the transmission between 250 and 500 GHz, where we have data. We omitted the alumina filter from this calculation, since we do not yet have data from an ARC alumina filter in the system.

to be the mean of the transmission between 250 and 500 GHz in Figure 4.2, which is a reasonable estimate to make.

Cryogenic Loading Estimates

Using a python package designed to model the thermal performance of the filters in a given radiative environment [51], we estimate the thermal loading due to optical power deposited at each of the given cryogenic stages. These estimates can be seen in Table 4.2. These estimates should be taken as lower bounds on the total loading [28], though we have sufficient cooling power at each stage to accommodate the estimated deposited loading.

4.1.2 Mechanical Design

In order to mount each of the optical components described in Section 4.1.1, we designed a variety of mounting components to address the mechanical requirements needed to ensure good cryogenic behavior at each cold stage.

Figure 4.5 shows the cryostat after the optical components are mounted. A 300 K

Table 4.2. Simulated estimated loading at each temperature stage. The right column shows the nominal cooling power at each cryostat stage, showing that our simulations demonstrate significant margin.

Stage	Predicted Loading	Nominal Cooling Power
40 K	2.015 W	40 W
4 K	0.017 W	1.5 W
1 K	1.25 mW	20 mW
0.1 K	4.9 μW	250 μW

extension was made to ensure adequate space for the vacuum window and the 300 K and 40 K filters without any cryogenic touches.

Since the 40 K alumina filter relies on radial thermal conductivity to filter the incident IR radiation, good thermal contact between the alumina disk and the 40 K shell of the cryostat is imperative. In order to promote this thermal contact, the mounting rings are made from aluminum 1100, which has higher thermal conductivity than other aluminum alloys. In addition, we use Spira spring gasket[3] to provide uniform axial pressure to ensure good thermal contact between the alumina disk and the baseplate. It is important to also provide room for the thermal contraction of the alumina disk and its aluminum mounting rings. Since the coefficient of expansion is substantially different between the alumina ceramic and the aluminum rings, it is important that the alumina is not constrained too tightly during large thermal changes; otherwise, it can shatter. The Spira gasket provides a good compromise between promoting good thermal contact and allowing enough freedom to prevent shattering during contraction and expansion.

The mounting for the TIR filter and the LPE filters is similar to that of the alumina, but with the depth of each pocket in the mounting rings tuned to the measured thickness of the filter. Similar to the alumina, we need to account for the differential thermal contraction between the aluminum mounting rings and the polypropylene substrate of the TIR and LPE filters. The geometry of each set of mounting rings is designed to keep from over-constraining the filters, which could cause mechanical stress to the filters during the cooling and warming processes.

[3]https://www.spira-emi.com/

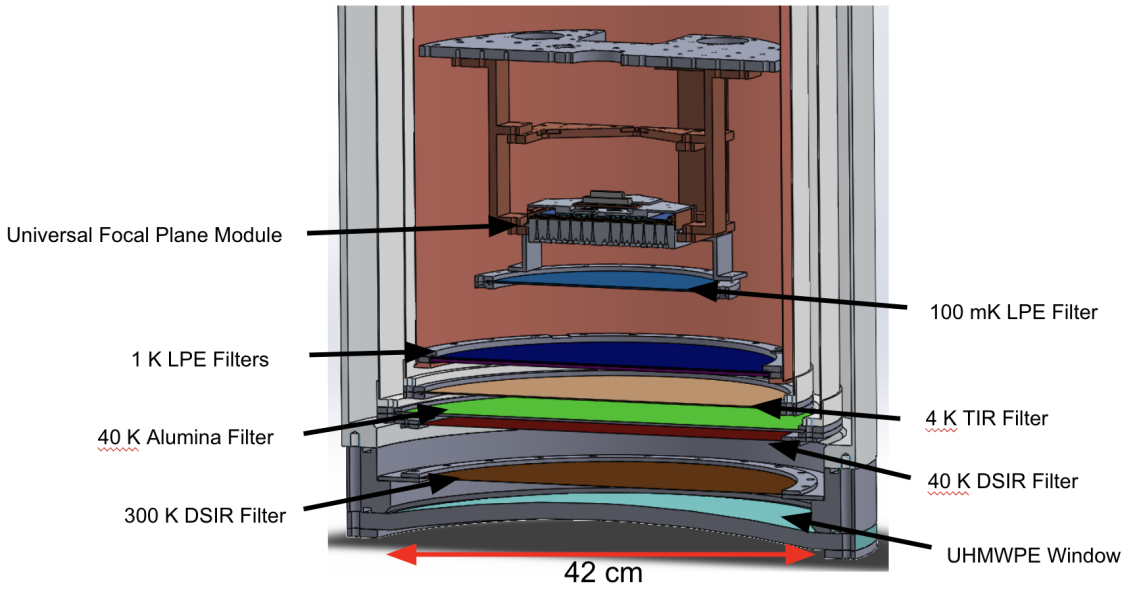

Figure 4.5. Modified cryostat with windows and filters installed to allow for optical access to detectors.

The thermal contact between the mounting rings and the filters is less important than for the aluminum: the radial thermal conductivity of the polypropylene substrate is low enough that the bulk cooling of the filter happens due to its radiative coupling to the cryogenic environment.

4.1.3 Performance Validation

All optical components have been successfully integrated into the system, with minimal effect on the cryogenic performance of the system. Base temperatures for each stage with the filtering fully integrated are presented in Table 4.3. Further testing is underway to estimate the exact loading on the millikelvin stages where the detectors are mounted.

4.2 Testing Hardware and Capabilities

We outline the design and implementation of the equipment and hardware for optical detector characterization.

Table 4.3. Base temperatures achieved with all filters and windows installed.

Cryostat stage	Dark Base Temperature (K)	Optical Base Temperature (K)
PTC1	41.8	44.7
PTC2	3.2	3.5
Still	0.745	0.979
Mixing Chamber	0.021	0.041

4.2.1 Cryogenic RF Readout Chain

The RF wiring chain installed in the cryostat in order to couple the room temperature readout electronics to the cold microwave multiplexing (μMux) components is designed to be the same as is implemented in the SO cameras [39]. This ensures minimal variance between the testing environments.

4.2.2 Optical Testing Hardware

The main optical testing equipment designed for use on the testbed are a beam mapper and a Fourier transform spectrometer (FTS). Below we describe the modifications to the test equipment to couple to our testbed, and the capabilities each piece of equipment provides.

Beam Mapping

A detector's angular response function, more commonly referred to as its beam, describes how the detector will couple to the telescope optical system, and the CMB sky signal. Measuring the detector beam in the lab allows us to make an isolated measurement of the angular response of the detector itself, without complications from the optical system in which it will be used.

In order to measure the detector beam, we scan a thermal source across the field of view of the detector and measure the detector response at a given source position. Then, knowing the distance from the source to the detector, we can reconstruct the angular response function of the detector.

Given the wide optically active area of the cryostat, we are able to measure the detector

beams out to a beam half-angle of 40 degrees for a center pixel and 30 degrees for an edge pixel on an SO UFM.

The beam mapper consists of a chopped thermal source coupled to x-y linear stages. The entire system is coupled to an 8020[4] mounting frame that allows for adjustment in the z-direction to enable changes in the mapped resolution. There are also multiple apertures that can be replaced in front of the thermal source to change the size of the source beam, affecting the resolution of the resulting beam map. The linear stages are commercially-available stages purchased from LinTech Motion.[5] There are two thermal sources that can be used interchangeably in the beam mapper: a liquid nitrogen source or a heater source that can reach temperatures of 900 °C. In addition, a rotating wire grid fabricated using an in-house grid winder [52] can be put in place to perform polarization maps and cross-polarization measurements.

All components of the beammapper have been assembled and validated, and some were also used for validating the SAT in lab, as described in chapter 5.

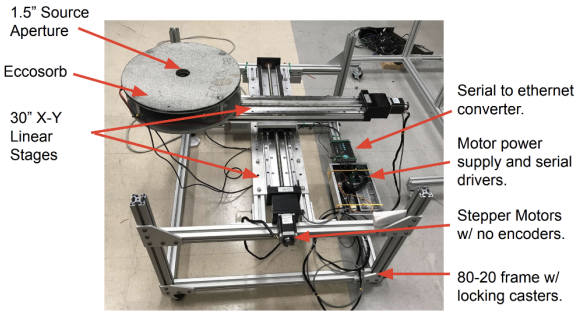

(a) Beammapper setup on its cart.

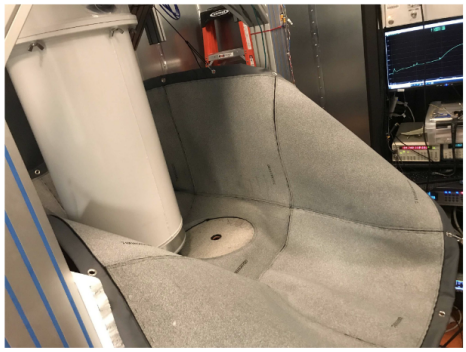

(b) Beammapper setup in the RF room.

Figure 4.6. (Left): Beammapper setup on its cart. (Right): Photo of the beammapper setup in the RF room underneath the test cryostat. Also included is the eccosorb blanket to suppress stray reflections.

[4]https://8020.net/
[5]https://www.lintechmotion.com/

Fourier Transform Spectrometer and Spectral Measurements

The detector bandpass is defined by on-chip filtering on the detector wafer and is an important aspect of detector characterization, since it defines what frequencies the detectors are sensitive to. Similar to measuring detector beams, measuring detector bandpasses in a separate testbed allows us to decouple the detector bandpass from any end-to-end features in the bandpass of the final integrated camera.

An FTS measures detector bandpasses. In particular, we are using an FTS whose design is based on the instrument used to characterize detectors for the POLARBEAR experiment [52]. The FTS is a Martin-Puplett interferometer with a maximum spectral range up to 500 GHz and a spectral resolution of 1 GHz or 0.5 GHz, depending on the operating mode. The FTS source is the same as the heater source used in the beam mapper. The FTS can be used to measure both the spectral response of the detectors and the polarization angle of the detector as a function of frequency, especially useful for characterizing the known polarization wobble of the sinuous antennas in the LF detectors for SO.

There are many systematic errors that can arise in performing spectral measurements with an FTS, one of which is improperly filling the beam of the detector. If the detector beam is not fully filled by the FTS signal, it can introduce spurious fringing in the measured band [53]. To mitigate this effect, the optical coupling of the FTS must be designed to ensure detector beam-filling. Given the mechanical constraints of the testbed and the surrounding RF room, several modifications were required to the FTS optical design. First, we replaced the f/2 output parabolic mirror with a faster mirror to reduce the focal length of the optics, compressing the entire FTS system. Then we designed and fabricated an off-axis elliptical coupling mirror designed to focus the FTS output signal onto the detectors under test. A ray trace of the coupling mechanism can be seen in Figure 4.7. A more detailed description of the optical coupling design can be found in Appendix A.

A mounting structure for the FTS and mirror system was designed out of aluminum 8020,

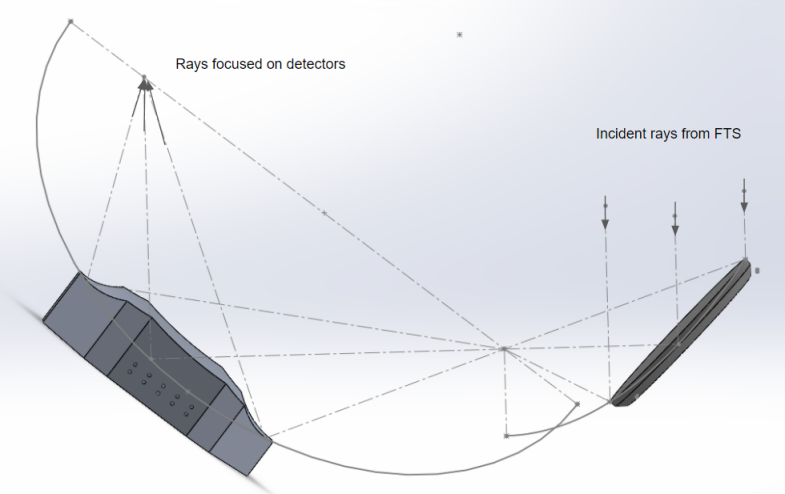

Figure 4.7. Ray trace of the FTS output parabolic mirror (right) and the elliptical coupling mirror (left). The underlying mirror curves are also pictured. The system takes in collimated rays from the FTS and focuses them onto the detectors under test, ensuring correct optical coupling to the full throughput of the detectors used in the actual instrument.

which enables adjustments in the alignment of the system, as well as translation in the x- and y-directions to measure many detector bandpasses in a single cooldown, regardless of detector offset. The structure can be seen in Figure 4.8.

4.3 Measurements and Results

Preliminary beam measurements were performed to validate the system. In addition, this helped validate the test equipment for use in the SAT testing in chapter 5.

A sample beam map was taken with a source temperature of $\sim$760° C. The chopper was spun at 6 Hz, and the stages were stepped in 0.75 inch steps from 4 to 16 inches in each dimension, where 0 corresponds to the far corner of the coordinate system. At each step, we integrated for 20 seconds to ensure good data quality.

An example 150 GHz beam and 1-D cuts can be seen in Figure 4.9. In the beam map performed for the plot, the total scan area was restricted in order to perform a faster map.

Figure 4.10 shows histograms for the half-width-half-maximums (HWHMs) measured in angular space for the detectors. We have also overplotted the expected beam sizes from

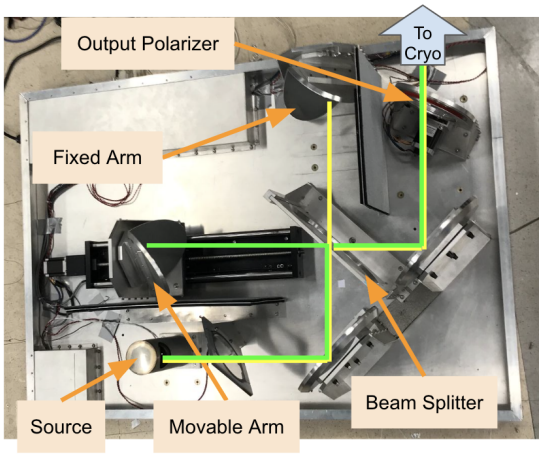

(a) Annotated photo of the FTS fully assembled before the enclosure cover is placed on.

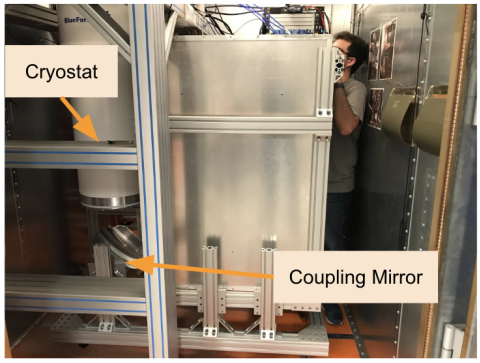

(b) Photo of the FTS on its cart with its coupling mirror installed. The full assembly is positioned next to the test cryostat.

Figure 4.8. FTS, cart, and mirror designed and built for coupling to the optical test cryostat.

simulations. While there is close agreement for the 150 GHz detectors, the 90 GHz detectors are saturated and not behaving properly.

4.4 Acknowledgements

Chapter 4, in part, is a reprint of the material as it appears in Joseph Seibert, Peter Ade, Aamir M. Ali, Kam Arnold, Nicholas F. Cothard, Nicholas Galitzki, Kathleen Harrington, Shuay-Pwu Patty Ho, Brian Keating, Lindsay Ng. Lowry, Megan Russell, Maximiliano Silva-Feaver, Praween Siritanasak, Grant P. Teply, Carole Tucker, Eve M. Vavagiakis, and Zhilei Xu. "Development of an optical detector testbed for the Simons Observatory". In: *Millimeter, Submillimeter, and Far-Infrared Detectors and Instrumentation for Astronomy X*. ed. by Jonas Zmuidzinas and Jian-Rong Gao. Vol. 11453. International Society for Optics and Photonics. SPIE, 2020, p. 114532C. DOI: 10.1117/12.2562045. URL: https://doi.org/10.1117/12.2562045.

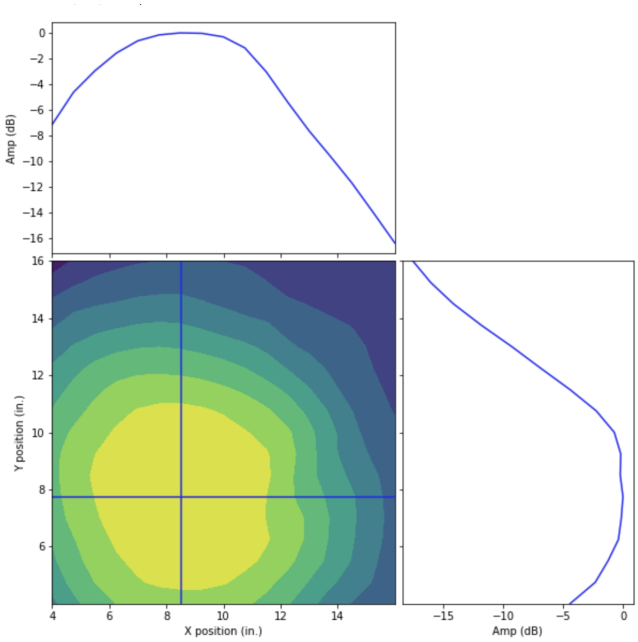

Figure 4.9. Example 150 GHz beam measured in the UCSD detector testbed on a prototype detector module. Cross-sectional, 2-D cuts of the beam are also plotted. The beam size matches closely with design values for the beam size in position-space.

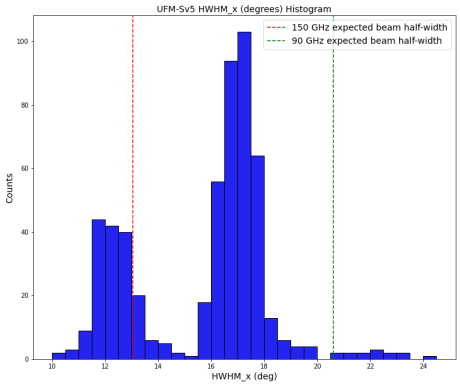

(a) Half-width-half-maximums in the X dimension.

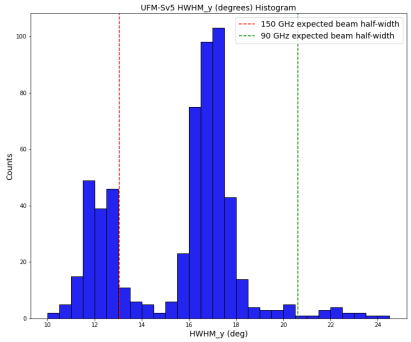

(b) Half-width-half-maximums in the Y dimension.

Figure 4.10. Measured HWHMs in angular space compared to the simulated expectation for the MF UFMs. The two populations in the histograms should be the 90 GHz vs 150 GHz detectors, but the 90 GHz detectors are saturated and thus the results are not accurate. However, the 150 GHz detectors show good agreement with the expected results.

Chapter 5

SAT MF-1 Integration and Testing

5.1 Introduction

As SO's first-light instrument, SAT MF-1 went through a thorough in-lab testing and validation program, which started upon receipt of the cryostat shells in June 2019 and completed in March 2023. Each subsytem was tested individually, in a phased integration system where dedicated cooldowns were used to verify that everything was functioning to specification before moving on to the next. The complexity of the instrument increased with each subsequent cooldown, with replacements and repairs occurring in between each phase if anything unexpected occurred.

The final validation phase involved building up the SAT in as close to a deployment-like configuration as possible, including antireflection-coated optical elements and a fully populated focal plane, as well as deployment-grade room-temperature electronics. This section will focus on this final phase, particularly on optical validation of the SAT and its focal plane. Prior integration and validation of the remainder of the SAT subsystems can be found in [29], [30], [54].

5.2 Detector Validation

Detector validation is described in more detail in [55]. For the purposes of this work, a brief summary will be presented to provide context for the description of the optical testing

program.

Of the seven UFMs installed in the SAT, six were operational and tested during this final validation phase. The seventh, UFM-Mv7, was found to have electrical issues that prohibited operation during the cooldown, but will be repaired before deployment and has been tested in other cryostats before. Figure 5.1 is a schematic demonstrating the layout of the installed UFMs in the focal plane.

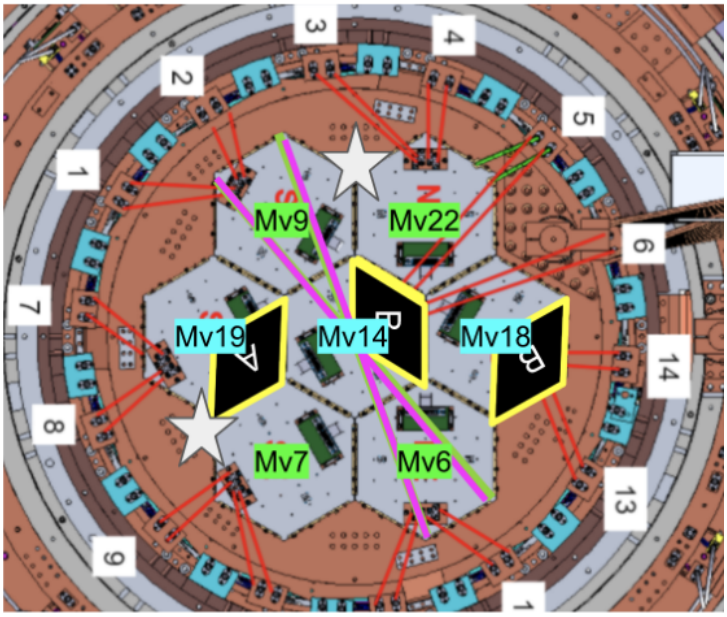

Figure 5.1. Layout of detector modules installed in the SAT for the final validation run, as viewed from behind. Mv7 was not operational during the run, and Mv14, Mv6, and Mv9 will be replaced when the SAT is installed at the observation site with detector modules that were validated in other test cryostats. Diagram courtesy of Daniel Dutcher, Erin Healy, and Marius Lungu.

Of the seven modules, four will be deployed with the SAT and integrated into the receiver for observations, while the other three will be replaced with previously validated arrays whose parameters more closely match the operating environment of the SAT. In particular, the optical loading on the MF-1 detectors was higher than originally anticipated in the detector parameter design phase, meaning those detectors were operating in the low loop gain limit, which led to higher than anticipated time constants. The replacement modules have slightly higher saturation powers, which when combined with the sky loading conditions are expected to operate in a more

nominal state. Table 5.1 has a summary of the measured detector parameters, broken down by UFM. The first three columns of the table are the modules which will deploy with the instrument, and the final three are the modules that will be replaced.

5.3 Optical Validation

A large portion of the final in-lab testing program for the SAT involves verification of the optical properties of the full telescope system. Some aspects of the detector modules or the SAT optical elements have been tested individually, but these in-lab measurements constitute the first time the entire fully coupled SAT system has been verified before integration with its platform at the Chilean observation site. Validation of the optical properties in lab is crucial before deploying the instrument to the site because any inconsistencies or unexpected failures can be addressed in the lab instead of later in the commissioning process. SAT MF-1 is the only one of SO's SATs that will undergo detailed optical testing, and so validation of all of these components is crucial not only for the success of the instrument, but for the entire SO SAT program.

Sections 5.4 and 5.5 describe some general aspects of the optical testing setup, then 5.6-5.8 describe the optical measurements I was responsible for: beam mapping, spectral measurements, and polarization measurements.

5.4 Neutral Density Filters

The detectors for the SAT are designed to observe the cold, high-elevation sky, and as such have saturation powers tuned for a much lower background signal. Even without brighter thermal sources used for optical testing, the conditions in the lab would cause the detectors to saturate and be unable to biased into an operable range for lab testing. This necessitates the use of additional attenuation, to reduce the incident power on the detectors from the lab and any additional thermal sources. The common way to accomplish this is via the use of cold attenuating filters, frequently referred to as Neutral Density Filters (NDFs). Though we will use

Table 5.1. Detector properties measured in the final validation run. The increased time constants are evidence of being in the low loopgain limit, which makes it more difficult to interpret detector testing results in the lab, and if like this in the field, more difficult to analyze the data from the detectors.

	Band	Mv18	Mv19	Mv22	Mv14	Mv6	Mv9
Operating Resistance (R/R_n)	MF-1	0.49±0.07	0.53±0.07	0.60±0.16	0.50±0.7	0.51±0.10	0.58±0.15
	MF-2	0.44±0.03	0.44±0.02	0.50±0.08	0.45±0.03	0.46±0.03	0.47±0.03
Time constant (ms)	MF-1	3.04±1.35	1.29±0.32	3.62±0.91	5.18±2.79	2.61±0.66	1.86±0.78
	MF-2	0.69±0.05	0.69±0.07	0.63±0.08	1.12±0.14	0.95±0.10	0.90±0.09
TES Total Noise (aW/$\sqrt{\text{Hz}}$)	MF-1	15.309	18.941	17.388	10.843	16.955	11.420
	MF-2	19.989	19.450	32.730	17.340	18.639	16.218
Optical Yield (%)	MF-1	82.47%	88.64%	91.87%	75.57%	77.51%	82.94%
	MF-2	91.30%	89.22%	91.96%	79.32%	76.63%	90.81%

this terminology for the remainder of the discussion, this term is notably inaccurate, as the filters have a strong frequency dependence, i.e. they are distinctly non-neutral, as can be seen in the measured transmittance in Figure 5.2.

The NDFs used for the SAT are 12.7-mm thick pieces of Eccosorb MF-112, which is a magnetically loaded machinable epoxy block. The material is chosen for repeatability and consistency with previous measurements, and the thickness is chosen such that both the MF-1 and MF-2 detector bands will have enough dynamic range to be able to be biased into the linear range of their transitions. In the measurements below, this is actually not the case for many of the MF-1 detectors, due to an error in modeling the expected optical load on the detectors in this frequency band.

Measurements of the transmission of the NDFs are crucial to be able to correct out their effect, particularly for optical efficiency and spectral measurements. However, these measurements are very difficult, due to the very lossy nature of the dielectric. From measurements of a variety of samples, we chose to use the MF-112A model as measured in [56], because it is the closest to an on-axis measurement. This transmittance is reproduced in Figure 5.2. In addition, measurements of the optical efficiency of the full end-to-end SAT optical system described in [55] are consistent with an NDF with the transmission profile described here.

We mount the NDFs 0.5 mm over the detector modules, attached to the focal plane via aluminum stand-offs. There are small spaces in between each NDF, but this still makes available the majority of the optically active area of the detector modules. A photo of the mounted NDFs can be seen in Figure 5.3.

5.5 Test Equipment Mounting Frame

The angular dependence of the cooling power of the PTCs and DR in the SAT restrict us from pointing the SAT at horizon in lab, which means that for optical testing, the SAT must be pointed at zenith. In order to mount test equipment in front of the window, we built a mounting

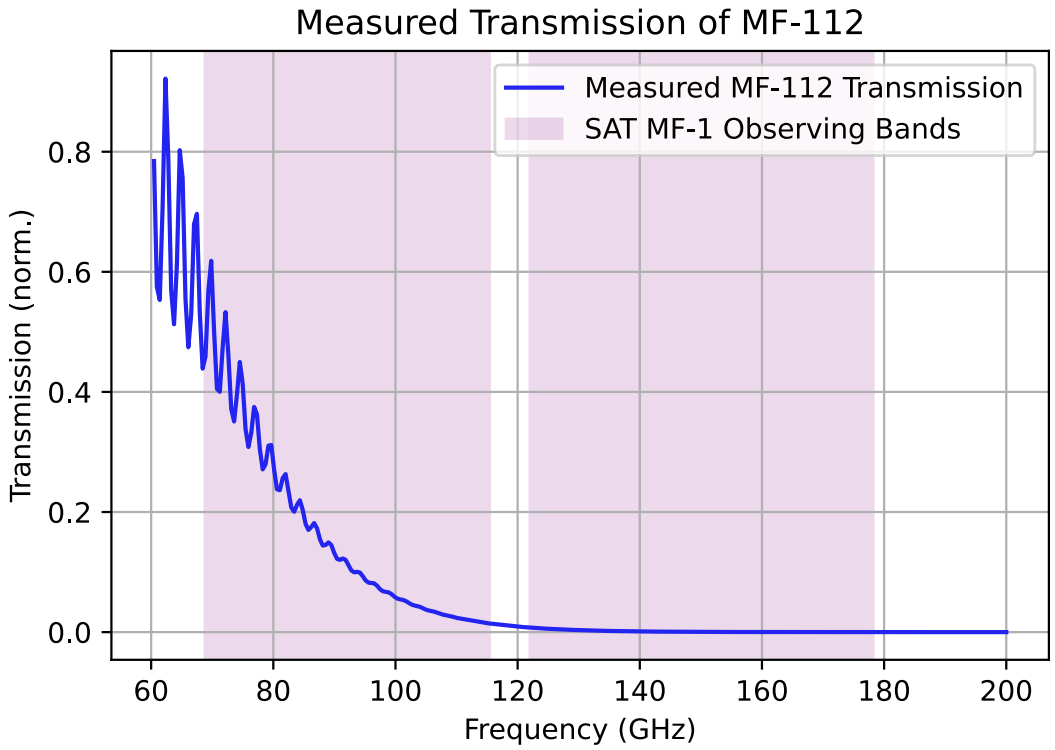

Figure 5.2. Measured transmittance of the MF-112 samples used for attenuating room-temperature signals for in-lab measurements [56].

frame out of T-slot aluminum that can support the weight and move freely around the lab. A picture of the mounting frame can be seen in Figure 5.4.

5.6 Beam Mapping

Beam mapping is a measurement designed to characterize the angular response function of the combined optical system. Any signal measured by the instrument is the convolution of the instrument beam and the real source profile, so understanding the beam is crucial for accurate measurements of the CMB [57]. From a lab-testing perspective, measurements that confirm there are not significant deviations of the beam profile from its design give us confidence that the instrument is performing to its designed specifications and is ready to begin commissioning at the site.

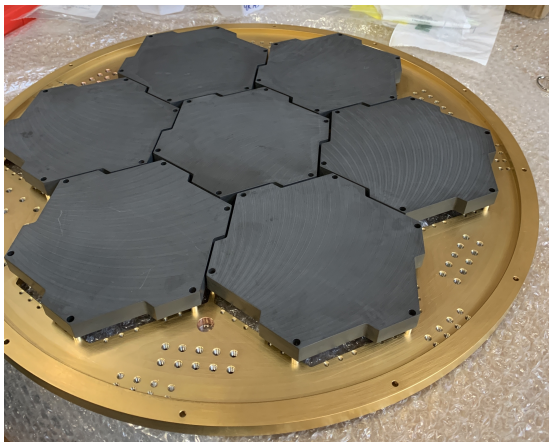

(a) NDFs mounted onto the sky-side of the focal plane.

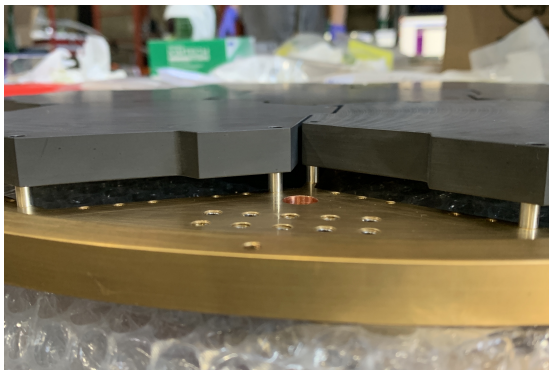

(b) Aluminum standoffs used to keep the NDFs from impinging on the horn arrays of the UFMs.

Figure 5.3. NDF installation on focal plane base before final validation cooldown.

5.6.1 Experimental Setup

In order to measure beams, we move a chopped thermal source in front of the window of the SAT and record the detector signal as we move to various positions. The angular size of the source is much smaller than the beam, such that we are able to resolve sub-beam variation and understand the profile more fully. Given physical constraints, we place the source in the near field of the telescope. More specifically, the source is mounted 81 cm above the SAT aperture stop.

The source sits at $\sim$760 °C, and for the measurements presented is modulated at 6 Hz by a chopper wheel. Modulating the source allows us to reduce noise by minimizing the effect of long timescale drifts in the system and allows us to isolate the source signal from the background. We place a 3.8-cm aperture over the source and chopper wheel assembly to ensure that the only modulated signal the detector observes is directly from the hot source. The source is mounted on X-Y stages, which are in turn mounted on the test equipment frame described in section 5.5.

In order to reduce background contribution and mitigate contribution from systematics, we use a blanket made from Eccosorb AN-72 mounted onto a tarp. Reflection off nearby surfaces can contribute to spurious detector signal, and the Eccosorb blanket acts as a way to minimize

Figure 5.4. Photo of test equipment mounting frame, built out of T-slot aluminum.

stray reflections from nearby bright surfaces entering the cryostat window. Viewed in the reverse-time paradigm, any photon emitted by the detector terminates on either the Eccosorb blanket or the modulated hot thermal source.

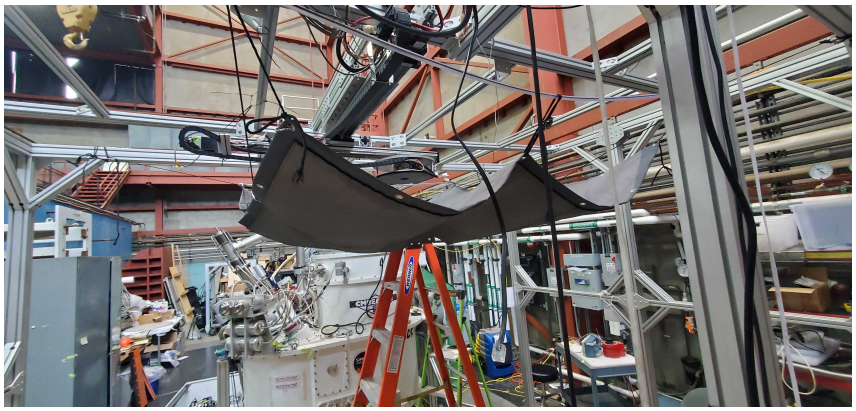

Figure 5.5. X-Y stages, source, and chopper installed on the mounting frame, along with an Eccosorb blanket to minimize stray reflections and pickup off the metal frame.

5.6.2 Measurements

The source was stepped from in a 38 cm by 38 cm square in 1 cm steps in a raster scan pattern with an integration time at each step of 1 second.

In order to process the beam maps, we load a raw timestream for a detector. We apply a 2 Hz high-pass Butterworth filter to remove unwanted low-frequency drift from the time-ordered

data. Afterwards, we demodulate the signal by assuming the chop is a stable 6 Hz. Then, we bin the detector signal at each position of the source over the full scan pattern to extract the final beam map. We expect the output beam to look like a two-dimensional Gaussian truncated by the aperture stop, where the width of the Gaussian depends on the frequency of the detector, and the truncation aperture depends on the position of the detector along the focal plane.

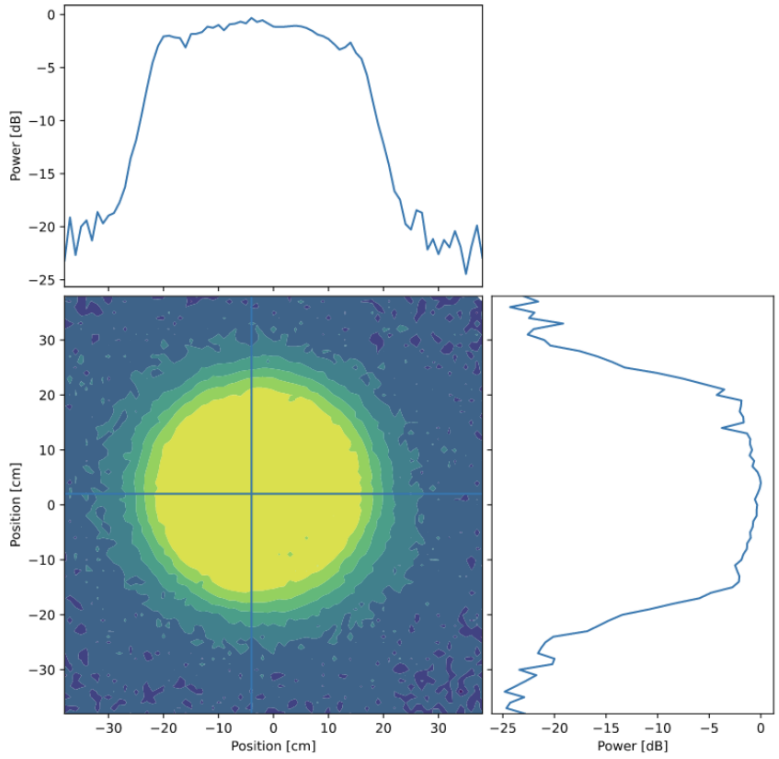

Figure 5.6. Sample detector beam measured from a 90 GHz detector. The beam is plotted on a log scale and peak-normalized. 1-D cuts are shown through the center of the beam.

In order to compare the performance of the SAT to design, we need to compare our near-field beam measurements to simulations. Because the signal is collimated, taking spherical wavefronts with center of curvature near the horn aperture to planar wavefronts at the output of the receiver[1], the effects of diffraction are important and we must use simulations that include these effects to model the full behavior of the beam exiting the SAT, as well as remember that

[1]At the horn aperture, the wavefronts are actually flat, but expand to spherical wavefronts through diffraction.

we are averaging these effects across the bandpass of the MF-1 and MF-2 detectors, respectively. The simulations must also be directly comparing the beam at the source plane of beam mapper to the measured beams. The only such simulations we have are of the central pixel and can be seen below in Figure 5.7. Off-axis effects should be minimal and will mostly appear as the output beam appearing more elliptical. Simulations shown here were provided by Jón Gudmundsson at Stockholm University and were performed in the GRASP software suite.[2]

Simulations like these in the near-field often contain non-physical artifacts that look like fringing and are a function of where you choose to place the source plane. To better compare to our measured results, we average out these fringing effects and re-normalize the simulated beams.

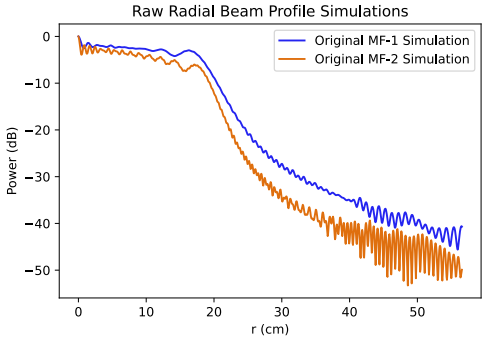

(a) Original beam simulations for both bands. The fringing here is an artifact of selecting a particular plane for the near-field beam simulations.

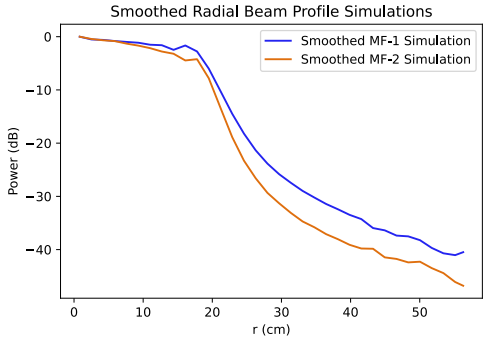

(b) Simulations after smoothing the fringing and re-normalizing.

Figure 5.7. Simulated radial beams for comparison to measured beam profiles. Simulations provided by Jon Gudmundsson.

To compare the measured beam shape to the simulations, we radially bin the detector beam and then do a weighted average based on signal-to-noise ratio (SNR), with the goal of reporting one averaged beam per module. Then, we extract a half-width-half-maximum (HWHM) for each UFM and compare to the HWHM extracted from the simulations. When overplotted in Figure 5.8, the agreement in the main beam between the measured beams and the simulated

[2]https://www.ticra.com/software/grasp/

beams is clear. The noise floor of the measurement limits our ability to see the beam profile at large radii.

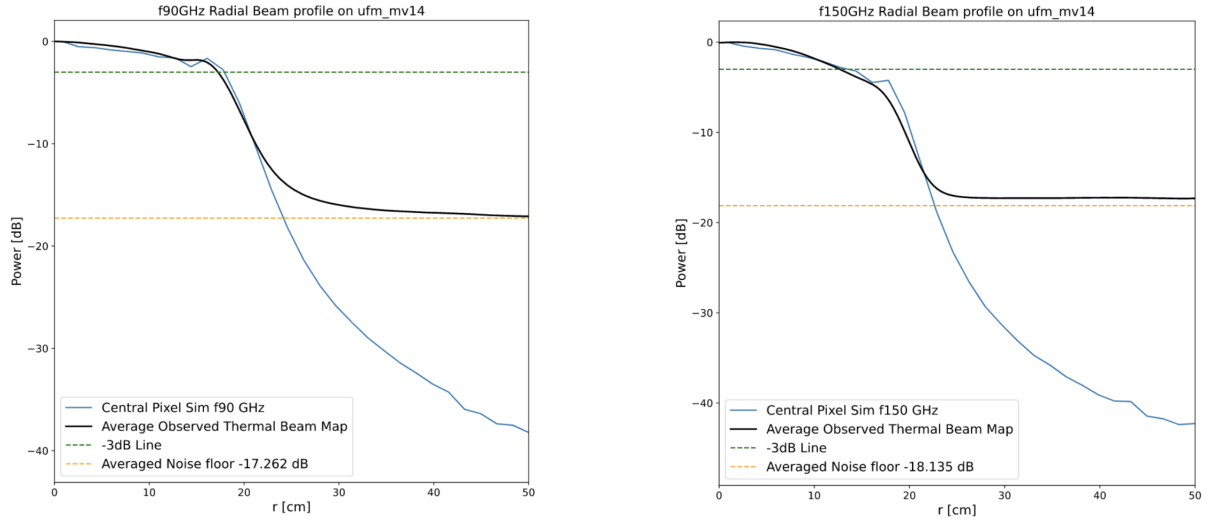

(a) MF-1 Band **(b)** MF-2 Band

Figure 5.8. Comparison between measured beam profiles from the central UFM, UFM_Mv14, and the simulated beam profiles. The HWHM are calculated as the -3 dB points for both the simulated profile as well as the measured profile. The measured profile represented in the plot is an average of all detectors, weighted by signal-to-noise ratio in each map. Also plotted is the averaged noise floor for the detectors, demonstrating that the roll-off at higher radii in the measurements is due to the residual noise when the source is not illuminating an individual detector beam, as compared to the simulation's ability to describe much further beam radii.

Summary statistics for each UFM measured can be seen in Table 5.2. We can only directly compare the central pixel to the simulations, but we see the expected trend across the full focal plane, where the measured HWHM is larger for the off-axis detectors than those on-axis, which is an effect of radially binning an ellipse as compared to a circle.

The requirement for completion of the in-lab testing program for the SAT is that we observe minimal deviation of the main beam from simulation. More specifically, we require that we do not see a deviation of greater than 2 dB between measurement and simulation out to -10 dB of the overall simulation amplitude. We can only directly compare the central UFM to the simulation, but we pass this requirement, as seen in Figure 5.9, which, when taken in concert with dedicated holography phase-sensitive measurements of the SAT optics [58], validated the

Table 5.2. Measured HWHMs for each UFM's averaged beam profile, derived from radial beam profiles like Figure 5.8. Simulations are only for a feedhorn at the center of the focal plane, which is most closely aligned with Mv14. The other modules do not have simulations to compare against, but the increase in size relative to the central UFM is expected as a result of the off-axis elliptical projection of the beams onto the aperture stop.

	Simulated Value	Mv14	Mv18	Mv19	Mv22	Mv6	Mv9
HWHM MF-1 (cm)	17.8	17.25	17.82	17.76	17.71	17.65	17.71
HWHM MF-2 (cm)	14.1	12.78	13.63	14.82	14.31	13.69	15.61

beam performance of the SAT for deployment.

5.7 Spectral Measurements

Measurements of the spectral properties of the SAT and its detectors are important for characterizing both in-band and out-of-band transmission. Both are important for understanding the sensitivity of the instrument, and these are the first measurements of in-band performance for a deployment-grade receiver coupled with detectors for SO.

We use a combination of Fourier transform spectroscopy and thick grill filter measurements to characterize the spectral performance of the system. These measurements are just used for validation of the instrument, with final calibration-quality measurements to be performed when the SAT is integrated into its platform at the observing site.

5.7.1 Fourier Transform Spectroscopy

Experimental Setup

With this measurement technique, a Fourier Transform Spectrometer (FTS) is used to measure the end-to-end spectral response of the SAT's optical elements and detectors. The FTS is an interferometer acting with a broadband source [59]. As the movable mirror is scanned, the resultant detector response is recorded as a function of mirror position, and the Fourier transform of the measured interferogram is the spectrum of the system.

In these measurements, the FTS used was built by collaborators at the University of

Chicago, inspired by a design made for the Primordial Inflation Explorer (PIXIE) [60]. We use a $\sim 560^{\circ}$ C ceramic lamp for the source, and chop it at 2.6 Hz before it enters the FTS. Inside the FTS, the source is polarized using polarizing grids. Typically, the output of the FTS must be properly coupled to the detectors, such that the FTS signal fills the beam of the detectors. This mitigates systematic effects, typically observed as fringing inside the band. For lab measurements, it was determined that the most important aspect to measure was the location of the band edges, which are minimally effected by optical coupling, so the output of the FTS was re-directed with a folding flat mirror into the SAT optical system, instead of a more complicated mirror coupling design. For science-grade calibration measurements, a complete coupling optics system will be integrated onto the SAT at site.

The combined FTS, souce and chopper, and folding flat system were mounted on the test equipment frame, with sliding mounts to allow for X-Y position adjustments, and a hinge that allowed adjustment of the folding flat to steer the FTS output at different angles.

Measurements

Given the size of the FTS output, it is not possible to illuminate the entire SAT focal plane in a single measurement. In order to measure multiple UFMs, we adjusted the angle of the folding flat to illuminate a different set of detectors between measurements, as well as moved the X-Y position of the FTS system. This adjustment process was performed empirically, by viewing live-streamed data while adjusting mirror angle and position until the 2.6 Hz chop was approximately maximized for the desired set of detectors. Figure 5.11a shows an example of this chopped signal in the downsampled detector data.

Given physical constraints, we were unable to measure the full focal plane by following the system described above. Positioning of warm housekeeping electronics and the warm readout electronics limited the available adjustment range and left us unable to measure all six operational modules. Data reported below is for the three UFMs we were able to measure, two of which will be integrated into the SAT during commissioning. The three UFMs also provided end-to-end

focal plane coverage, which reduced risk associated with any radial effects to the end-to-end spectral performance.

For each scan, the FTS movable mirror was scanned from -37.5 cm to 37.5 cm in 0.15 cm steps. This provided a 1.02 GHz resolution spectrum with a maximum frequency of 256 GHz.

To extract bandpass data for each detector, we first load the raw timestream and then apply a bandpass filter between 2 and 3 Hz. The filter helps reduce power in unwanted frequencies, since the FTS signal is less bright than the beam-mapper source. After the filter, we demodulate the signal at 2.6 Hz, and then bin the mean detector signal for each step of the movable mirror. This provides a raw interferogram, which can then be cleaned further by removing any glitches or trends in the baseline. To pull out the bandpass, we perform a Fourier transform on the interferogram. Similarly to the beam map measurements, we compute module-averaged bandpasses using the SNR of a particular spectrum as its weight.

The resultant spectra are the combined transmission of each optical element in the SAT as well as the on-chip filters on the detector wafers. However, this includes the NDFs that we use to attenuate the room-temperature optical signal, which are only used in lab testing and thus not included in simulation, which is what we need to compare our measurements against. Since the NDF has a frequency dependence, we have to correct out this effect before we can verify that the spectral performance of the SAT is as expected.

Using the transmission measurements described in 5.4, it is relatively straightforward to remove the effect of the NDF, albeit with a substantial error bar driven by difficulty measuring the high-loss samples. In-band, removing the NDF effect brings the measured bandpasses into good agreement with the designed transmission, but the presence of the NDF makes it difficult to characterize the upper band edge and out-of-band transmission. We attempt to remove this effect as much as possible by subtracting out an exponential fit, as seen in Figure 5.13. This allows more definitive statements about the upper band edges, but still makes out-of-band leakage characterization difficult above certain frequencies.

The band edges are defined as the points where the normalized transmission is 0.05. The

definitions for band center and Dicke bandwidth are:

$$\nu_c = \frac{\int \nu S(\nu) d\nu}{\int S(\nu) d\nu} \tag{5.1}$$

$$\Delta\nu = \frac{(\int S(\nu) d\nu)^2}{\int S(\nu)^2 d\nu} \tag{5.2}$$

For a photon-noise-limited detector, it is critical that we do not observe too much emission from atmospheric lines. The atmospheric emission in these regions is much brighter than the corresponding CMB signal, and accidental sensitivity to the emission would cause our detectors to saturate, reducing the loop gain and thus increasing the contributions from other noise sources, as described in section 3.2. This is what allows us to set quantitative requirements on the spectral properties.

The in-band properties can be found in Table 5.3, along with the SO requirements where they exist. An example spectra with atmospheric and designed bandpasses can be seen in Figure 5.14. The band edges do not have explicit requirements and instead are phrased in terms of out-of-band leakage requirements. We are in compliance with all stated requirements except for the MF-2 bandwidth requirements. The incomplete nature of the coupling optics, error in the NDF correction, and the low optical efficiencies of the MF-2 detectors could all contribute to this, though the exact cause is unclear.

Table 5.3. Module-averaged values for band centers and bandwidths in both frequency bands. Each module measured is in compliance with SAT requirements, except for the MF-2 bandwidth requirements, which could be related to NDF uncertainties or reduced MF-2 efficiencies, a previously known effect in the detector modules.

Parameter	Min (GHz)	Typical (GHz)	Max (GHz)	Mv14 (GHz)	Mv18 (GHz)	Mv19 (GHz)
Band center MF-1	88.0	92.6	97.2	90.3	91.2	89.6
Band center MF-2	141.6	149.1	156.6	142.3	144.8	141.1
Bandwidth MF-1	33.1	—	—	34.4	37.4	33.1
Bandwidth MF-2	43.9	—	—	41.2	39.9	41.4

The out-of-band leakage requirements are written as integrated power in between frequencies ν_1 and ν_2 relative to the integrated power between the band edges ν_{lower} and ν_{upper}:

$$\frac{\text{out-of-band power}}{\text{in-band power}} = \frac{\int_{\nu_1}^{\nu_2} S(\nu) d\nu}{\int_{\nu_{\text{lower}}}^{\nu_{\text{upper}}} S(\nu) d\nu} \tag{5.3}$$

where $S(\nu)$ is the measured bandpass for a particular detector.

Due to the NDF, we cannot provide any constraining power above 145 GHz for the MF-1 band and above 180 GHz for the MF-2 band, which can be seen in Figure 5.15. For the regions we have sensitivity to, we are passing all leakage requirements, which can be seen in Table 5.4. Validation of the high-frequency leakage requirements, which could not be done with this FTS, is discussed in the next section.

5.7.2 Thick Grill Filters

Additional out-of-band leakage measurements can be performed by using a so-called thick grill filter, which acts as a high-pass filter for free-space electromagnetic radiation [61].

Experimental Setup

The same source, chopper, and aperture from the beam mapping measurements were used for the thick grill filter measurements. The source was running at 760 °C and chopped at 6 Hz. The source was positioned in the middle of the window to maximize the SNR for as many detectors as possible.

The filters were provided by collaborators at the University of Pennsylvania and were the same ones used for characterizing the optics tubes for the LATR at University of Chicago. We used two different filters, one with a 120 GHz cutoff to restrict the MF-1 band but transmit the MF-2 band, and one with a 190 GHz cutoff to restrict both detector bands. Photos of the filters can be seen in Figure 5.16. The cutoff frequency for the filter is set by the hole diameter, as described in [61], and given by

Table 5.4. Out-of-band leakage estimates. For all atmospheric windows where we have low enough uncertainty from NDF transmission, we are in compliance with SAT requirements.

Line	Min (GHz)	Max (GHz)	MF-1 Requirement	Mv14 MF-1	Mv18 MF-1	Mv19 MF-1
L1	51.4	68.8	1.0%	0.11%	0.11%	0.2%
L2	115.4	122.0	0.8%	0.7%	0.5%	0.6%
O1	21.7	30.3	1.0%	0.005%	0.002%	0.006%
O2	30.3	51.4	1.0%	0.005%	0.04%	0.09%
O3	68.8	115.4	—	—	—	—

Line	Min (GHz)	Max (GHz)	MF-2 Requirement	Mv14 MF-2	Mv18 MF-2	Mv19 MF-2
L1	51.4	68.8	0.4%	0.01%	0.01%	0.003%
L2	115.4	122.0	1.0%	0.6%	0.12%	0.7%
O1	21.7	30.3	1.0%	0.002%	0.001%	0.0003%
O2	30.3	51.4	1.0%	0.007%	0.006%	0.002%
O3	68.8	115.4	1.0%	0.17%	0.2%	0.07%

$$\nu_c = \frac{0.586}{d} \tag{5.4}$$

where d is the hole diameter. The two filters used have hole sizes of 1.5 mm and 0.905 mm, which correspond to the 120 and 190 GHz cutoffs.

Measurements

Three datasets were collected for each filter. In the first, the chopper and source were both turned on, but the aperture was covered with a piece of eccosorb. In the second, we removed the eccosorb but left the chopper and source on. In the third, we placed the thick grill filter in the aperture. Each dataset was 5 minutes long, and they were taken in close proximity to one another to ensure comparability.

The eccosorb-covered aperture dataset provided a baseline noise floor for each measurement. The ”out-of-band power” is the total power present at the chop frequency in the filtered measurement, while the ”in-band power” is the total power present at the chop frequency in the empty aperture measurement. This allows us to compute the analogous out-of-band leakage definition in equation 5.3.

The figure of merit here is the comparison between the effective noise floor defined by the dataset with no visible chopped source and the out-of-band leakage defined above. Due to the NDF attenuation increasing as frequency increases, we can only provide an upper-bound on this value, but we observe that all out-of-band transmission is at minimum consistent with no visible source. Constraints on out-of-band leakage found on other similar detectors [62] are compelling enough to consider this aspect of the SAT's optical performance validated.

5.8 Polarization Measurements

For polarization-sensitive instruments like the SAT, especially when we are concerned with extremely weak signals, one of the most important qualities is that we do not accidentally

Table 5.5. Upper bounds on high-frequency out-of-band leakage for each measurement done with the two thick grill filters, respectively. The upper bound from baseline no-chop sets a noise floor from no visible chop in the detector signal, and the fractional leakage is computed as the ratio of the power present at the 6 Hz chop with and without the thick grill filter, following the definition in equation 5.3.

	Mv14	Mv18	Mv19	Mv22	Mv6	Mv9
Upper bound from baseline no-chop	1.3%	1%	2.4%	0.4%	0.4%	3.6%
Fractional leakage above 120 GHz	1.3%	1.4%	2.4%	1%	1%	5.4%
Upper bound from baseline no-chop	1.2%	2%	9.7%	2.8%	1.6%	2.7%
Fractional leakage above 190 GHz	1.2%	2.2%	9.9%	2.8%	1.6%	2.7%

reject polarized signals. Viewed another way, if a certain polarized input is not efficiently transferred to and measured by the detectors, it can confuse the analysis and, at best, is a direct hit to sensitivity, because it requires more observing hours to generate the same level of sensitivity.

This can be broadly separated into two different terms: polarization efficiency and cross-polarization. Polarization efficiency is how much of an incoming polarized signal is measured, with 0% being we observe zero signal on a detector from a source polarized along the same direction and 100% being same measured amplitude as incoming amplitude. Cross-polarization, in this context, refers to how much observed polarized signal is measured on a detector orthogonal to an incoming signal. In other words, how much spurious polarized signal is observed when an orthogonal signal is introduced.

In the SAT, we measured total optical efficiency and used that in concert with the cross-polarization measurements to characterize the polarized efficiency, the results of which can be found in [55].

Experimental Setup

To generate the incident polarized signal, we use the same source and chopper as the beam-mapping setup. A >99% efficient polarizing grid is installed between the source and the aperture, such that any signal observed through the aperture is polarized perpendicular to the

grid direction, and modulated at 6 Hz. The polarized source is mounted on the test equipment frame and positioned over the middle of the window to maximize SNR for the maximal number of detectors.

The polarizing grid can be stepped with sub-degree accuracy to different positions to change the polarization angle of the source. There is no absolute reference for the grid, but it is kept consistent between all measurements, such that there is no relative phase difference between any successive trials. For the purposes of the reported measurements, 0° refers to the grid being aligned parallel to the long axis of the SAT.

The position of the HWP will rotate the incoming polarization angle by an unknown amount, since the position of the HWP is not known once it stops rotating. The effect on the measured signal is a phase shift of the detector's recorded sinusoidal response dependent on the relative angle between the HWP angle and the detector's polarization angle. However, the phase shift does not matter for a measurement of the cross-polarization, where the only important parameter to extract is the relative size of a response to the grid when it is rotated 90° relative to the angle of peak response. Thus, for these measurements, the HWP is held stationary and ignored in analysis.

Measurements

Starting from 0°, the grid is stepped in 5° steps over one full grid rotation. This corresponds to two periods of polarized response in the detector. Data is recorded continuously during this period, waiting at each grid step for one minute, while the source is chopped at 6 Hz.

To process the timestreams, we load the detector data, detrend and high-pass filter the data, and then demodulate at 6 Hz. At each step of the grid, we bin the detector's mean signal and record it relative to the current grid position. Since each detector sees a different amplitude signal, dependent on its focal plane position, we then peak-normalize the resulting signal. For a well-behaved detector, the resultant signal should look sinusoidal, like in Figure 5.19.

Afterwards, we fit a periodic function of the form

$$a\sin(2\pi fx)+b\cos(2\pi fx)+c \tag{5.5}$$

which is mathematically equivalent to

$$A\sin(2\pi fx+\phi)+c \tag{5.6}$$

when

$$A=\sqrt{a^2+b^2}, \qquad \phi=\arctan\left(\frac{b}{a}\right). \tag{5.7}$$

The cross-polarization for a particular detector is then defined as the minimum of the curve, $c-A$, which should occur 90° from the peaks of the curve. The values reported here are $1-2A$, which is approximately correct for this signal-dominated peak-normalized data. Histograms for each measured UFM are shown in Figure 5.20. As shown, the cross-polarization is much higher than the required 1%. This result is consistent with other measurements of similar modules in other test cryostats, namely measurements of the MF detectors in the LATR Optics Tube Tester at University of Chicago [47], [62]. Further measurements will be performed at the observing site with far-field polarizing sources to determine whether this is an effect of near-field lab measurements or a property intrinsic to the detector modules.

While the lower values shown in the histograms in Figure 5.20 are well above the requirement threshold, it is worth highlighting that the larger values (>10%) are likely biased due to lower SNR on these channels, especially in the MF-2 detector band. This effect is highlighted in Figure 5.21, where the lower SNR resulting from the reduced NDF transmission at higher frequency and dimmer apparent signal further off-axis contributes to poorer measurements of the cross-polarization signal.

5.9 Summary

In this section, we have presented the in-lab validation of the SAT and its optical system with a fully populated focal plane. This includes validation of the detector properties, as well as a description of the optical tests I performed during validation: beam measurements, spectral measurements, and polarization measurements. In the beam and spectral measurements, the SAT was shown to meet all required benchmarks for deployment of the cryogenic receiver, after completion of the in-lab testing program. The polarization measurements demonstrated a cross-polarization leakage above our required benchmark, but consistent with measurements made at other institutions with similar modules, which yields increased confidence that the SAT is not inducing additional polarization leakage. As a result, we have completed in-lab validation of the SAT and will move on to the next phase, shipping to the observation site and proceeding with site commissioning before beginning science observations.

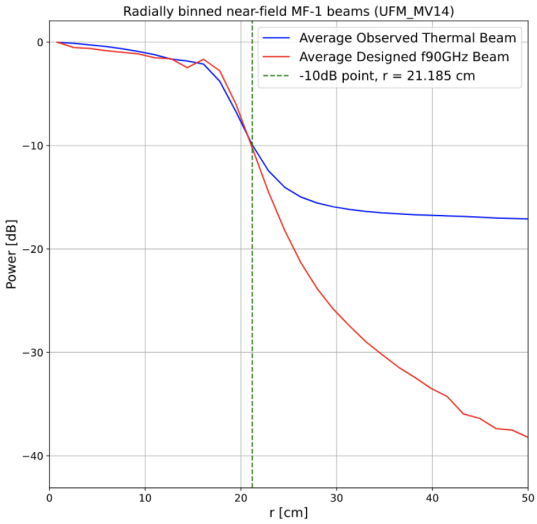

(a) MF-1 radial beam profile

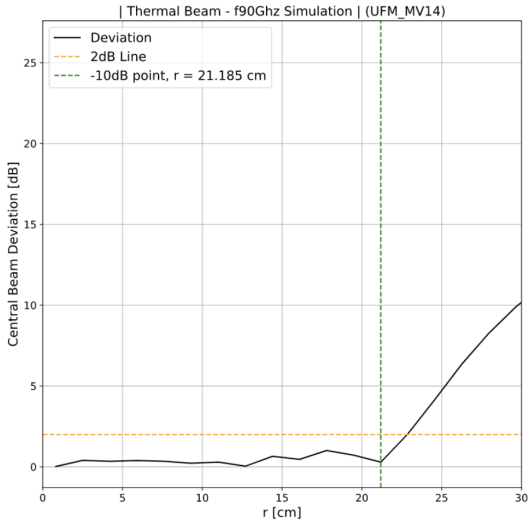

(b) MF-1 beam deviation

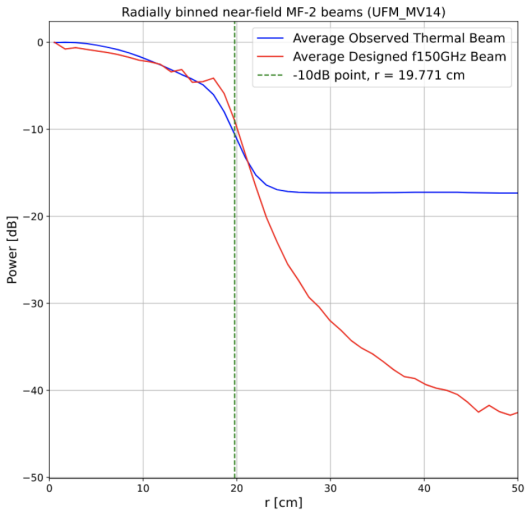

(c) MF-2 radial beam profile

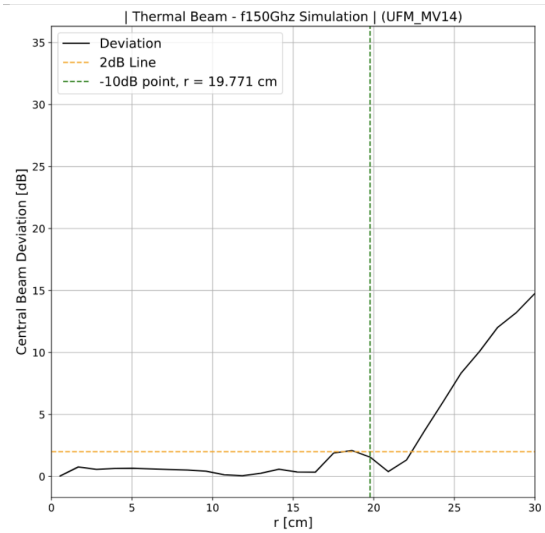

(d) MF-2 beam deviation

Figure 5.9. The figures in the left column are the radial beam profiles overplotted with the simulated beam profiles, as in Figure 5.8. On the right column is shown the difference of these two profiles. For SO, we require that the near-field beam deviation up to -10 dB of the normalized beam profile is $<$2 dB in both frequency bands, which is demonstrated by our measurements of the beam profiles in the central UFM.

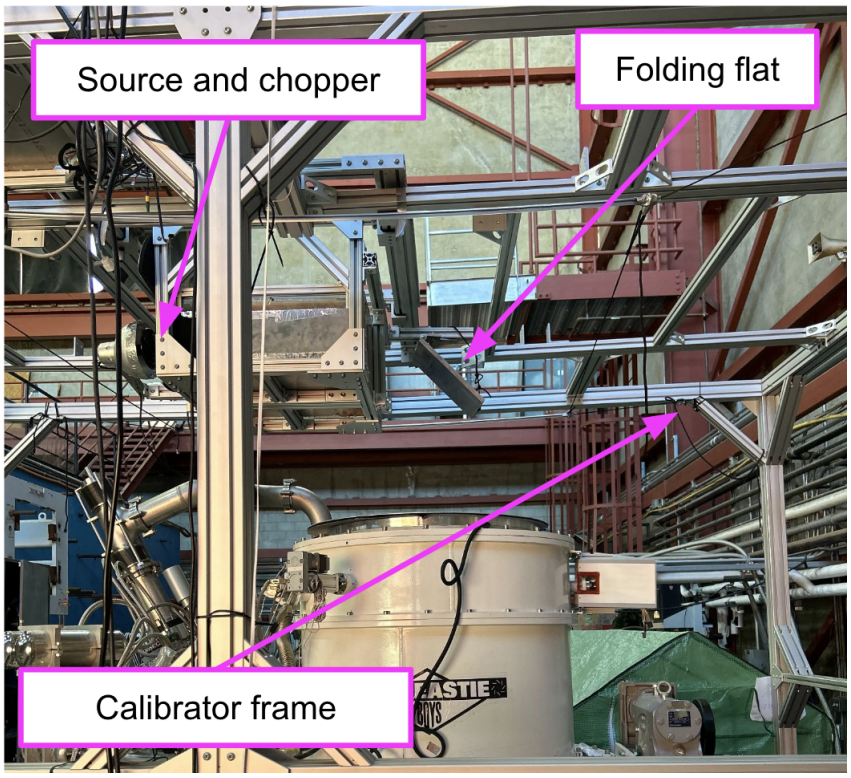

Figure 5.10. FTS test equipment installed on the mounting frame above the SAT. Pictured are the thermal source and chopper, the FTS itself, and the folding flat used to redirect the FTS output into the SAT and couple to various detector modules.

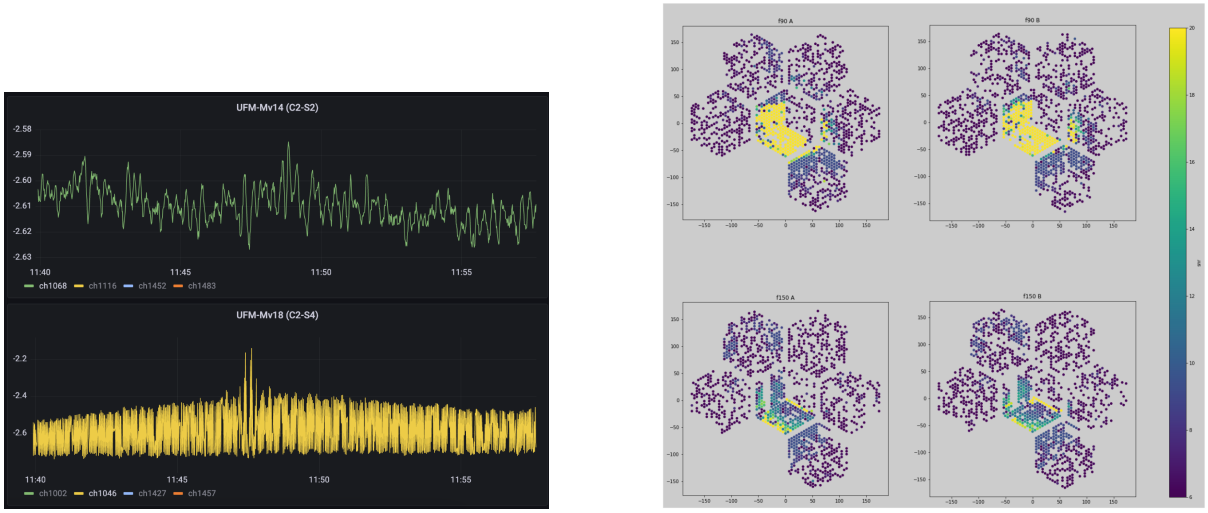

(a) **(b)**

Figure 5.11. Detector timestream data during FTS scans. (Left): Livestreaming, downsampled detector timestreams taken while adjusting the position of the FTS and the folding flat. The green timestream is a detector that does not see a chopped signal, while the yellow timestream is a detector in another UFM that is able to observe the chopped signal, indicating that an FTS measurement can be taken illuminating this particular UFM. (Right): Signal-to-noise ratio as a function of detector position for a particular FTS scan. The top row are the 90 GHz detectors, while the bottom row corresponds to the 150 GHz detectors. Only a single UFM is illuminated at substantial SNR in a particular FTS scan, requiring re-positioning of the FTS and mirror in between each measurement. The SNR is much higher in the MF-1 band because there is increased attenuation of the signal due to the NDF in the MF-2 band.

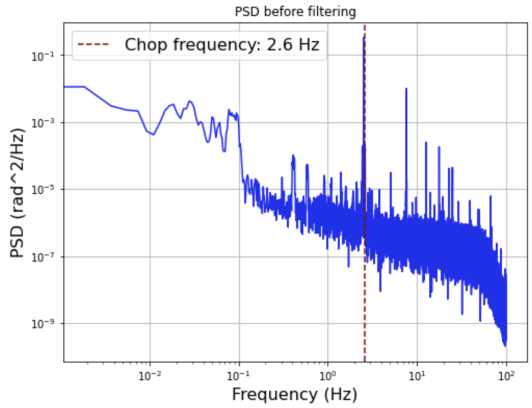

(a) Unfiltered PSD

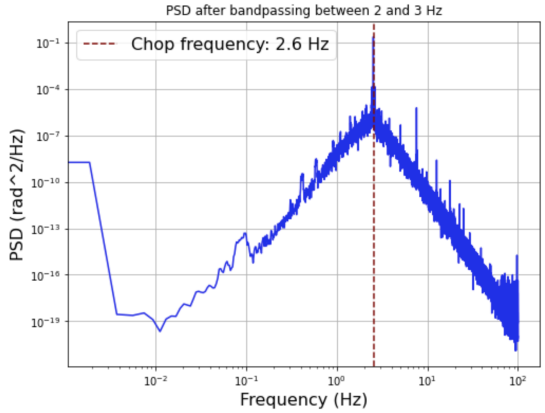

(b) PSD after bandpass filtering between 2 and 3 Hz

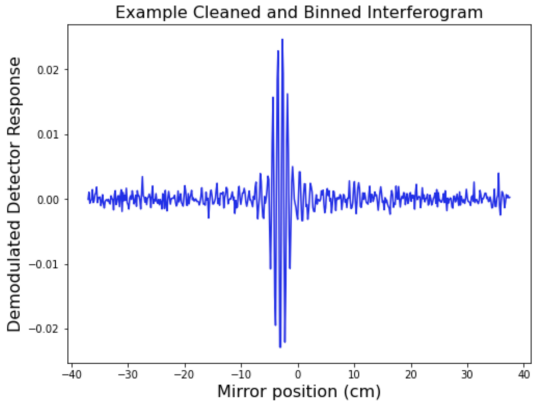

(c) Cleaned and binned interferogram

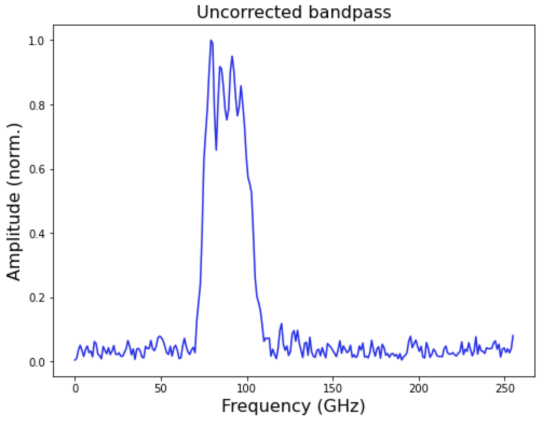

(d) Example Bandpass for a 90 GHz detector

Figure 5.12. Sample plots from FTS data processing for a particular detector channel.

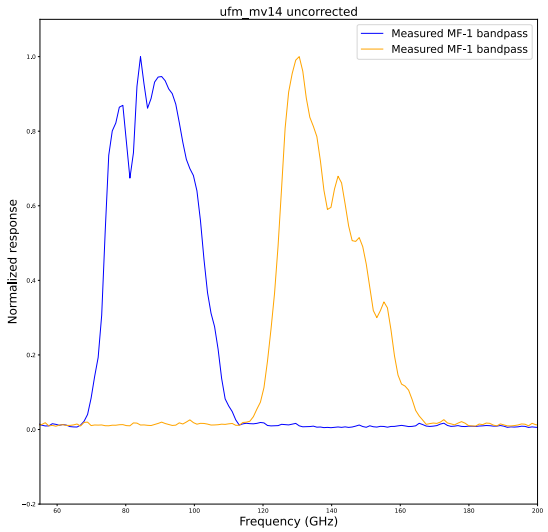

(a) No correction applied

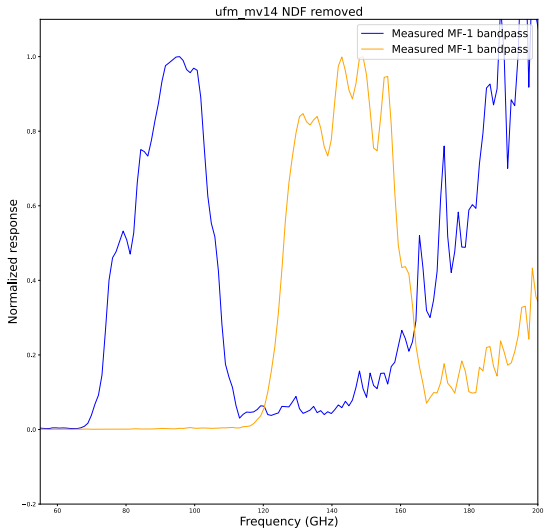

(b) NDF transmission removed

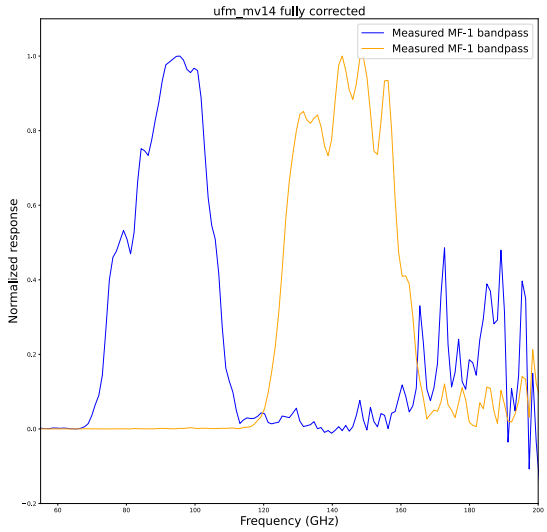

(c) Exponential increase at higher frequencies removed

Figure 5.13. Illustrated correction process for removing the NDF spectral dependence from the measured detector bandpasses. The effect is especially noticeable in the MF-2 bandpass in 5.13a. Once the NDF tranmission is removed, the small transmission values cause a non-physical, exponential increase to appear in the high-frequency range of the spectrum where it is noise-dominated, as seen in 5.13b. In order to remove this, we subtract an exponential to suppress the effect close to the spectrum, in order to enable reconstruction of the upper band edges of the individual bandpasses. The nature of the increase limits our ability to characterize out-of-band leakage at higher frequencies from these in-lab measurements.

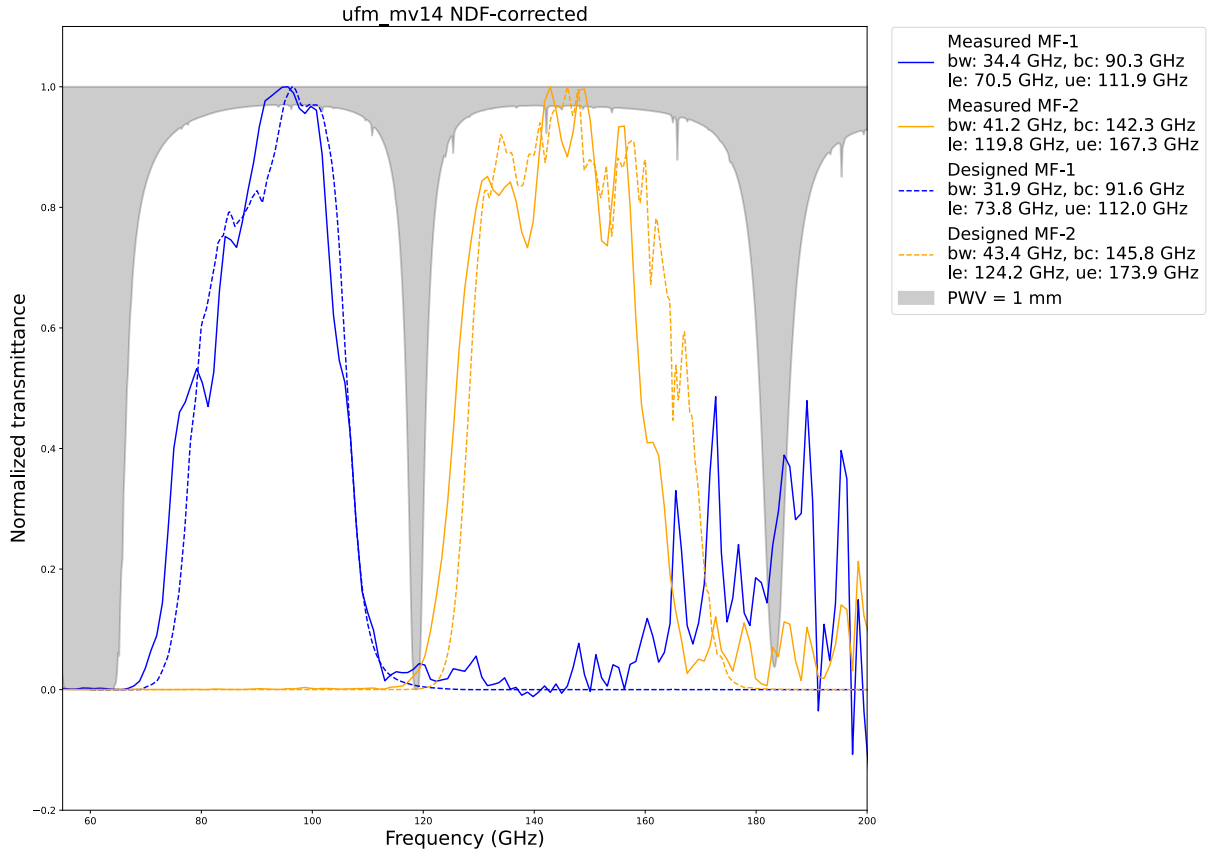

Figure 5.14. Module-averaged spectra from the central UFM, overplotted with the designed end-to-end bandpasses for the SAT, as well as the transmittance of the atmosphere simulated with one mm of PWV. Even though the upper band edges are difficult to characterize due to the presence of the NDF, and the MF-2 bandwidth is slightly below expectation, we are well within the required atmospheric windows, and meet requirements for deployment.

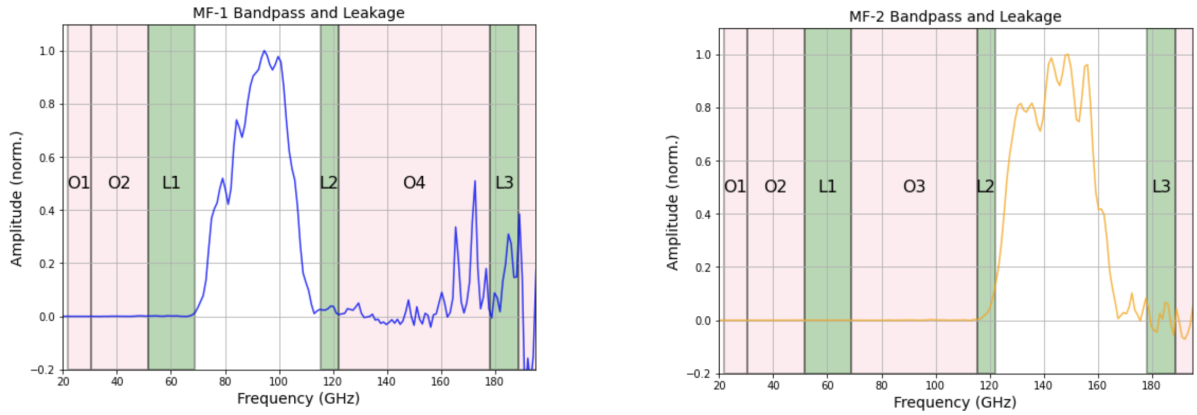

(a) MF-1 band

(b) MF-2 band

Figure 5.15. Module-averaged bandpasses overplotted with the atmospheric leakage windows. The increased uncertainty in transmission due to the NDF correction can be observed here, which is the main limiting factor in characterizing these properties via in-lab measurements.

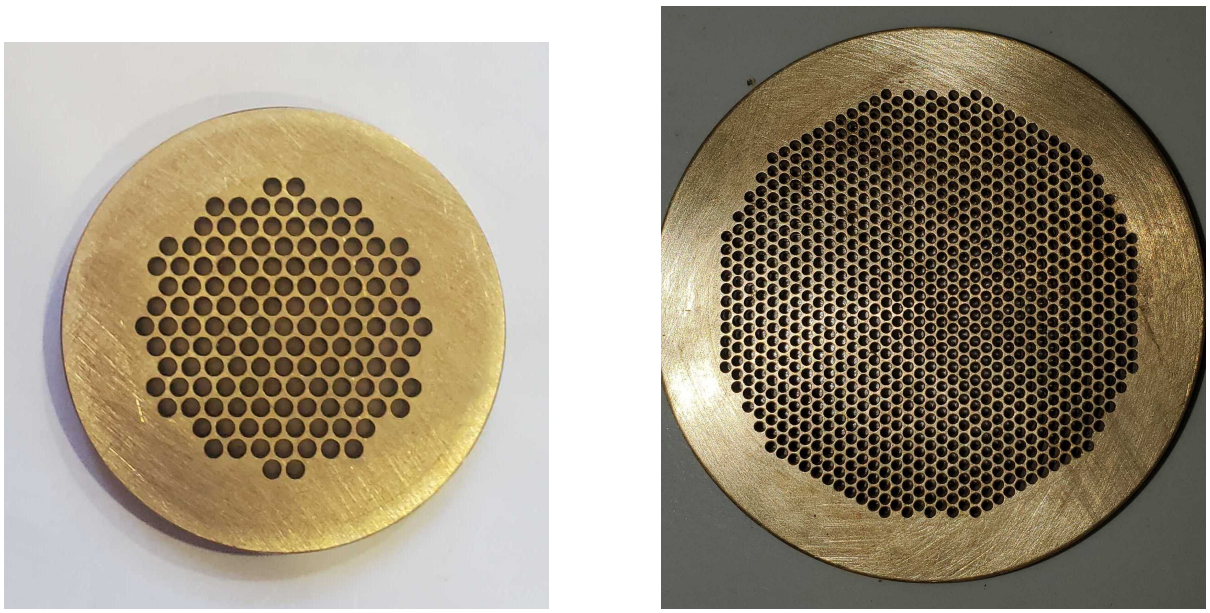

(a) 120 GHz cutoff

(b) 190 GHz cutoff

Figure 5.16. Thick grill filters used for placing limits on high-frequency out-of-band leakage. The hole diameter and spacing determines the cutoff frequency for transmission, causing it to act as a high-pass filter [61].

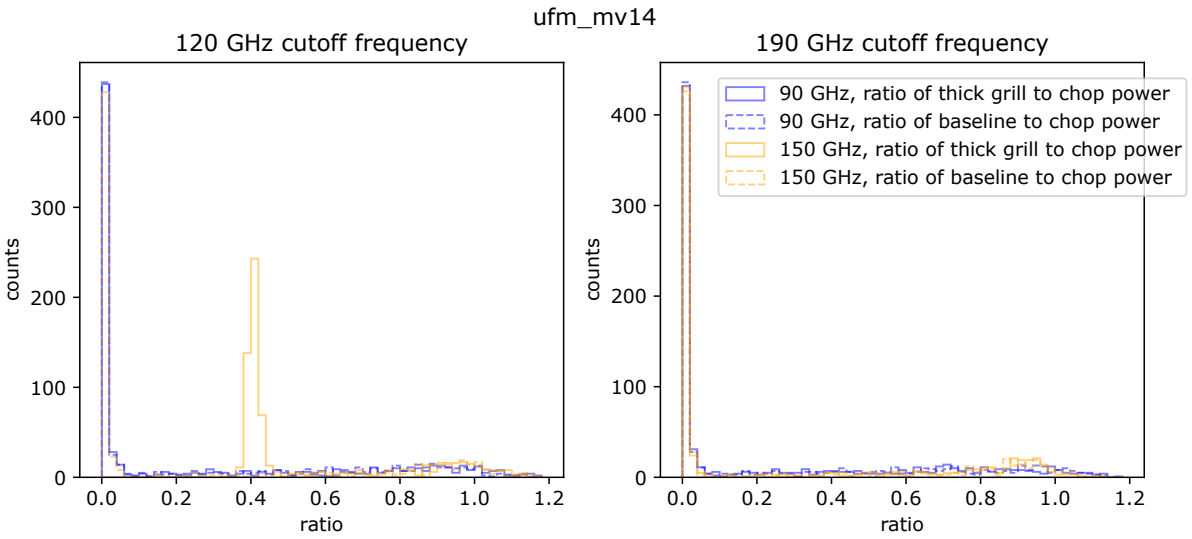

Figure 5.17. The ratio of out-of-band leakage to in-band power. This is measured as the power present near the 6 Hz chop frequency with and without the thick grill filter in place, compared to the power present at 6 Hz when Eccosorb obscures the chop from the detectors. On the left is when the 120 GHz cutoff filter is used, compared to the 190 GHz filter on the right. As expected, the MF-2 band still observes power transmitted above 120 GHz, but none above 190 GHz, while the MF-1 band observes no power transmitted with either filter installed.

Figure 5.18. Stepped, polarizing grid installed in front of the thermal source and chopper. Not present in this picture: the 3.8-cm aperture to restrict reflections and systematics from appearing in the observed detector signal.

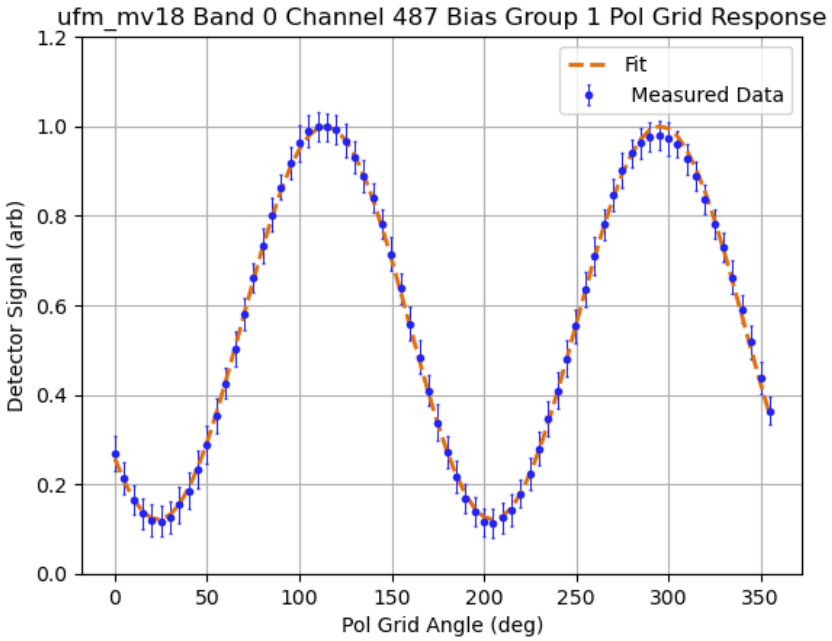

Figure 5.19. An example of a processed detector response as a function of polarizing grid angle. A sinusoidal wave is fit to the detector signal, which is then used to extract the cross-polarization observed, which is defined as the size of the signal when the grid is orthogonal to the maximum-amplitude signal.

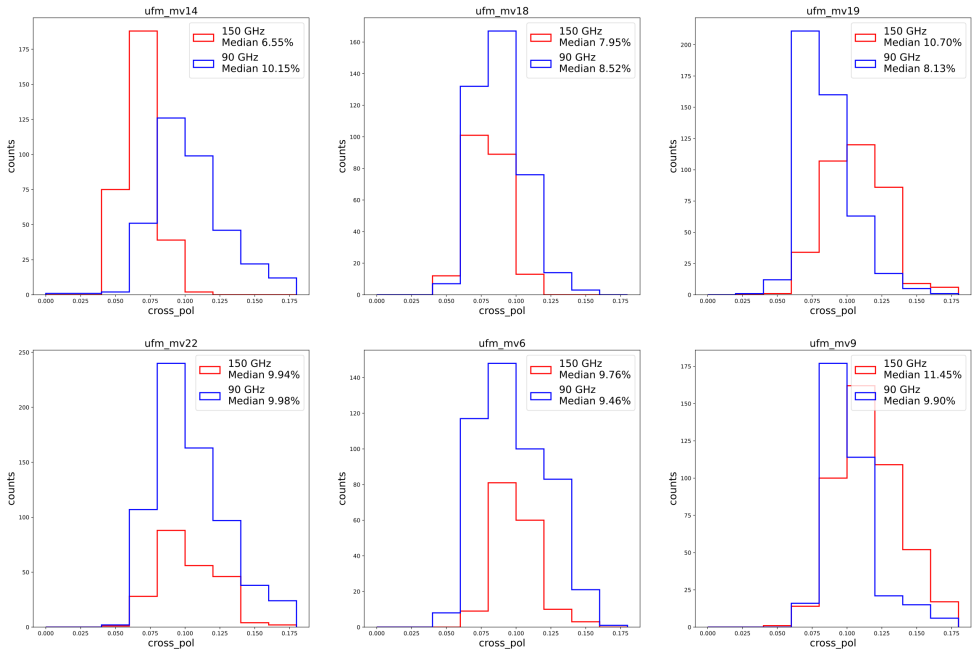

Figure 5.20. Cross-polarization distribution as a function of module and detector band.

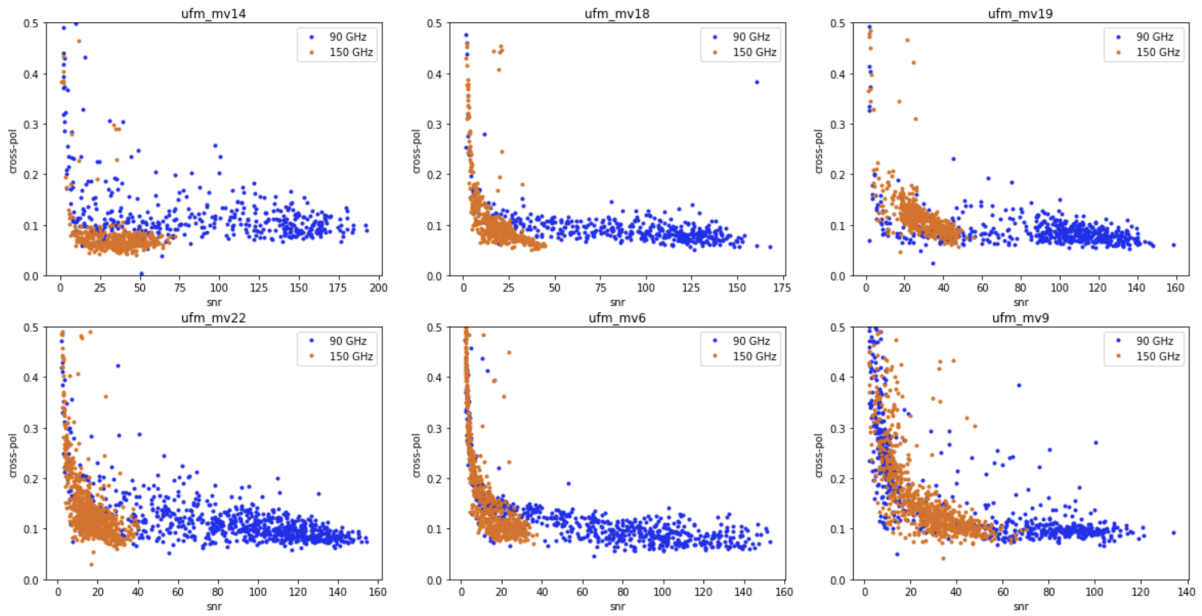

Figure 5.21. Demonstration of the noise bias present for certain high cross-polarization channels, particularly in the 150 GHz band. There is still a high minimum, average value for cross-polarization across all detectors, but the higher values are not likely to be real. Instead, low SNR due to increased NDF attenuation at 150 GHz and poorer off-axis illumination likely contribute to the higher values in the 150 GHz band.

Chapter 6

Detector Software Development

The adoption of a new detector readout scheme, μmux, and the SMuRF electronics system requires new control and analysis software to implement the detector characterization methods described in Chapter 3. In addition, for a project the scale of SO producing large data volumes, organized integration into the complex software stack used for processing data in the time-domain is a critical step. This chapter outlines development of software tools for all three key steps of detector calibration and testing: data acquisition and analysis of detector parameters, loading detector timestreams, and the application of calibration metadata to streamed detector data.

6.1 Simons Observatory Detector Library

The Simons Observatory Detector Library (`sodetlib`[1]) is a library we developed to implement common detector operations and analysis tools. This includes, but is not limited to, the techniques described in section 3.3.

Given that SO is employing a novel readout technology, with new electronics and control that have not been deployed at full scale before, we require a novel implementation of the common detector characterization methods. This requires development of new data acquisition modes compatible with the control provided by the SMuRF electronics and the `pysmurf`[2]

[1] https://github.com/simonsobs/sodetlib
[2] https://github.com/slaclab/pysmurf

software, along with analysis code creates outputs compatible with SO's extensive software stack.

Implementation of `sodetlib` and its detector characterization tools was done in the detector testbed described in chapter 4. This included early testing on single-detector systems and continued to full array-scale testing and development. The SAT, with the fully integrated focal plane described in chapter 5, was then used to validate the performance of the full software package when operating on multiple UFMs simultaneously.

`sodetlib` is intended to provide two main use cases: in-lab validation measurements and detector calibration operations during science observations at the Chilean site. The former was demonstrated in the detector testbed here at UCSD and in SAT-1, described in chapter 5. All the detector data produced in the final in-lab testing run of the SAT was taken using `sodetlib` tools, and was critical for informing continued development.

The final run of the SAT also provided useful inputs for the latter, since it was the first full-scale integration run for an SO instrument. The volume of data produced in the SAT in-lab testing program provided testing grounds for the integration of `sodetlib` outputs into the SO data processing pipeline, which will be described in more detail in section 6.3.

6.1.1 Example Outputs

All of the detector calibration operations produce stored outputs, saved as dictionaries in `.npy` files. Figures 6.1, 6.2, and 6.3 show example plots generated by `sodetlib`. All of these examples were generated in either the UCSD detector testbed or the SAT.

6.2 G3tSmurf

The detector timestreams and the accompanying metadata produced by SMuRF are complicated and non-trivial to sort through by hand. As such, loading the datastreams presents a meaningful software challenge. We developed the `G3tSmurf` module in order to provide a schema to organize the volume of SMuRF data as well as provide data loading tools for in-lab

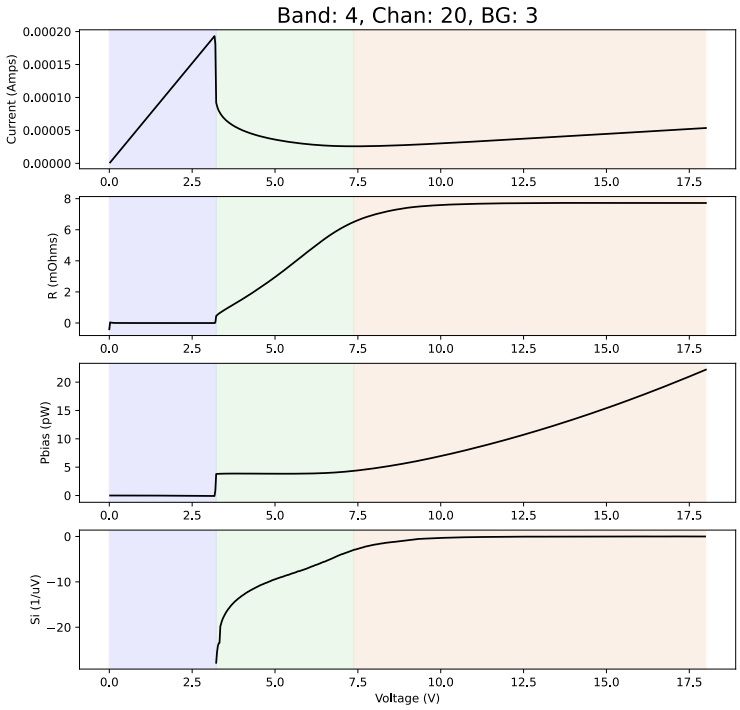

Figure 6.1. Example IV curves and associated parameters measured and produced by `sodetlib`. Also plotted are the other TES parameters vs. voltage, R_{TES}, P_{bias}, and S_I. The colored regions show the fitted overbiased, in-transition, and superconducting regions.

testing and low-level users involved in site commissioning.

As with `sodetlib`, I have been heavily involved in the development and testing of `G3tSmurf`. This has been directed especially in its scaling to handle full focal-plane data from SAT-1 in-lab data and the identification and integration of `sodetlib` detector calibration operations.

There are four main problems that need to be addressed in order to properly load detector data produced by SMuRF:

1. Identifying which files stored on disk correspond to which detector observations

2. Organization of the `.g3`[3] files that detector timestreams are stored in is complicated, and

[3]https://github.com/simonsobs/so3g

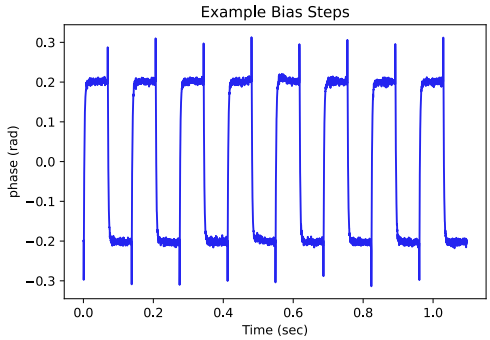

(a) Bias steps.

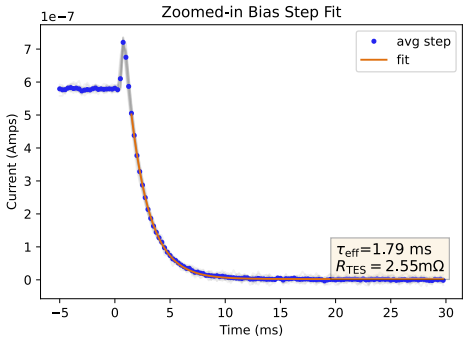

(b) Stacked and fitted bias steps.

Figure 6.2. Example bias steps taken and measured by `sodetlib`. On the left are bias steps taken on a single detector in-transition. The smaller spikes are the result of the electrical time constant, and the slower relaxation time is from the modified time constant due to electrothermal feedback. On the right, the steps are stacked and then the time constant τ_{eff} is fitted and provided.

requires expert knowledge to parse correctly

3. Element-wise comparison of datastreams do not map cleanly between distinct observations, because of the way SMuRF assigns each detector-resonator pair to a readout channel

4. Connecting raw timestreams to the SO timestream processing tools provided by `sotodlib`[4], SO's library for doing time-domain data analysis

`sodetlib` registers moments of continuous detector streaming as discrete actions, which provides a solution to the first problem. In addition, SMuRF itself provides the metadata necessary to address the third item. However, identifying all the required metadata and actions when trying to load specific observations is difficult and impractical on-the-fly, which points to the need for a system to relate all the stored metadata. The other two problems also indicate the need for a more user-friendly implementation of data-loading mechanisms, developed by experts in the low-level data storage and readout technology.

`G3tSmurf`[5] is best understood as a database system with a set of relationally linked tables. A list of the tables and a brief corresponding description of each can be found in Table 6.1, and

[4]https://github.com/simonsobs/sotodlib
[5]https://sotodlib.readthedocs.io/en/latest/g3tsmurf.html

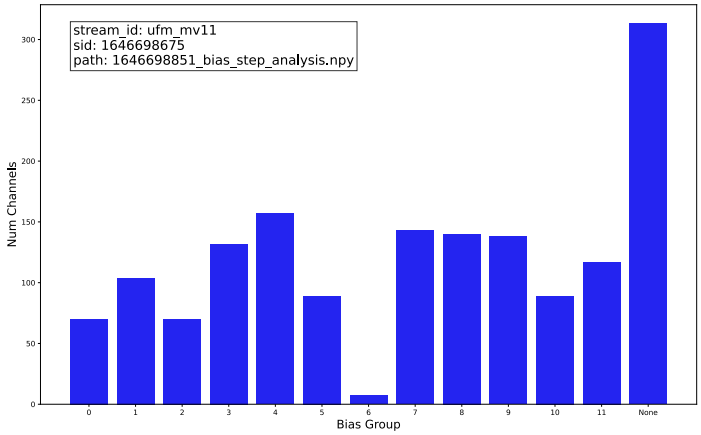

Figure 6.3. Bias group map generated by `sodetlib`. Bias steps are performed on each individual bias line, and each detector response is correlated with the commanded steps to compare which detectors are connected to which bias groups. Detectors that don't respond to any bias lines are flagged as None.

are represented visually in Figure 6.4. These tables and their relationships form the core of the required information to load detector observations in a complete and context-filled manner.

`G3tSmurf` implementation followed a similar trajectory to `sodetlib`. Initial development took place on smaller systems like the UCSD detector testbed (Chapter 4), and was further worked on in early testing runs of the SAT (Chapter 5) and the LATR Tester at University of Chicago [47]. The final full-scale, multi-UFM demonstration of `G3tSmurf` was done on the SAT focal plane in the test run described in Chapter 5.

`G3tSmurf` has not only provided a crucial tool for in-lab testing, and planned use in site commissioning of the instruments, but is also a major part of the data flow pipeline for SO. The `G3tSmurf` database tables form the foundation for the relational databases that will be in place to organize the final data used for science-grade analysis. Development during the final run of the SAT provided a robust test case for such full-scale observations.

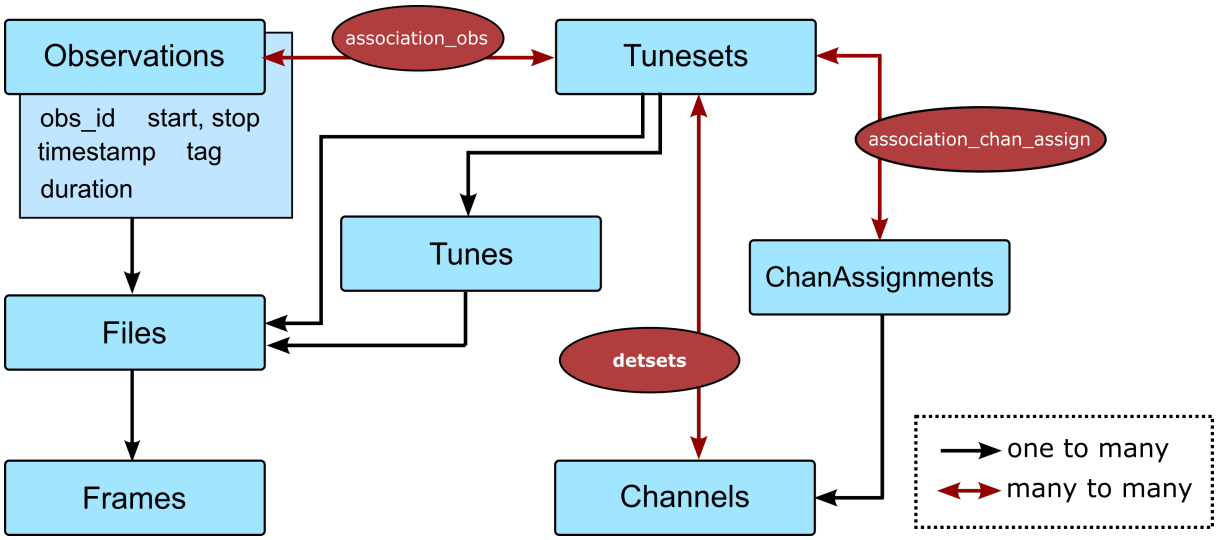

Figure 6.4. Flow chart describing the relationships between the tables in the `G3tSmurf` database. Each of these tables is required to properly reference detector timestreams with the SMuRF metadata that describes the datastream.

6.3 Detector Metadata Calibration Databases

The detector parameters obtained from `sodetlib` measurements are an important part of the analysis pipelines for processing the raw detector data into a useful scientific product. For example, the time constant response of the detectors must be deconvolved from the measured data, and we can use the bias step measurements to provide the necessary input. Similarly, the measured TES resistance and responsivities can be used to identify which detector channels are well behaved and likely to provide meaningful results.

The `Context`[6] system implemented in `sotodlib` provides the framework for including associated metadata when loading observations. However, it requires any metadata loaded in this manner to be stored in a specific format. For each individual piece of metadata, a table with the appropriate values is stored as an HDF5 dataset called a Calibration Database (`CalDb`, for short). Each dataset must also have a corresponding Metadata Index entry, detailing the file where the dataset is stored, the name of the dataset, and a way to match a particular dataset with the observation being loaded.

[6] https://sotodlib.readthedocs.io/en/latest/context.html

Table 6.1. `G3tSmurf` Table Descriptions

Table	Description
Observations	Times of continuous detector readout for individual UFMs. Observations also contain descriptive tags.
Files	The `.g3` files that make up a particular observation.
Frames	Indexing info for accessing `.g3` files.
Tunes	Files produced by SMuRF containing information about the tracked resonators for a particular observation.
TuneSets	The tunefiles that define the channel mapping for a particular set of observations. Each TuneSet is a Tune, but not each Tune is a TuneSet.
ChanAssignments	The assignments referenced in the TuneSet that correlates resonator frequencies with a reported channel number from SMuRF.
Channels	All detectors that were streaming for a particular observation.

The site-like configuration of the final SAT in-lab test run provided a large dataset of detector calibration outputs, along with many separate streamed observations. While the storage of detector metadata in this manner was not necessary for in-lab testing, we still used the in-lab data to develop the pipeline scripts for full-scale operations at the Chilean site.

The `.npy` output files from `sodetlib` contain all the required information but are not stored in a format compatible with the metadata system in the SO software stack. The general pipeline for generating the `Context`-compatible datasets and corresponding Metadata Index entries from the `sodetlib` output files is as follows:

1. Identify any non-indexed detector calibrations.
2. For each one, extract the relevant calculated parameters, documented in Table 6.2. The readout channels for each are pulled from the corresponding `TuneSet` in the `G3tSmurf`

database.

3. Store the per-detector parameters as an HDF5 dataset, and save it in the appropriate `CalDb`.

4. Identify the range of times for which the detector calibration is valid. By default, this stretches from the time it was taken until it is replaced by a new calibration.

5. Store the dataset name, file name, and valid time range as an entry in the corresponding Metadata Index.

This developed pipeline runs automatically and checks for any new `sodetlib` calibrations saved to disk to provide the corresponding `CalDb`. When an observation is loaded and the detector calibration metadata is requested, the system locates the appropriate entry in the Metadata Index and loads the data from the `CalDb` into the observation, provided the readout channel names in the observation match the entries in the `CalDb`. Because the calibration is measured asynchronously from the observation datastream, this is not necessarily true, since a new readout tune could be applied in the intervening time.

The pipeline described here was developed using SAT-1 data from the final test run, using data from a full focal plane.

Table 6.2. SMuRF `CalDb` Contents. Each `CalDb` contains any information necessary to use the derived TES parameters, or to determine if channels from a particular observation are usable or not.

Type	Information included
IV Curves	Readout Channel, R_n, P_{sat}, S_I @ $R_{frac} = 0.5$
Bias Steps	Readout Channel, τ_{eff}, S_I, R_{TES}, R_n from IV, V_{bias}
Bias Group Maps	Readout Channel, Assigned Bias Group

6.4 Future Outlook

The SAT has completed its final validation run and has been packed and shipped to the observation site in Chile. The platforms, which provide pointing and scanning capability in azimuth, elevation, and boresight rotation, are installed and have been commissioned. After installation of the SAT on the platform, commissioning will immediately follow. The software developed in this chapter based on in-lab testing at the UCSD detector testbed and the SAT, including `sodetlib`, `G3tSmurf`, and the detector `CalDbs`, will be used to complete the commissioning process throughout late 2023.

Following commissioning, full-scale science observations will then commence. All of the tools will also be applied to the full science pipeline, where detector timestreams are processed into sky maps and then used to extract angular power spectra and cosmological parameters.

Appendix A

Detector Testbed Optical Coupling Design

To reduce systematic errors when performing spectral measurements with a Fourier Transform Spectrometer (FTS), it is preferred to fill as much of the detector beam as possible. A simplified description of the systematic effect can be seen in [53], and goes as follows. For a detector with effective area A_e and a source with frequency-dependent intensity $S(\nu)$, the total measured power as a function of frequency is

$$P(\nu) = \frac{1}{2}\int_{4\pi} A_e(\theta,\phi)S(\nu,\theta,\phi)d\Omega. \tag{A.1}$$

For a single-moded antenna, like those used by SO, $A_e \propto \lambda^2$, and for a beam-filling blackbody source in the Rayleigh-Jeans limit, $S(\nu,\theta,\phi) = B(\nu) = \frac{2kT}{\lambda^2}$. In this case, the power measured by the detector is simply

$$P(\nu) = kT, \tag{A.2}$$

which is independent of frequency. If the source is not beam-filling, the directional dependence in $S(\nu,\theta,\phi)$ generates a frequency dependence in the measured power, which is a systematic effect that isn't considered a real contribution to the bandpass for the measured detector.

In practice, understanding these systematics is complicated and difficult to calibrate. The effect is typically seen as a fringing effect inside the bandpass [52], and does not effect the measured band edges. The simplest tactic for mitigating these systematics is to design an optical

coupling that is highly efficient and fills as much of the detector beams as possible.

The FTS described in chapter 4 for use in the optical testbed was originally designed based on the optical design for the POLARBEAR cryogenic receiver [52]. In order to adapt it for use in the optical testbed, we designed a new optical coupling system.

The design must satisfy requirements related to the SO beam size, as well as function within the physical constraints of the lab space where testing is taking place. Because the optical testbed is also used for detector beam measurements, there is no installed aperture stop. Thus, we require that the optical coupling is able to couple to a 17° half width at half maximum (HWHM) beam, which is the angular size of the SAT aperture stop.

The testbed is installed inside a shielded RF room, which mitigates unwanted electromagnetic interference. This room, along with the mounting frame of the cryostat, puts a number of physical constraints on the overall size of the system. A CAD rendering of the system and a picture of the FTS inside the RF room can be seen in Figure A.1.

The original FTS design has an output parabolic mirror with a focus near the output of the FTS enclosure. In order to focus the FTS output onto the detector plane, we designed an off-axis elliptical mirror with F1 = 508 mm and F2 = 406.4 mm and a $\sim$380 mm diameter. The diameter was chosen to be large enough to capture the full output of the FTS.

The original design of the output parabolic mirror in the FTS is too slow to be compatible with the strict space constraints in the RF room, so a new mirror was fabricated. The mirror is an off-axis parabolic mirror with a focal length of 125 mm and a 200 mm clear collimated aperture. In order to be compatible with the newly placed focus, the output polarizer was also moved inside the FTS so it would not truncate the output. We also widened the output on the FTS enclosure itself to reduce truncation.

A ray trace of the system with measurements in millimeters can be seen in Figure A.2, as well as the same ray trace with CAD renderings of the mirrors overlaid.

The output mirror is installed and aligned with the rest of the optical elements of the FTS using the same laser alignment method used to align all the original components, where the

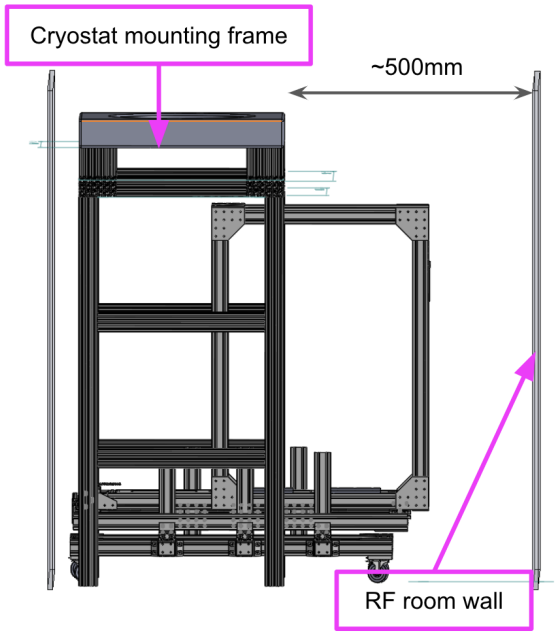

(a) CAD rendering of the RF room and FTS mounting frame.

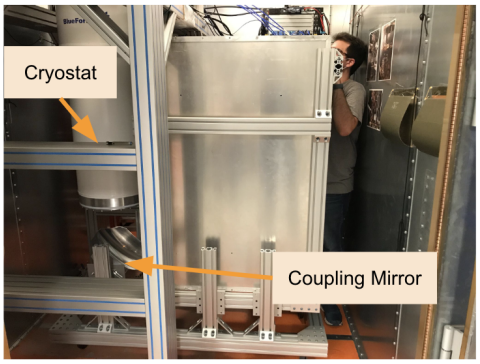

(b) Photo of the FTS and mount inside the RF room.

Figure A.1. The RF room where the optical testbed is installed creates a strong physical constraint on the size of the FTS and optical coupling system.

location of the expected focus is confirmed. The elliptical mirror is then installed in its nominal location relative to the measured focus of the FTS. The position and angle of the mirror can be adjusted using mounting brackets on the FTS frame.

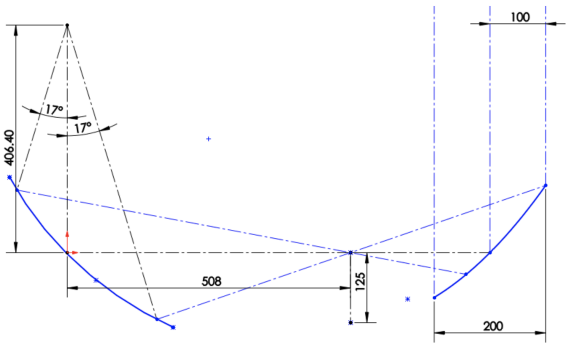

(a) Ray trace of coupling mirror system with dimensions. The mirror on the right replaces the previous FTS output mirror.

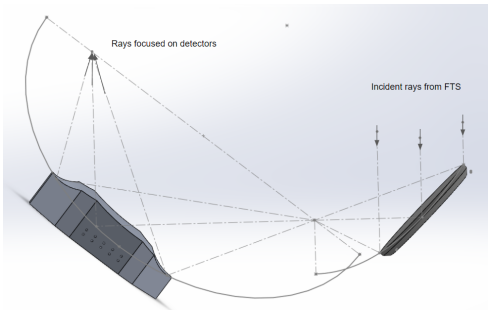

(b) Rendered image of mirrors including ray trace.

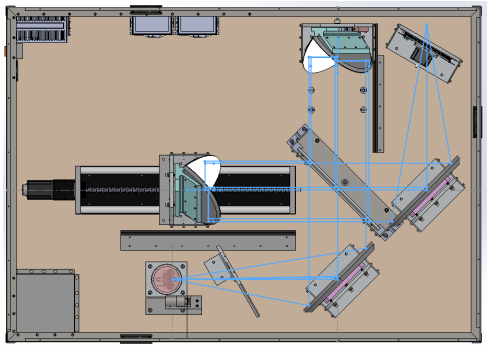

(c) CAD schematic of the original FTS design, with a ray trace highlighted. The mirror furthest to the right was replaced with the new parabolic mirror, and the polarizer in the upper right was moved closer to the output mirror.

Figure A.2. Ray traces for the FTS coupling mirror systems. The original FTS design and optical design is done by Fred Matsuda, and described in [52]. The ray trace for the altered output parabolic mirror and elliptical coupling mirror is also shown.

Bibliography

[1] Scott Dodelson. *Modern Cosmology*. Academic Press, Elsevier Science, 2003.

[2] Planck Collaboration, Aghanim, N., Akrami, Y., Ashdown, M., Aumont, J., Baccigalupi, C., Ballardini, M., Banday, A. J., Barreiro, R. B., Bartolo, N., Basak, S., Battye, R., Benabed, K., Bernard, J.-P., Bersanelli, M., Bielewicz, P., Bock, J. J., Bond, J. R., Borrill, J., Bouchet, F. R., Boulanger, F., Bucher, M., Burigana, C., Butler, R. C., Calabrese, E., Cardoso, J.-F., Carron, J., Challinor, A., Chiang, H. C., Chluba, J., Colombo, L. P. L., Combet, C., Contreras, D., Crill, B. P., Cuttaia, F., de Bernardis, P., de Zotti, G., Delabrouille, J., Delouis, J.-M., Di Valentino, E., Diego, J. M., Doré, O., Douspis, M., Ducout, A., Dupac, X., Dusini, S., Efstathiou, G., Elsner, F., Enßlin, T. A., Eriksen, H. K., Fantaye, Y., Farhang, M., Fergusson, J., Fernandez-Cobos, R., Finelli, F., Forastieri, F., Frailis, M., Fraisse, A. A., Franceschi, E., Frolov, A., Galeotta, S., Galli, S., Ganga, K., Génova-Santos, R. T., Gerbino, M., Ghosh, T., González-Nuevo, J., Górski, K. M., Gratton, S., Gruppuso, A., Gudmundsson, J. E., Hamann, J., Handley, W., Hansen, F. K., Herranz, D., Hildebrandt, S. R., Hivon, E., Huang, Z., Jaffe, A. H., Jones, W. C., Karakci, A., Keihänen, E., Keskitalo, R., Kiiveri, K., Kim, J., Kisner, T. S., Knox, L., Krachmalnicoff, N., Kunz, M., Kurki-Suonio, H., Lagache, G., Lamarre, J.-M., Lasenby, A., Lattanzi, M., Lawrence, C. R., Le Jeune, M., Lemos, P., Lesgourgues, J., Levrier, F., Lewis, A., Liguori, M., Lilje, P. B., Lilley, M., Lindholm, V., López-Caniego, M., Lubin, P. M., Ma, Y.-Z., Macıas-Pérez, J. F., Maggio, G., Maino, D., Mandolesi, N., Mangilli, A., Marcos-Caballero, A., Maris, M., Martin, P. G., Martinelli, M., Martınez-González, E.,

Matarrese, S., Mauri, N., McEwen, J. D., Meinhold, P. R., Melchiorri, A., Mennella, A., Migliaccio, M., Millea, M., Mitra, S., Miville-Deschênes, M.-A., Molinari, D., Montier, L., Morgante, G., Moss, A., Natoli, P., Nørgaard-Nielsen, H. U., Pagano, L., Paoletti, D., Partridge, B., Patanchon, G., Peiris, H. V., Perrotta, F., Pettorino, V., Piacentini, F., Polastri, L., Polenta, G., Puget, J.-L., Rachen, J. P., Reinecke, M., Remazeilles, M., Renzi, A., Rocha, G., Rosset, C., Roudier, G., Rubiño-Martın, J. A., Ruiz-Granados, B., Salvati, L., Sandri, M., Savelainen, M., Scott, D., Shellard, E. P. S., Sirignano, C., Sirri, G., Spencer, L. D., Sunyaev, R., Suur-Uski, A.-S., Tauber, J. A., Tavagnacco, D., Tenti, M., Toffolatti, L., Tomasi, M., Trombetti, T., Valenziano, L., Valiviita, J., Van Tent, B., Vibert, L., Vielva, P., Villa, F., Vittorio, N., Wandelt, B. D., Wehus, I. K., White, M., White, S. D. M., Zacchei, A., and Zonca, A. "Planck 2018 results - VI. Cosmological parameters". In: *A&A* 641 (2020), A6. DOI: 10.1051/0004-6361/201833910. URL: https://doi.org/10.1051/0004-6361/201833910.

[3] C. L. Bennett, A. J. Banday, K. M. Górski, G. Hinshaw, P. Jackson, P. Keegstra, A. Kogut, G. F. Smoot, D. T. Wilkinson, and E. L. Wright. "Four-Year COBE* DMR Cosmic Microwave Background Observations: Maps and Basic Results". In: *The Astrophysical Journal* 464.1 (June 1996), p. L1. DOI: 10.1086/310075. URL: https://dx.doi.org/10.1086/310075.

[4] Steven Weinberg. *Cosmology*. 2008. ISBN: 978-0-19-852682-7.

[5] Alan H. Guth. "Inflationary universe: A possible solution to the horizon and flatness problems". In: *Phys. Rev. D* 23 (2 Jan. 1981), pp. 347–356. DOI: 10.1103/PhysRevD.23.347. URL: https://link.aps.org/doi/10.1103/PhysRevD.23.347.

[6] A.D. Linde. "A new inflationary universe scenario: A possible solution of the horizon, flatness, homogeneity, isotropy and primordial monopole problems". In: *Physics Letters B* 108.6 (1982), pp. 389–393. ISSN: 0370-2693. DOI: https://doi.org/10.1016/0370-2693(82)91219-9. URL: https://www.sciencedirect.com/science/article/pii/0370269382912199.

[7] Andreas Albrecht and Paul J. Steinhardt. “Cosmology for Grand Unified Theories with Radiatively Induced Symmetry Breaking”. In: *Phys. Rev. Lett.* 48 (17 Apr. 1982), pp. 1220–1223. DOI: 10.1103/PhysRevLett.48.1220. URL: https://link.aps.org/doi/10.1103/PhysRevLett.48.1220.

[8] Wayne Hu. *Wayne Hu CMB Tutorials*. 1996. URL: http://background.uchicago.edu/index.html.

[9] K.N. Abazajian, K. Arnold, J. Austermann, B.A. Benson, C. Bischoff, J. Bock, J.R. Bond, J. Borrill, I. Buder, D.L. Burke, E. Calabrese, J.E. Carlstrom, C.S. Carvalho, C.L. Chang, H.C. Chiang, S. Church, A. Cooray, T.M. Crawford, B.P. Crill, K.S. Dawson, S. Das, M.J. Devlin, M. Dobbs, S. Dodelson, O. Doré, J. Dunkley, J.L. Feng, A. Fraisse, J. Gallicchio, S.B. Giddings, D. Green, N.W. Halverson, S. Hanany, D. Hanson, S.R. Hildebrandt, A. Hincks, R. Hlozek, G. Holder, W.L. Holzapfel, K. Honscheid, G. Horowitz, W. Hu, J. Hubmayr, K. Irwin, M. Jackson, W.C. Jones, R. Kallosh, M. Kamionkowski, B. Keating, R. Keisler, W. Kinney, L. Knox, E. Komatsu, J. Kovac, C.-L. Kuo, A. Kusaka, C. Lawrence, A.T. Lee, E. Leitch, A. Linde, E. Linder, P. Lubin, J. Maldacena, E. Martinec, J. McMahon, A. Miller, V. Mukhanov, L. Newburgh, M.D. Niemack, H. Nguyen, H.T. Nguyen, L. Page, C. Pryke, C.L. Reichardt, J.E. Ruhl, N. Sehgal, U. Seljak, L. Senatore, J. Sievers, E. Silverstein, A. Slosar, K.M. Smith, D. Spergel, S.T. Staggs, A. Stark, R. Stompor, A.G. Vieregg, G. Wang, S. Watson, E.J. Wollack, W.L.K. Wu, K.W. Yoon, O. Zahn, and M. Zaldarriaga. “Inflation physics from the cosmic microwave background and large scale structure”. In: *Astroparticle Physics* 63 (2015). Dark Energy and CMB, pp. 55–65. ISSN: 0927-6505. DOI: https://doi.org/10.1016/j.astropartphys.2014.05.013. URL: https://www.sciencedirect.com/science/article/pii/S0927650514000838.

[10] Wayne Hu and Scott Dodelson. “Cosmic Microwave Background Anisotropies”. In: *Annual Review of Astronomy and Astrophysics* 40.1 (2002), pp. 171–216. DOI: 10.1146/

annurev.astro.40.060401.093926. eprint: https://doi.org/10.1146/annurev.astro.40.060401.093926. URL: https://doi.org/10.1146/annurev.astro.40.060401.093926.

[11] Uroš Seljak and Matias Zaldarriaga. "Signature of Gravity Waves in the Polarization of the Microwave Background". In: *Physical Review Letters* 78.11 (Mar. 1997), pp. 2054–2057. DOI: 10.1103/PhysRevLett.78.2054. arXiv: astro-ph/9609169 [astro-ph].

[12] P. A. R. Ade, Z. Ahmed, M. Amiri, D. Barkats, R. Basu Thakur, C. A. Bischoff, D. Beck, J. J. Bock, H. Boenish, E. Bullock, V. Buza, J. R. Cheshire, J. Connors, J. Cornelison, M. Crumrine, A. Cukierman, E. V. Denison, M. Dierickx, L. Duband, M. Eiben, S. Fatigoni, J. P. Filippini, S. Fliescher, N. Goeckner-Wald, D. C. Goldfinger, J. Grayson, P. Grimes, G. Hall, G. Halal, M. Halpern, E. Hand, S. Harrison, S. Henderson, S. R. Hildebrandt, G. C. Hilton, J. Hubmayr, H. Hui, K. D. Irwin, J. Kang, K. S. Karkare, E. Karpel, S. Kefeli, S. A. Kernasovskiy, J. M. Kovac, C. L. Kuo, K. Lau, E. M. Leitch, A. Lennox, K. G. Megerian, L. Minutolo, L. Moncelsi, Y. Nakato, T. Namikawa, H. T. Nguyen, R. O'Brient, R. W. Ogburn, S. Palladino, T. Prouve, C. Pryke, B. Racine, C. D. Reintsema, S. Richter, A. Schillaci, R. Schwarz, B. L. Schmitt, C. D. Sheehy, A. Soliman, T. St. Germaine, B. Steinbach, R. V. Sudiwala, G. P. Teply, K. L. Thompson, J. E. Tolan, C. Tucker, A. D. Turner, C. Umiltà, C. Vergès, A. G. Vieregg, A. Wandui, A. C. Weber, D. V. Wiebe, J. Willmert, C. L. Wong, W. L. K. Wu, H. Yang, K. W. Yoon, E. Young, C. Yu, L. Zeng, C. Zhang, and S. Zhang. "Improved Constraints on Primordial Gravitational Waves using Planck, WMAP, and BICEP/Keck Observations through the 2018 Observing Season". In: *Phys. Rev. Lett.* 127 (15 Oct. 2021), p. 151301. DOI: 10.1103/PhysRevLett.127.151301. URL: https://link.aps.org/doi/10.1103/PhysRevLett.127.151301.

[13] The Polarbear Collaboration: P. A. R. Ade, Y. Akiba, A. E. Anthony, K. Arnold, M. Atlas, D. Barron, D. Boettger, J. Borrill, S. Chapman, Y. Chinone, M. Dobbs, T. Elleflot, J. Errard, G. Fabbian, C. Feng, D. Flanigan, A. Gilbert, W. Grainger, N. W. Halverson, M. Hasegawa, K. Hattori, M. Hazumi, W. L. Holzapfel, Y. Hori, J. Howard, P. Hyland, Y.

Inoue, G. C. Jaehnig, A. H. Jaffe, B. Keating, Z. Kermish, R. Keskitalo, T. Kisner, M. Le Jeune, A. T. Lee, E. M. Leitch, E. Linder, M. Lungu, F. Matsuda, T. Matsumura, X. Meng, N. J. Miller, H. Morii, S. Moyerman, M. J. Myers, M. Navaroli, H. Nishino, A. Orlando, H. Paar, J. Peloton, D. Poletti, E. Quealy, G. Rebeiz, C. L. Reichardt, P. L. Richards, C. Ross, I. Schanning, D. E. Schenck, B. D. Sherwin, A. Shimizu, C. Shimmin, M. Shimon, P. Siritanasak, G. Smecher, H. Spieler, N. Stebor, B. Steinbach, R. Stompor, A. Suzuki, S. Takakura, T. Tomaru, B. Wilson, A. Yadav, and O. Zahn. "A MEASUREMENT OF THE COSMIC MICROWAVE BACKGROUND B-MODE POLARIZATION POWER SPECTRUM AT SUB-DEGREE SCALES WITH POLARBEAR". In: *The Astrophysical Journal* 794.2 (Oct. 2014), p. 171. DOI: 10.1088/0004-637X/794/2/171. URL: https://dx.doi.org/10.1088/0004-637X/794/2/171.

[14] Planck Collaboration, Akrami, Y., Ashdown, M., Aumont, J., Baccigalupi, C., Ballardini, M., Banday, A. J., Barreiro, R. B., Bartolo, N., Basak, S., Benabed, K., Bersanelli, M., Bielewicz, P., Bond, J. R., Borrill, J., Bouchet, F. R., Boulanger, F., Bucher, M., Burigana, C., Calabrese, E., Cardoso, J.-F., Carron, J., Casaponsa, B., Challinor, A., Colombo, L. P. L., Combet, C., Crill, B. P., Cuttaia, F., de Bernardis, P., de Rosa, A., de Zotti, G., Delabrouille, J., Delouis, J.-M., Di Valentino, E., Dickinson, C., Diego, J. M., Donzelli, S., Doré, O., Ducout, A., Dupac, X., Efstathiou, G., Elsner, F., Enßlin, T. A., Eriksen, H. K., Falgarone, E., Fernandez-Cobos, R., Finelli, F., Forastieri, F., Frailis, M., Fraisse, A. A., Franceschi, E., Frolov, A., Galeotta, S., Galli, S., Ganga, K., Génova-Santos, R. T., Gerbino, M., Ghosh, T., González-Nuevo, J., Górski, K. M., Gratton, S., Gruppuso, A., Gudmundsson, J. E., Handley, W., Hansen, F. K., Helou, G., Herranz, D., Hildebrandt, S. R., Huang, Z., Jaffe, A. H., Karakci, A., Keihänen, E., Keskitalo, R., Kiiveri, K., Kim, J., Kisner, T. S., Krachmalnicoff, N., Kunz, M., Kurki-Suonio, H., Lagache, G., Lamarre, J.-M., Lasenby, A., Lattanzi, M., Lawrence, C. R., Le Jeune, M., Levrier, F., Liguori, M., Lilje, P. B., Lindholm, V., López-Caniego, M., Lubin, P. M., Ma, Y.-Z., Macıas-Pérez, J.

F., Maggio, G., Maino, D., Mandolesi, N., Mangilli, A., Marcos-Caballero, A., Maris, M., Martin, P. G., Martınez-González, E., Matarrese, S., Mauri, N., McEwen, J. D., Meinhold, P. R., Melchiorri, A., Mennella, A., Migliaccio, M., Miville-Deschênes, M.-A., Molinari, D., Moneti, A., Montier, L., Morgante, G., Natoli, P., Oppizzi, F., Pagano, L., Paoletti, D., Partridge, B., Peel, M., Pettorino, V., Piacentini, F., Polenta, G., Puget, J.-L., Rachen, J. P., Reinecke, M., Remazeilles, M., Renzi, A., Rocha, G., Roudier, G., Rubiño-Martın, J. A., Ruiz-Granados, B., Salvati, L., Sandri, M., Savelainen, M., Scott, D., Seljebotn, D. S., Sirignano, C., Spencer, L. D., Suur-Uski, A.-S., Tauber, J. A., Tavagnacco, D., Tenti, M., Thommesen, H., Toffolatti, L., Tomasi, M., Trombetti, T., Valiviita, J., Van Tent, B., Vielva, P., Villa, F., Vittorio, N., Wandelt, B. D., Wehus, I. K., Zacchei, A., and Zonca, A. "Planck 2018 results - IV. Diffuse component separation". In: *A&A* 641 (2020), A4. DOI: 10.1051/0004-6361/201833881. URL: https://doi.org/10.1051/0004-6361/201833881.

[15] Wayne Stein. "Infrared Radiation from Interstellar Grains". In: *The Astrophysical Journal* 144 (Apr. 1966), p. 318. DOI: 10.1086/148606.

[16] Peter Ade, James Aguirre, Zeeshan Ahmed, Simone Aiola, Aamir Ali, David Alonso, Marcelo A. Alvarez, Kam Arnold, Peter Ashton, Jason Austermann, Humna Awan, Carlo Baccigalupi, Taylor Baildon, Darcy Barron, Nick Battaglia, Richard Battye, Eric Baxter, Andrew Bazarko, James A. Beall, Rachel Bean, Dominic Beck, Shawn Beckman, Benjamin Beringue, Federico Bianchini, Steven Boada, David Boettger, J. Richard Bond, Julian Borrill, Michael L. Brown, Sarah Marie Bruno, Sean Bryan, Erminia Calabrese, Victoria Calafut, Paolo Calisse, Julien Carron, Anthony Challinor, Grace Chesmore, Yuji Chinone, Jens Chluba, Hsiao-Mei Sherry Cho, Steve Choi, Gabriele Coppi, Nicholas F. Cothard, Kevin Coughlin, Devin Crichton, Kevin D. Crowley, Kevin T. Crowley, Ari Cukierman, John M. DÉwart, Rolando Dünner, Tijmen de Haan, Mark Devlin, Simon Dicker, Joy Didier, Matt Dobbs, Bradley Dober, Cody J. Duell, Shannon Duff, Adri Duivenvoorden, Jo Dunkley, John Dusatko, Josquin Errard, Giulio Fabbian, Stephen Feeney,

Simone Ferraro, Pedro Fluxà, Katherine Freese, Josef C. Frisch, Andrei Frolov, George Fuller, Brittany Fuzia, Nicholas Galitzki, Patricio A. Gallardo, Jose Tomas Galvez Ghersi, Jiansong Gao, Eric Gawiser, Martina Gerbino, Vera Gluscevic, Neil Goeckner-Wald, Joseph Golec, Sam Gordon, Megan Gralla, Daniel Green, Arpi Grigorian, John Groh, Chris Groppi, Yilun Guan, Jon E. Gudmundsson, Dongwon Han, Peter Hargrave, Masaya Hasegawa, Matthew Hasselfield, Makoto Hattori, Victor Haynes, Masashi Hazumi, Yizhou He, Erin Healy, Shawn W. Henderson, Carlos Hervias-Caimapo, Charles A. Hill, J. Colin Hill, Gene Hilton, Matt Hilton, Adam D. Hincks, Gary Hinshaw, Renée Hložek, Shirley Ho, Shuay-Pwu Patty Ho, Logan Howe, Zhiqi Huang, Johannes Hubmayr, Kevin Huffenberger, John P. Hughes, Anna Ijjas, Margaret Ikape, Kent Irwin, Andrew H. Jaffe, Bhuvnesh Jain, Oliver Jeong, Daisuke Kaneko, Ethan D. Karpel, Nobuhiko Katayama, Brian Keating, Sarah S. Kernasovskiy, Reijo Keskitalo, Theodore Kisner, Kenji Kiuchi, Jeff Klein, Kenda Knowles, Brian Koopman, Arthur Kosowsky, Nicoletta Krachmalnicoff, Stephen E. Kuenstner, Chao-Lin Kuo, Akito Kusaka, Jacob Lashner, Adrian Lee, Eunseong Lee, David Leon, Jason S. -Y. Leung, Antony Lewis, Yaqiong Li, Zack Li, Michele Limon, Eric Linder, Carlos Lopez-Caraballo, Thibaut Louis, Lindsay Lowry, Marius Lungu, Mathew Madhavacheril, Daisy Mak, Felipe Maldonado, Hamdi Mani, Ben Mates, Frederick Matsuda, Loic Maurin, Phil Mauskopf, Andrew May, Nialh McCallum, Chris McKenney, Jeff McMahon, P. Daniel Meerburg, Joel Meyers, Amber Miller, Mark Mirmelstein, Kavilan Moodley, Moritz Munchmeyer, Charles Munson, Sigurd Naess, Federico Nati, Martin Navaroli, Laura Newburgh, Ho Nam Nguyen, Michael Niemack, Haruki Nishino, John Orlowski-Scherer, Lyman Page, Bruce Partridge, Julien Peloton, Francesca Perrotta, Lucio Piccirillo, Giampaolo Pisano, Davide Poletti, Roberto Puddu, Giuseppe Puglisi, Chris Raum, Christian L. Reichardt, Mathieu Remazeilles, Yoel Rephaeli, Dominik Riechers, Felipe Rojas, Anirban Roy, Sharon Sadeh, Yuki Sakurai, Maria Salatino, Mayuri Sathyanarayana Rao, Emmanuel Schaan, Marcel Schmittfull, Neelima Sehgal, Joseph Seibert, Uros Seljak, Blake Sherwin, Meir Shimon, Carlos Sierra, Jonathan Sievers,

Precious Sikhosana, Maximiliano Silva-Feaver, Sara M. Simon, Adrian Sinclair, Praween Siritanasak, Kendrick Smith, Stephen R. Smith, David Spergel, Suzanne T. Staggs, George Stein, Jason R. Stevens, Radek Stompor, Aritoki Suzuki, Osamu Tajima, Satoru Takakura, Grant Teply, Daniel B. Thomas, Ben Thorne, Robert Thornton, Hy Trac, Calvin Tsai, Carole Tucker, Joel Ullom, Sunny Vagnozzi, Alexander van Engelen, Jeff Van Lanen, Daniel D. Van Winkle, Eve M. Vavagiakis, Clara Vergès, Michael Vissers, Kasey Wagoner, Samantha Walker, Jon Ward, Ben Westbrook, Nathan Whitehorn, Jason Williams, Joel Williams, Edward J. Wollack, Zhilei Xu, Byeonghee Yu, Cyndia Yu, Fernando Zago, Hezi Zhang, Ningfeng Zhu, and Simons Observatory Collaboration. "The Simons Observatory: science goals and forecasts". In: *Journal of Cosmology and Astrophysics* 2019.2, 056 (Feb. 2019), p. 056. DOI: 10.1088/1475-7516/2019/02/056. arXiv: 1808.07445 [astro-ph.CO].

[17] D. S. Swetz, P. A. R. Ade, M. Amiri, J. W. Appel, E. S. Battistelli, B. Burger, J. Chervenak, M. J. Devlin, S. R. Dicker, W. B. Doriese, R. Dünner, T. Essinger-Hileman, R. P. Fisher, J. W. Fowler, M. Halpern, M. Hasselfield, G. C. Hilton, A. D. Hincks, K. D. Irwin, N. Jarosik, M. Kaul, J. Klein, J. M. Lau, M. Limon, T. A. Marriage, D. Marsden, K. Martocci, P. Mauskopf, H. Moseley, C. B. Netterfield, M. D. Niemack, M. R. Nolta, L. A. Page, L. Parker, S. T. Staggs, O. Stryzak, E. R. Switzer, R. Thornton, C. Tucker, E. Wollack, and Y. Zhao. "OVERVIEW OF THE ATACAMA COSMOLOGY TELESCOPE: RECEIVER, INSTRUMENTATION, AND TELESCOPE SYSTEMS". In: *The Astrophysical Journal Supplement Series* 194.2 (June 2011), p. 41. DOI: 10.1088/0067-0049/194/2/41. URL: https://dx.doi.org/10.1088/0067-0049/194/2/41.

[18] R. J. Thornton, P. A. R. Ade, S. Aiola, F. E. Angilè, M. Amiri, J. A. Beall, D. T. Becker, H-M. Cho, S. K. Choi, P. Corlies, K. P. Coughlin, R. Datta, M. J. Devlin, S. R. Dicker, R. Dünner, J. W. Fowler, A. E. Fox, P. A. Gallardo, J. Gao, E. Grace, M. Halpern, M. Hasselfield, S. W. Henderson, G. C. Hilton, A. D. Hincks, S. P. Ho, J. Hubmayr, K. D.

Irwin, J. Klein, B. Koopman, Dale Li, T. Louis, M. Lungu, L. Maurin, J. McMahon, C. D. Munson, S. Naess, F. Nati, L. Newburgh, J. Nibarger, M. D. Niemack, P. Niraula, M. R. Nolta, L. A. Page, C. G. Pappas, A. Schillaci, B. L. Schmitt, N. Sehgal, J. L. Sievers, S. M. Simon, S. T. Staggs, C. Tucker, M. Uehara, J. van Lanen, J. T. Ward, and E. J. Wollack. "THE ATACAMA COSMOLOGY TELESCOPE: THE POLARIZATION-SENSITIVE ACTPol INSTRUMENT". In: *The Astrophysical Journal Supplement Series* 227.2 (Dec. 2016), p. 21. DOI: 10.3847/1538-4365/227/2/21. URL: https://dx.doi.org/10.3847/1538-4365/227/2/21.

[19] A. Suzuki, P. Ade, Y. Akiba, C. Aleman, K. Arnold, C. Baccigalupi, B. Barch, D. Barron, A. Bender, D. Boettger, J. Borrill, S. Chapman, Y. Chinone, A. Cukierman, M. Dobbs, A. Ducout, R. Dunner, T. Elleflot, J. Errard, G. Fabbian, S. Feeney, C. Feng, T. Fujino, G. Fuller, A. Gilbert, N. Goeckner-Wald, J. Groh, T. De Haan, G. Hall, N. Halverson, T. Hamada, M. Hasegawa, K. Hattori, M. Hazumi, C. Hill, W. Holzapfel, Y. Hori, L. Howe, Y. Inoue, F. Irie, G. Jaehnig, A. Jaffe, O. Jeong, N. Katayama, J. Kaufman, K. Kazemzadeh, B. Keating, Z. Kermish, R. Keskitalo, T. Kisner, A. Kusaka, M. Le Jeune, A. Lee, D. Leon, E. Linder, L. Lowry, F. Matsuda, T. Matsumura, N. Miller, K. Mizukami, J. Montgomery, M. Navaroli, H. Nishino, J. Peloton, D. Poletti, G. Puglisi, G. Rebeiz, C. Raum, C. Reichardt, P. Richards, C. Ross, K. Rotermund, Y. Segawa, B. Sherwin, I. Shirley, P. Siritanasak, N. Stebor, R. Stompor, J. Suzuki, O. Tajima, S. Takada, S. Takakura, S. Takatori, A. Tikhomirov, T. Tomaru, B. Westbrook, N. Whitehorn, T. Yamashita, A. Zahn, and O. Zahn. "The Polarbear-2 and the Simons Array Experiments". In: *Journal of Low Temperature Physics* 184.3-4 (Aug. 2016), pp. 805–810. DOI: 10.1007/s10909-015-1425-4. arXiv: 1512.07299 [astro-ph.IM].

[20] Kathleen Harrington, Tobias Marriage, Aamir Ali, John W. Appel, Charles L. Bennett, Fletcher Boone, Michael Brewer, Manwei Chan, David T. Chuss, Felipe Colazo, Sumit Dahal, Kevin Denis, Rolando Dünner, Joseph Eimer, Thomas Essinger-Hileman, Pedro

Fluxa, Mark Halpern, Gene Hilton, Gary F. Hinshaw, Johannes Hubmayr, Jeffrey Iuliano, John Karakla, Jeff McMahon, Nathan T. Miller, Samuel H. Moseley, Gonzalo Palma, Lucas Parker, Matthew Petroff, Bastián Pradenas, Karwan Rostem, Marco Sagliocca, Deniz Valle, Duncan Watts, Edward Wollack, Zhilei Xu, and Lingzhen Zeng. "The Cosmology Large Angular Scale Surveyor". In: *Millimeter, Submillimeter, and Far-Infrared Detectors and Instrumentation for Astronomy VIII*. Ed. by Wayne S. Holland and Jonas Zmuidzinas. Vol. 9914. International Society for Optics and Photonics. SPIE, 2016, 99141K. DOI: 10.1117/12.2233125. URL: https://doi.org/10.1117/12.2233125.

[21] E. Sánchez. "The Dark Energy Survey: Status and First results". In: *Nuclear and Particle Physics Proceedings* 273-275 (2016). 37th International Conference on High Energy Physics (ICHEP), pp. 302–308. ISSN: 2405-6014. DOI: https://doi.org/10.1016/j.nuclphysbps.2015.09.042. URL: https://www.sciencedirect.com/science/article/pii/S2405601415005313.

[22] Ž. Ivezić, S. M. Kahn, J. A. Tyson, B. Abel, E. Acosta, R. Allsman, D. Alonso, Y. AlSayyad, S. F. Anderson, J. Andrew, and et al. "LSST: From Science Drivers to Reference Design and Anticipated Data Products". In: *The Astrophysical Journal* 873, 111 (Mar. 2019), p. 111. DOI: 10.3847/1538-4357/ab042c. arXiv: 0805.2366.

[23] Alwyn Wootten and A. Richard Thompson. "The Atacama Large Millimeter/ Submillimeter Array". In: *Proceedings of the IEEE* 97.8 (2009), pp. 1463–1471. DOI: 10.1109/JPROC.2009.2020572.

[24] J. Errard, P. A. R. Ade, Y. Akiba, K. Arnold, M. Atlas, C. Baccigalupi, D. Barron, D. Boettger, J. Borrill, S. Chapman, Y. Chinone, A. Cukierman, J. Delabrouille, M. Dobbs, A. Ducout, T. Elleflot, G. Fabbian, C. Feng, S. Feeney, A. Gilbert, N. Goeckner-Wald, N. W. Halverson, M. Hasegawa, K. Hattori, M. Hazumi, C. Hill, W. L. Holzapfel, Y. Hori, Y. Inoue, G. C. Jaehnig, A. H. Jaffe, O. Jeong, N. Katayama, J. Kaufman, B. Keating, Z. Kermish, R. Keskitalo, T. Kisner, M. Le Jeune, A. T. Lee, E. M. Leitch, D. Leon,

E. Linder, F. Matsuda, T. Matsumura, N. J. Miller, M. J. Myers, M. Navaroli, H. Nishino, T. Okamura, H. Paar, J. Peloton, D. Poletti, G. Puglisi, G. Rebeiz, C. L. Reichardt, P. L. Richards, C. Ross, K. M. Rotermund, D. E. Schenck, B. D. Sherwin, P. Siritanasak, G. Smecher, N. Stebor, B. Steinbach, R. Stompor, A. Suzuki, O. Tajima, S. Takakura, A. Tikhomirov, T. Tomaru, N. Whitehorn, B. Wilson, A. Yadav, and O. Zahn. "MODELING ATMOSPHERIC EMISSION FOR CMB GROUND-BASED OBSERVATIONS". In: *The Astrophysical Journal* 809.1 (Aug. 2015), p. 63. DOI: 10.1088/0004-637X/809/1/63. URL: https://dx.doi.org/10.1088/0004-637X/809/1/63.

[25] Charles A. Hill, Sarah Marie M. Bruno, Sara M. Simon, Aamir Ali, Kam S. Arnold, Peter C. Ashton, Darcy Barron, Sean Bryan, Yuji Chinone, Gabriele Coppi, Kevin T. Crowley, Ari Cukierman, Simon Dicker, Jo Dunkley, Giulio Fabbian, Nicholas Galitzki, Patricio A. Gallardo, Jon E. Gudmundsson, Johannes Hubmayr, Brian Keating, Akito Kusaka, Adrian T. Lee, Frederick Matsuda, Philip D. Mauskopf, Jeffrey McMahon, Michael D. Niemack, Giuseppe Puglisi, Mayuri Sathyanarayana Rao, Maria Salatino, Carlos Sierra, Suzanne Staggs, Aritoki Suzuki, Grant Teply, Joel N. Ullom, Benjamin Westbrook, Zhilei Xu, and Ningfeng Zhu. "BoloCalc: a sensitivity calculator for the design of Simons Observatory". In: *Millimeter, Submillimeter, and Far-Infrared Detectors and Instrumentation for Astronomy IX*. Ed. by Jonas Zmuidzinas and Jian-Rong Gao. Vol. 10708. International Society for Optics and Photonics. SPIE, 2018, p. 1070842. DOI: 10.1117/12.2313916. URL: https://doi.org/10.1117/12.2313916.

[26] Zhilei Xu, Tanay Bhandarkar, Gabriele Coppi, Anna Kofman, John L. Orlowski-Scherer, Ningfeng Zhu, Aamir M. Ali, Kam Arnold, Jason E. Austermann, Steve K. Choi, Jake Connors, Nicholas F. Cothard, Mark Devlin, Simon Dicker, Bradley Dober, Shannon M. Duff, Giulio Fabbian, Nicholas Galitzki, Saianeesh Haridas, Katheleen Harrington, Erin Healy, Shuay-Pwu Patty Ho, Johannes Hubmayr, Jeffrey Iuliano, Jack Lashner, Yaqiong Li, Michele Limon, Brian J. Koopman, Heather McCarrick, Jenna Moore, Federico

Nati, Michael D. Niemack, Christian L. Reichardt, Karen Sarmiento, Joseph Seibert, Maximiliano Silva-Feaver, Rita F. Sonka, Suzanne Staggs, Robert J. Thornton, Eve M. Vavagiakis, Michael R. Vissers, Samantha Walker, Yuhan Wang, Edward J. Wollack, and Kaiwen Zheng. "The Simons Observatory: the Large Aperture Telescope Receiver (LATR) integration and validation results". In: *Millimeter, Submillimeter, and Far-Infrared Detectors and Instrumentation for Astronomy X*. Ed. by Jonas Zmuidzinas and Jian-Rong Gao. Vol. 11453. Society of Photo-Optical Instrumentation Engineers (SPIE) Conference Series. Dec. 2020, 1145315, p. 1145315. DOI: 10.1117/12.2576151. arXiv: 2012.07862 [astro-ph.IM].

[27] Ningfeng Zhu, Tanay Bhandarkar, Gabriele Coppi, Anna M. Kofman, John L. Orlowski-Scherer, Zhilei Xu, Shunsuke Adachi, Peter Ade, Simone Aiola, Jason Austermann, Andrew O. Bazarko, James A. Beall, Sanah Bhimani, J. Richard Bond, Grace E. Chesmore, Steve K. Choi, Jake Connors, Nicholas F. Cothard, Mark Devlin, Simon Dicker, Bradley Dober, Cody J. Duell, Shannon M. Duff, Rolando Dünner, Giulio Fabbian, Nicholas Galitzki, Patricio A. Gallardo, Joseph E. Golec, Saianeesh K. Haridas, Kathleen Harrington, Erin Healy, Shuay-Pwu Patty Ho, Zachary B. Huber, Johannes Hubmayr, Jeffrey Iuliano, Bradley R. Johnson, Brian Keating, Kenji Kiuchi, Brian J. Koopman, Jack Lashner, Adrian T. Lee, Yaqiong Li, Michele Limon, Michael Link, Tammy J. Lucas, Heather McCarrick, Jenna Moore, Federico Nati, Laura B. Newburgh, Michael D. Niemack, Elena Pierpaoli, Michael J. Randall, Karen Perez Sarmiento, Lauren J. Saunders, Joseph Seibert, Carlos Sierra, Rita Sonka, Jacob Spisak, Shreya Sutariya, Osamu Tajima, Grant P. Teply, Robert J. Thornton, Tran Tsan, Carole Tucker, Joel Ullom, Eve M. Vavagiakis, Michael R. Vissers, Samantha Walker, Benjamin Westbrook, Edward J. Wollack, and Mario Zannoni. "The Simons Observatory Large Aperture Telescope Receiver". In: *The Astrophysical Journal Supplement Series* 256.1, 23 (Sept. 2021), p. 23. DOI: 10.3847/1538-4365/ac0db7. arXiv: 2103.02747 [astro-ph.IM].

[28] Nicholas Galitzki, Aamir Ali, Kam S. Arnold, Peter C. Ashton, Jason E. Austermann, Carlo Baccigalupi, Taylor Baildon, Darcy Barron, James A. Beall, Shawn Beckman, Sarah Marie M. Bruno, Sean Bryan, Paolo G. Calisse, Grace E. Chesmore, Yuji Chinone, Steve K. Choi, Gabriele Coppi, Kevin D. Crowley, Kevin T. Crowley, Ari Cukierman, Mark J. Devlin, Simon Dicker, Bradley Dober, Shannon M. Duff, Jo Dunkley, Giulio Fabbian, Patricio A. Gallardo, Martina Gerbino, Neil Goeckner-Wald, Joseph E. Golec, Jon E. Gudmundsson, Erin E. Healy, Shawn Henderson, Charles A. Hill, Gene C. Hilton, Shuay-Pwu Patty Ho, Logan A. Howe, Johannes Hubmayr, Oliver Jeong, Brian Keating, Brian J. Koopman, Kenji Kiuchi, Akito Kusaka, Jacob Lashner, Adrian T. Lee, Yaqiong Li, Michele Limon, Marius Lungu, Frederick Matsuda, Philip D. Mauskopf, Andrew J. May, Nialh McCallum, Jeff McMahon, Federico Nati, Michael D. Niemack, John L. Orlowski-Scherer, Stephen C. Parshley, Lucio Piccirillo, Mayuri Sathyanarayana Rao, Christopher Raum, Maria Salatino, Joseph S. Seibert, Carlos Sierra, Max Silva-Feaver, Sara M. Simon, Suzanne T. Staggs, Jason R. Stevens, Aritoki Suzuki, Grant Teply, Robert Thornton, Calvin Tsai, Joel N. Ullom, Eve M. Vavagiakis, Michael R. Vissers, Benjamin Westbrook, Edward J. Wollack, Zhilei Xu, and Ningfeng Zhu. “The Simons Observatory: instrument overview”. In: *Millimeter, Submillimeter, and Far-Infrared Detectors and Instrumentation for Astronomy IX*. Ed. by Jonas Zmuidzinas and Jian-Rong Gao. Vol. 10708. Society of Photo-Optical Instrumentation Engineers (SPIE) Conference Series. July 2018, 1070804, p. 1070804. DOI: 10.1117/12.2312985. arXiv: 1808.04493 [astro-ph.IM].

[29] Aamir M. Ali, Shunsuke Adachi, Kam Arnold, Peter Ashton, Andrew Bazarko, Yuji Chinone, Gabriele Coppi, Lance Corbett, Kevin D. Crowley, Kevin T. Crowley, Mark Devlin, Simon Dicker, Shannon Duff, Chris Ellis, Nicholas Galitzki, Neil Goeckner-Wald, Kathleen Harrington, Erin Healy, Charles A. Hill, Shuay-Pwu Patty Ho, Johannes Hubmayr, Brian Keating, Kenji Kiuchi, Akito Kusaka, Adrian T. Lee, Michael Ludlam, Aashrita Mangu, Frederick Matsuda, Heather McCarrick, Federico Nati, Michael D. Niemack,

Haruki Nishino, John Orlowski-Scherer, Mayuri Sathyanarayana Rao, Christopher Raum, Yuki Sakurai, Maria Salatino, Trevor Sasse, Joseph Seibert, Carlos Sierra, Maximiliano Silva-Feaver, Jacob Spisak, Sara M. Simon, Suzanne Staggs, Osamu Tajima, Grant Teply, Tran Tsan, Edward Wollack, Bejamin Westbrook, Zhilei Xu, Mario Zannoni, and Ningfeng Zhu. "Small Aperture Telescopes for the Simons Observatory". In: *Journal of Low Temperature Physics* 200.5-6 (Apr. 2020), pp. 461–471. DOI: 10.1007/s10909-020-02430-5. arXiv: 2001.07848 [astro-ph.IM].

[30] Kenji Kiuchi, Shunsuke Adachi, Aamir M. Ali, Kam Arnold, Peter Ashton, Jason E. Austermann, Andrew Bazako, James A. Beall, Yuji Chinone, Gabriele Coppi, Kevin D. Crowley, Kevin T. Crowley, Simon Dicker, Bradley Dober, Shannon M. Duff, Giulio Fabbian, Nicholas Galitzki, Joseph E. Golec, Jon E. Gudmundsson, Kathleen Harrington, Masaya Hasegawa, Makoto Hattori, Charles A. Hill, Shuay-Pwu Patty Ho, Johannes Hubmayr, Bradley R. Johnson, Daisuke Kaneko, Nobuhiko Katayama, Brian Keating, Akito Kusaka, Jack Lashner, Adrian T. Lee, Frederick Matsuda, Heather McCarrick, Masaaki Murata, Federico Nati, Yume Nishinomiya, Lyman Page, Mayuri Sathyanarayana Rao, Christian L. Reichardt, Kana Sakaguri, Yuki Sakurai, Joseph Sibert, Jacob Spisak, Osamu Tajima, Grant P. Teply, Tomoki Terasaki, Tran Tsan, Samantha Walker, Edward J. Wollack, Zhilei Xu, Kyohei Yamada, Mario Zannoni, and Ningfeng Zhu. "Simons Observatory Small Aperture Telescope overview". In: *Ground-based and Airborne Telescopes VIII*. Ed. by Heather K. Marshall, Jason Spyromilio, and Tomonori Usuda. Vol. 11445. Society of Photo-Optical Instrumentation Engineers (SPIE) Conference Series. Dec. 2020, 114457L, p. 114457L. DOI: 10.1117/12.2562016. arXiv: 2101.11917 [astro-ph.IM].

[31] Joseph E. Golec et al. "Design and Fabrication of Metamaterial Anti-ReflectionCoatings for the Simons Observatory". In: *Society of Photo-Optical Instrumentation Engineers (SPIE) Conference Series*. in preparation. Dec. 2020.

[32] John L. Orlowski-Scherer, Ningfeng Zhu, Zhilei Xu, Aamir Ali, Kam S. Arnold, Peter C. Ashton, Gabriele Coppi, Mark Devlin, Simon Dicker, Nicholas Galitzki, Patricio A. Gallardo, Brian Keating, Adrian T. Lee, Michele Limon, Marius Lungu, Andrew May, Jeff McMahon, Michael D. Niemack, Lucio Piccirillo, Giuseppe Puglisi, Maria Salatino, Max Silva-Feaver, Sara M. Simon, Robert Thornton, and Eve M. Vavagiakis. "Simons Observatory large aperture receiver simulation overview". In: *Millimeter, Submillimeter, and Far-Infrared Detectors and Instrumentation for Astronomy IX*. Ed. by Jonas Zmuidzinas and Jian-Rong Gao. Vol. 10708. International Society for Optics and Photonics. SPIE, 2018, p. 107083X. DOI: 10.1117/12.2312868. URL: https://doi.org/10.1117/12.2312868.

[33] Kevin D. Crowley, Peter Dow, Jordan E. Shroyer, John C. Groh, Bradley Dober, Jacob Spisak, Nicholas Galitzki, Tanay Bhandarkar, Mark J. Devlin, Simon Dicker, Patricio A. Gallardo, Kathleen Harrington, Jeffrey Iuliano, Bradley R. Johnson, Delwin Johnson, Anna M. Kofman, Akito Kusaka, Adrian Lee, Michele Limon, Federico Nati, John Orlowski-Scherer, Lyman Page, Michael Randall, Grant Teply, Tran Tsan, Edward J. Wollack, Zhilei Xu, and Ningfeng Zhu. "The Simons Observatory: A large-diameter truss for a refracting telescope cooled to 1 K". In: *Review of Scientific Instruments* 93.5 (May 2022). 055106. ISSN: 0034-6748. DOI: 10.1063/5.0093857. eprint: https://pubs.aip.org/aip/rsi/article-pdf/doi/10.1063/5.0093857/16637830/055106_1_online.pdf. URL: https://doi.org/10.1063/5.0093857.

[34] Peter A. R. Ade, Giampaolo Pisano, Carole Tucker, and Samuel Weaver. "A review of metal mesh filters". In: *Society of Photo-Optical Instrumentation Engineers (SPIE) Conference Series*. Ed. by Jonas Zmuidzinas, Wayne S. Holland, Stafford Withington, and William D. Duncan. Vol. 6275. Society of Photo-Optical Instrumentation Engineers (SPIE) Conference Series. June 2006, 62750U, 62750U. DOI: 10.1117/12.673162.

[35] Kana Sakaguri et al. "AR coating with mullite and duroid for SA/SO half-wave plates and alumina filters". In preparation.

[36] Tomotake Matsumura, Shaul Hanany, Peter Ade, Bradley R. Johnson, Terry J. Jones, Prashanth Jonnalagadda, and Giorgio Savini. “Performance of three- and five-stack achromatic half-wave plates at millimeter wavelengths”. In: *Appl. Opt.* 48.19 (July 2009), pp. 3614–3625. DOI: 10.1364/AO.48.003614. URL: https://opg.optica.org/ao/abstract.cfm?URI=ao-48-19-3614.

[37] C. A. Hill, A. Kusaka, P. Ashton, P. Barton, T. Adkins, K. Arnold, B. Bixler, S. Ganjam, A. T. Lee, F. Matsuda, T. Matsumura, Y. Sakurai, R. Tat, and Y. Zhou. “A cryogenic continuously rotating half-wave plate mechanism for the POLARBEAR-2b cosmic microwave background receiver”. In: *Review of Scientific Instruments* 91.12 (Dec. 2020). 124503. ISSN: 0034-6748. DOI: 10.1063/5.0029006. eprint: https://pubs.aip.org/aip/rsi/article-pdf/doi/10.1063/5.0029006/14884669/124503_1_online.pdf. URL: https://doi.org/10.1063/5.0029006.

[38] Erin Healy, Aamir M. Ali, Kam Arnold, Jason E. Austermann, James A. Beall, Sarah Marie Bruno, Steve K. Choi, Jake Connors, Nicholas F. Cothard, Bradley Dober, Shannon M. Duff, Nicholas Galitzki, Gene Hilton, Shuay-Pwu Patty Ho, Johannes Hubmayr, Bradley R. Johnson, Yaqiong Li, Michael J. Link, Tammy J. Lucas, Heather McCarrick, Michael D. Niemack, Maximiliano Silva-Feaver, Rita F. Sonka, Suzanne Staggs, Eve M. Vavagiakis, Michael R. Vissers, Yuhan Wang, Edward J. Wollack, Zhilei Xu, Benjamin Westbrook, and Kaiwen Zheng. “Assembly development for the Simons Observatory focal plane readout module”. In: *Millimeter, Submillimeter, and Far-Infrared Detectors and Instrumentation for Astronomy X*. Ed. by Jonas Zmuidzinas and Jian-Rong Gao. Vol. 11453. International Society for Optics and Photonics. SPIE, 2020, p. 1145317. DOI: 10.1117/12.2561743. URL: https://doi.org/10.1117/12.2561743.

[39] Mayuri Sathyanarayana Rao, Maximiliano Silva-Feaver, Aamir Ali, Kam Arnold, Peter Ashton, Bradley J. Dober, Cody J. Duell, Shannon M. Duff, Nicholas Galitzki, Erin Healy, Shawn Henderson, Shuay-Pwu Patty Ho, Jonathan Hoh, Anna M. Kofman, Akito Kusaka,

Adrian T. Lee, Aashrita Mangu, Justin Mathewson, Philip Mauskopf, Heather McCarrick, Jenna Moore, Michael D. Niemack, Christopher Raum, Maria Salatino, Trevor Sasse, Joseph Seibert, Sara M. Simon, Suzanne Staggs, Jason R. Stevens, Grant Teply, Robert Thornton, Joel Ullom, Eve M. Vavagiakis, Benjamin Westbrook, Zhilei Xu, and Ningfeng Zhu. "Simons Observatory Microwave SQUID Multiplexing Readout: Cryogenic RF Amplifier and Coaxial Chain Design". In: *Journal of Low Temperature Physics* 199.3-4 (Mar. 2020), pp. 807–816. DOI: 10.1007/s10909-020-02429-y. arXiv: 2003.08949 [astro-ph.IM].

[40] Adrian Lee, Maximilian H. Abitbol, Shunsuke Adachi, Peter Ade, James Aguirre, Zeeshan Ahmed, Simone Aiola, Aamir Ali, David Alonso, Marcelo A. Alvarez, Kam Arnold, Peter Ashton, Zachary Atkins, Jason Austermann, Humna Awan, Carlo Baccigalupi, Taylor Baildon, Anton Baleato Lizancos, Darcy Barron, Nick Battaglia, Richard Battye, Eric Baxter, Andrew Bazarko, James A. Beall, Rachel Bean, Dominic Beck, Shawn Beckman, Benjamin Beringue, Tanay Bhandarkar, Sanah Bhimani, Federico Bianchini, Steven Boada, David Boettger, Boris Bolliet, J. Richard Bond, Julian Borrill, Michael L. Brown, Sarah Marie Bruno, Sean Bryan, Erminia Calabrese, Victoria Calafut, Paolo Calisse, Julien Carron, Fred. M. Carl, Juan Cayuso, Anthony Challinor, Grace Chesmore, Yuji Chinone, Jens Chluba, Hsiao-Mei Sherry Cho, Steve Choi, Susan Clark, Philip Clarke, Carlo Contaldi, Gabriele Coppi, Nicholas F. Cothard, Kevin Coughlin, Will Coulton, Devin Crichton, Kevin D. Crowley, Kevin T. Crowley, Ari Cukierman, John M. DÉwart, Rolando Dünner, Tijmen de Haan, Mark Devlin, Simon Dicker, Bradley Dober, Cody J. Duell, Shannon Duff, Adri Duivenvoorden, Jo Dunkley, Hamza El Bouhargani, Josquin Errard, Giulio Fabbian, Stephen Feeney, James Fergusson, Simone Ferraro, Pedro Fluxa, Katherine Freese, Josef C. Frisch, Andrei Frolov, George Fuller, Nicholas Galitzki, Patricio A. Gallardo, Jose Tomas Galvez Ghersi, Jiansong Gao, Eric Gawiser, Martina Gerbino, Vera Gluscevic, Neil Goeckner-Wald, Joseph Golec, Sam Gordon, Megan Gralla, Daniel Green, Arpi Grigorian,

John Groh, Chris Groppi, Yilun Guan, Jon E. Gudmundsson, Mark Halpern, Dongwon Han, Peter Hargrave, Kathleen Harrington, Masaya Hasegawa, Matthew Hasselfield, Makoto Hattori, Victor Haynes, Masashi Hazumi, Erin Healy, Shawn W. Henderson, Brandon Hensley, Carlos Hervias-Caimapo, Charles A. Hill, J. Colin Hill, Gene Hilton, Matt Hilton, Adam D. Hincks, Gary Hinshaw, Renee Hložek, Shirley Ho, Shuay-Pwu Patty Ho, Thuong D. Hoang, Jonathan Hoh, Selim C. Hotinli, Zhiqi Huang, Johannes Hubmayr, Kevin Huffenberger, John P. Hughes, Anna Ijjas, Margaret Ikape, Kent Irwin, Andrew H. Jaffe, Bhuvnesh Jain, Oliver Jeong, Matthew Johnson, Daisuke Kaneko, Ethan D. Karpel, Nobuhiko Katayama, Brian Keating, Reijo Keskitalo, Theodore Kisner, Kenji Kiuchi, Jeff Klein, Kenda Knowles, Anna Kofman, Brian Koopman, Arthur Kosowsky, Nicoletta Krachmalnicoff, Akito Kusaka, Paul La Plante, Jacob Lashner, Adrian Lee, Eunseong Lee, Antony Lewis, Yaqiong Li, Zack Li, Michele Limon, Eric Linder, Jia Liu, Carlos Lopez-Caraballo, Thibaut Louis, Marius Lungu, Mathew Madhavacheril, Daisy Mak, Felipe Maldonado, Hamdi Mani, Ben Mates, Frederick Matsuda, Loic Maurin, Phil Mauskopf, Andrew May, Nialh McCallum, Heather McCarrick, Chris McKenney, Jeff McMahon, P. Daniel Meerburg, James Mertens, Joel Meyers, Amber Miller, Mark Mirmelstein, Kavilan Moodley, Jenna Moore, Moritz Munchmeyer, Charles Munson, Masaaki Murata, Sigurd Naess, Toshiya Namikawa, Federico Nati, Martin Navaroli, Laura Newburgh, Ho Nam Nguyen, Andrina Nicola, Mike Niemack, Haruki Nishino, Yume Nishinomiya, John Orlowski-Scherer, Luca Pagano, Bruce Partridge, Francesca Perrotta, Phumlani Phakathi, Lucio Piccirillo, Elena Pierpaoli, Giampaolo Pisano, Davide Poletti, Roberto Puddu, Giuseppe Puglisi, Chris Raum, Christian L. Reichardt, Mathieu Remazeilles, Yoel Rephaeli, Dominik Riechers, Felipe Rojas, Aditya Rotti, Anirban Roy, Sharon Sadeh, Yuki Sakurai, Maria Salatino, Mayuri Sathyanarayana Rao, Lauren Saunders, Emmanuel Schaan, Marcel Schmittfull, Neelima Sehgal, Joseph Seibert, Uros Seljak, Paul Shellard, Blake Sherwin, Meir Shimon, Carlos Sierra, Jonathan Sievers, Cristobal Sifon, Precious Sikhosana, Maximiliano Silva-Feaver, Sara M. Simon, Adrian Sinclair, Kendrick Smith,

Wuhyun Sohn, Rita Sonka, David Spergel, Jacob Spisak, Suzanne T. Staggs, George Stein, Jason R. Stevens, Radek Stompor, Aritoki Suzuki, Osamu Tajima, Satoru Takakura, Grant Teply, Daniel B. Thomas, Ben Thorne, Robert Thornton, Hy Trac, Jesse Treu, Calvin Tsai, Carole Tucker, Joel Ullom, Sunny Vagnozzi, Alexander van Engelen, Jeff Van Lanen, Daniel D. Van Winkle, Eve M. Vavagiakis, Clara Vergès, Michael Vissers, Kasey Wagoner, Samantha Walker, Yuhan Wang, Jon Ward, Ben Westbrook, Nathan Whitehorn, Jason Williams, Joel Williams, Edward Wollack, Zhilei Xu, Siavash Yasini, Edward Young, Byeonghee Yu, Cyndia Yu, Fernando Zago, Mario Zannoni, Hezi Zhang, Kaiwen Zheng, Ningfeng Zhu, and Andrea Zonca. "The Simons Observatory". In: *Bulletin of the American Astronomical Society*. Vol. 51. Sept. 2019, 147, p. 147. DOI: 10.48550/arXiv.1907.08284. arXiv: 1907.08284 [astro-ph.IM].

[41] K.D. Irwin and G.C. Hilton. "Transition-Edge Sensors". In: *Cryogenic Particle Detection*. Ed. by Christian Enss. Berlin, Heidelberg: Springer Berlin Heidelberg, 2005, pp. 63–150. ISBN: 978-3-540-31478-3. DOI: 10.1007/10933596_3. URL: https://doi.org/10.1007/10933596_3.

[42] Kam Stahly Arnold. "Design and Deployment of the Polarbear Cosmic Microwave Background Polarization Experiment". PhD thesis. University of California, Berkeley, Dec. 2010.

[43] Jonas Zmuidzinas. "Thermal noise and correlations in photon detection". In: *Appl. Opt.* 42.25 (Sept. 2003), pp. 4989–5008. DOI: 10.1364/AO.42.004989. URL: https://opg.optica.org/ao/abstract.cfm?URI=ao-42-25-4989.

[44] John Arthur Benson Mates. "The Microwave SQUID Multiplexer". PhD thesis. University of Colorado, Boulder, Dec. 2011.

[45] Heather McCarrick, Erin Healy, Zeeshan Ahmed, Kam Arnold, Zachary Atkins, Jason E. Austermann, Tanay Bhandarkar, James A. Beall, Sarah Marie Bruno, Steve K. Choi, Jake Connors, Nicholas F. Cothard, Kevin D. Crowley, Simon Dicker, Bradley Dober,

Cody J. Duell, Shannon M. Duff, Daniel Dutcher, Josef C. Frisch, Nicholas Galitzki, Megan B. Gralla, Jon E. Gudmundsson, Shawn W. Henderson, Gene C. Hilton, Shuay-Pwu Patty Ho, Zachary B. Huber, Johannes Hubmayr, Jeffrey Iuliano, Bradley R. Johnson, Anna M. Kofman, Akito Kusaka, Jack Lashner, Adrian T. Lee, Yaqiong Li, Michael J. Link, Tammy J. Lucas, Marius Lungu, J. A. B. Mates, Jeffrey J. McMahon, Michael D. Niemack, John Orlowski-Scherer, Joseph Seibert, Maximiliano Silva-Feaver, Sara M. Simon, Suzanne Staggs, Aritoki Suzuki, Tomoki Terasaki, Robert Thornton, Joel N. Ullom, Eve M. Vavagiakis, Leila R. Vale, Jeff Van Lanen, Michael R. Vissers, Yuhan Wang, Edward J. Wollack, Zhilei Xu, Edward Young, Cyndia Yu, Kaiwen Zheng, and Ningfeng Zhu. "The Simons Observatory Microwave SQUID Multiplexing Detector Module Design". In: *The Astrophysical Journal* 922.1, 38 (Nov. 2021), p. 38. DOI: 10.3847/1538-4357/ac2232. arXiv: 2106.14797 [astro-ph.IM].

[46] Cyndia Yu, Zeeshan Ahmed, Josef C. Frisch, Shawn W. Henderson, Max Silva-Feaver, Kam Arnold, David Brown, Jake Connors, Ari J. Cukierman, J. Mitch DÉwart, Bradley J. Dober, John E. Dusatko, Gunther Haller, Ryan Herbst, Gene C. Hilton, Johannes Hubmayr, Kent D. Irwin, Chao-Lin Kuo, John A. B. Mates, Larry Ruckman, Joel Ullom, Leila Vale, Daniel D. Van Winkle, Jesus Vasquez, and Edward Young. "SLAC microresonator RF (SMuRF) electronics: A tone-tracking readout system for superconducting microwave resonator arrays". In: *Review of Scientific Instruments* 94.1 (Jan. 2023). 014712. ISSN: 0034-6748. DOI: 10.1063/5.0125084. eprint: https://pubs.aip.org/aip/rsi/article-pdf/doi/10.1063/5.0125084/16713259/014712_1_online.pdf. URL: https://doi.org/10.1063/5.0125084.

[47] Kathleen Harrington, Carlos Sierra, Grace Chesmore, Shreya Sutariya, Aamir M. Ali, Steve K. Choi, Nicholas F. Cothard, Simon Dicker, Nicholas Galitzki, Shuay-Pwu Patty Ho, Anna M. Kofman, Brian J. Koopman, Jack Lashner, Jeff McMahon, Michael D. Niemack, John Orlowski-Scherer, Joseph Seibert, Max Silva-Feaver, Eve M. Vavagiakis,

Zhilei Xu, and Ningfeng Zhu. “The Integration and Testing Program for the Simons Observatory Large Aperture Telescope Optics Tubes”. In: *arXiv e-prints*, arXiv:2102.02129 (Feb. 2021), arXiv:2102.02129. DOI: 10.48550/arXiv.2102.02129. arXiv: 2102.02129 [astro-ph.IM].

[48] Jason R. Stevens, Nicholas F. Cothard, Eve M. Vavagiakis, Aamir Ali, Kam Arnold, Jason E. Austermann, Steve K. Choi, Bradley J. Dober, Cody Duell, Shannon M. Duff, Gene C. Hilton, Shuay-Pwu Patty Ho, Thuong D. Hoang, Johannes Hubmayr, Adrian T. Lee, Aashrita Mangu, Federico Nati, Michael D. Niemack, Christopher Raum, Mario Renzullo, Maria Salatino, Trevor Sasse, Sara M. Simon, Suzanne Staggs, Aritoki Suzuki, Patrick Truitt, Joel Ullom, John Vivalda, Michael R. Vissers, Samantha Walker, Benjamin Westbrook, Edward J. Wollack, Zhilei Xu, and Daniel Yohannes. “Characterization of Transition Edge Sensors for the Simons Observatory”. In: *Journal of Low Temperature Physics* 199.3-4 (Feb. 2020), pp. 672–680. DOI: 10.1007/s10909-020-02375-9. arXiv: 1912.00860 [astro-ph.IM].

[49] Nicholas F. Cothard et al. “Comparing Complex Impedance and Bias Step Measurementsof Simons Observatory Transition Edge Sensors”. In: *Society of Photo-Optical Instrumentation Engineers (SPIE) Conference Series*. in preparation. Dec. 2020.

[50] Yuki Inoue, Tomotake Matsumura, Masashi Hazumi, Adrian T. Lee, Takahiro Okamura, Aritoki Suzuki, Takayuki Tomaru, and Hiroshi Yamaguchi. “Cryogenic infrared filter made of alumina for use at millimeter wavelength”. In: *Appl. Opt.* 53.9 (Mar. 2014), pp. 1727–1733. DOI: 10.1364/AO.53.001727. URL: https://opg.optica.org/ao/abstract.cfm?URI=ao-53-9-1727.

[51] Ningfeng Zhu, John L. Orlowski-Scherer, Zhilei Xu, Aamir Ali, Kam S. Arnold, Peter C. Ashton, Gabriele Coppi, Mark J. Devlin, Simon Dicker, Nicholas Galitzki, Patricio A. Gallardo, Shawn W. Henderson, Shuay-Pwu Patty Ho, Johannes Hubmayr, Brian Keating, Adrian T. Lee, Michele Limon, Marius Lungu, Philip D. Mauskopf, Andrew J.

May, Jeff McMahon, Michael D. Niemack, Lucio Piccirillo, Giuseppe Puglisi, Mayuri Sathyanarayana Rao, Maria Salatino, Max Silva-Feaver, Sara M. Simon, Suzanne Staggs, Robert Thornton, Joel N. Ullom, Eve M. Vavagiakis, Benjamin Westbrook, and Edward J. Wollack. "Simons Observatory large aperture telescope receiver design overview". In: *Millimeter, Submillimeter, and Far-Infrared Detectors and Instrumentation for Astronomy IX*. Ed. by Jonas Zmuidzinas and Jian-Rong Gao. Vol. 10708. Society of Photo-Optical Instrumentation Engineers (SPIE) Conference Series. July 2018, 1070829, p. 1070829. DOI: 10.1117/12.2312871. arXiv: 1808.10037 [astro-ph.IM].

[52] F. Matsuda, L. Lowry, A. Suzuki, M. Aguilar Fáundez, K. Arnold, D. Barron, F. Bianchini, K. Cheung, Y. Chinone, T. Elleflot, G. Fabbian, N. Goeckner-Wald, M. Hasegawa, D. Kaneko, N. Katayama, B. Keating, A. T. Lee, M. Navaroli, H. Nishino, H. Paar, G. Puglisi, P. L. Richards, J. Seibert, P. Siritanasak, O. Tajima, S. Takatori, C. Tsai, and B. Westbrook. "The POLARBEAR Fourier transform spectrometer calibrator and spectroscopic characterization of the POLARBEAR instrument". In: *Review of Scientific Instruments* 90.11, 115115 (Nov. 2019), p. 115115. DOI: 10.1063/1.5095160. arXiv: 1904.02901 [astro-ph.IM].

[53] K.S. Karkare et al. "Keck array and BICEP3: spectral characterization of 5000+ detectors". In: *Proc. SPIE Int. Soc. Opt. Eng.* 9153 (2014), 91533B. DOI: 10.1117/12.2056779.

[54] Nicholas Galitzki et al. "The Simons Observatory: Integration and testing of the first small aperture telescope, SAT-MF1 ". In preparation.

[55] Maximiliano Silva-Feaver. "Microwave SQUID Multiplexing for the Simons Observatory Cosmic Microwave Background Telescopes ". In preparation, expected July 2023.

[56] Shreya Sutariya, Kathleen Harrington, Thomas Alford, Carlos Sierra, and Jeff McMahon. "The Simons Observatory: Characterization of absorbing Neutral Density Filters". In: *Millimeter, Submillimeter, and Far-Infrared Detectors and Instrumentation for Astronomy XI*. Ed. by Jonas Zmuidzinas and Jian-Rong Gao. Vol. PC12190. International Society

for Optics and Photonics. SPIE, 2022, PC1219008. DOI: 10.1117/12.2630538. URL: https://doi.org/10.1117/12.2630538.

[57] Zhilei Xu, Michael K. Brewer, Pedro Fluxá Rojas, Yunyang Li, Keisuke Osumi, Bastián Pradenas, Aamir Ali, John W. Appel, Charles L. Bennett, Ricardo Bustos, Manwei Chan, David T. Chuss, Joseph Cleary, Jullianna Denes Couto, Sumit Dahal, Rahul Datta, Kevin L. Denis, Rolando Dünner, Joseph R. Eimer, Thomas Essinger-Hileman, Dominik Gothe, Kathleen Harrington, Jeffrey Iuliano, John Karakla, Tobias A. Marriage, Nathan J. Miller, Carolina Núñez, Ivan L. Padilla, Lucas Parker, Matthew A. Petroff, Rodrigo Reeves, Karwan Rostem, Deniz Augusto Nunes Valle, Duncan J. Watts, Janet L. Weiland, Edward J. Wollack, and (CLASS Collaboration). "Two-year Cosmology Large Angular Scale Surveyor (CLASS) Observations: 40 GHz Telescope Pointing, Beam Profile, Window Function, and Polarization Performance". In: *The Astrophysical Journal* 891.2 (Mar. 2020), p. 134. DOI: 10.3847/1538-4357/ab76c2. URL: https://dx.doi.org/10.3847/1538-4357/ab76c2.

[58] Grace E. Chesmore, Kathleen Harrington, Carlos E. Sierra, Patricio A. Gallardo, Shreya Sutariya, Tommy Alford, Alexandre E. Adler, Tanay Bhandarkar, Gabriele Coppi, Nadia Dachlythra, Joseph Golec, Jon Gudmundsson, Saianeesh K. Haridas, Bradley R. Johnson, Anna M. Kofman, Jeffrey Iuliano, Jeff McMahon, Michael D. Niemack, John Orlowski-Scherer, Karen Perez Sarmiento, Roberto Puddu, Max Silva-Feaver, Sara M. Simon, Julia Robe, Edward J. Wollack, and Zhilei Xu. "Simons Observatory: characterizing the Large Aperture TelescopeReceiver with radio holography". In: *Appl. Opt.* 61.34 (Dec. 2022), pp. 10309–10319. DOI: 10.1364/AO.470138. URL: https://opg.optica.org/ao/abstract.cfm?URI=ao-61-34-10309.

[59] D.H. Martin and E. Puplett. "Polarised interferometric spectrometry for the millimetre and submillimetre spectrum". In: *Infrared Physics* 10.2 (1970), pp. 105–109. ISSN: 0020-0891.

DOI: https://doi.org/10.1016/0020-0891(70)90006-0. URL: https://www.sciencedirect.com/science/article/pii/0020089170900060.

[60] Alan Kogut, Jens Chluba, Dale J. Fixsen, Stephan Meyer, and David Spergel. "The Primordial Inflation Explorer (PIXIE)". In: *Space Telescopes and Instrumentation 2016: Optical, Infrared, and Millimeter Wave*. Ed. by Howard A. MacEwen, Giovanni G. Fazio, Makenzie Lystrup, Natalie Batalha, Nicholas Siegler, and Edward C. Tong. Vol. 9904. International Society for Optics and Photonics. SPIE, 2016, 99040W. DOI: 10.1117/12.2231090. URL: https://doi.org/10.1117/12.2231090.

[61] T. Timusk and P. L. Richards. "Near millimeter wave bandpass filters". In: *Appl. Opt.* 20.8 (Apr. 1981), pp. 1355–1360. DOI: 10.1364/AO.20.001355. URL: https://opg.optica.org/ao/abstract.cfm?URI=ao-20-8-1355.

[62] Carlos Sierra et al. "Simons Observatory: Predeployment Performance of the Large Aperture Telescope Instrument in the 90 and 150 GHz Bands ". In preparation.